Fusion Neutron Production using Deuterium Fuel in an Inertial Electrostatic Confinement Device at 10 to 200 Kilovolts

By

Aaron N. Fancher

A dissertation submitted in partial fulfillment of

the requirements for the degree of

Doctor of Philosophy

(Nuclear Engineering & Engineering Physics)

at the

UNIVERSITY OF WISCONSIN – MADISON

2018

Date of final oral examination: 5/9/2018

This dissertation was approved by the following members of the Final Oral Committee:

Gerald, L. Kulcinski, Professor Emeritus, Engineering Physics
Douglass L. Henderson, Professor, Engineering Physics
Oliver Schmitz, Professor, Engineering Physics
David T. Anderson, Professor, Electrical and Computer Engineering
Todd R. Allen, Professor, Engineering Physics
John F. Santarius, Research Professor Emeritus, Engineering Physics

Abstract

This work details the advancement and understanding of fusion neutron generation capabilities using a deuterium fueled spherical gridded inertial electrostatic confinement (IEC) device operating up to 200 kV at the University of Wisconsin-Madison. The goal of this work was to extend the experimental and theoretical understanding of gridded IEC operations to previously unachieved 200 kV cathode operation and to investigate long term trends in the neutron production rate performance. To support this experimental investigation, hardware with the capability to reliably sustain 200 kV operation was developed by constructing a resistively divided 2-stage high voltage vacuum feedthrough. This new feedthrough design proved to be robust against destructive high voltage failures and was successful in achieving a peak IEC operational voltage at 210 kV and 30 mA cathode grid operation at a chamber pressure of 1.0 mTorr D_2.

Repeated measurements of the neutron production rate under fixed experimental conditions were performed over the span of 100 operational runs, which showed an upward trend in the neutron production rate performance. An investigation into the impact of impurity gas in the chamber during operation showed the reduction of impurity gas in the system and an increase in neutron production rate are correlated. An estimation of the neutron production rate increase over these runs due to embedded fusion reactions in the chamber wall showed a fuel density build up near the surface by the implantation of fast neutral deuterium particles leaving the system can plausibly account for the upward trend in neutron production rate measurements; however, measurements of this implanted deuterium profile are still needed to corroborate this estimate.

Parametric studies measured the neutron production rate with variations in the device cathode voltage (10-200 kV), cathode current (30-100 mA) and chamber pressure (0.2-1.7 mTorr D_2), and comparisons with a theoretical model are made. The results of this study showed the neutron production rate scales linearly with current as expected with a beam-background fusion regime and scales in a complex manner with voltage and pressure. Comparisons made to a theoretical model of the neutron production rate using an integral transport code previously developed for IEC devices at the University of Wisconsin showed that the predicted scaling with voltage agrees; however, a discrepancy in the absolute neutron production rate prediction by the model is found to be factor of 7.8 lower than experimental measurements. A new record for steady-state D-D neutron production rate of 3.8×10^8 neutrons/s has been achieved in a gridded IEC device at a cathode voltage of 200 kV, cathode current of 100 mA, and chamber pressure of 1.0 mTorr D_2.

Acknowledgments

I would like to thank Professor Gerald Kulcinski and Professor John Santarius for giving me the opportunity to pursue my doctoral degree at the University of Wisconsin and for instilling upon me the knowledge, wisdom, and encouragement to accomplish this feat. I would additionally like to thank those I have worked with during my time at the IEC laboratory: Richard Bonomo, Matthew Michalak, Matthew Jasica, Marcos Navarro, Karla Hall, Aaron Olson, Kevin Johnson, Nolan van Rossum, Gabriel Becerra, Craig Schuff, Aaron McEvoy, and the others I have had the pleasure to work with at the University of Wisconsin. Lastly, I would like to extend my deepest gratitude to my family that have provided love and support and to my friends that I have shared many adventures with during my time here at Wisconsin.

Table of Contents

List of Figures

List of Tables

1. Introduction

1.1 Motivation

Nuclear fusion is a subject of international study not only for developing a fusion energy source but also for numerous practical applications of high energy fusion products. In a basic description, nuclear fusion is the process of joining lighter nuclei to form a heavier nucleus, releasing energy and additional reaction products. While many large-scale experiments work toward a goal of fusion energy generation [1]–[3], other research is being conducted on the uses of fusion products for near term applications. Some of these applications include neutron generators for materials detection using activation analysis [4] and neutron radiography [5], [6]. Applications of charged fusion products that have been considered include space propulsion [7], [8], and radioisotope production [9]–[11].

At the University of Wisconsin-Madison Inertial Electrostatic Confinement Fusion Laboratory, devices have been developed with the capability of fusing fuels in a steady state or pulsed operation. Here, extensive experimental and theoretical campaigns have been conducted over the past two decades to better understand how inertial electrostatic confinement (IEC) fusion devices operate [12], and demonstrations of D-D, D-^{3}He, and ^{3}He-^{3}He fusion reactions using these IEC devices have been made [13]–[15]. By applying technology developed in the laboratory, several techniques using fusion fuels in IEC devices have been demonstrated, including: detection of highly enriched uranium [16] and chemical explosives [17] using D-D fusion neutrons, and production of medical isotopes ^{94m}Tc [9] and ^{13}N [10] using D-^{3}He fusion protons. Recently, a design study investigated unmanned aerial vehicles for the detection of nitrogen based explosives

by thermal neutron analysis using IEC neutron generators with a D-D neutron yield of 10^8 neutrons/s [18].

1.2 Objective

This work details the advancement and understanding of fusion neutron generation capabilities using deuterium fueled IEC devices at the University of Wisconsin-Madison. The focus of this work is the development of an IEC device capable of 200 kV operation and the use of this device to study of neutron generation at previously unachieved voltages. To accomplish this, three goals were identified.

The primary goal is to extend the experimental and theoretical understanding of gridded IEC operations to 200 kV operation. Previous efforts to understand gridded IEC devices have led to the development of an integral transport theory, named VICTER, that describes complex distributions of fusion producing particles within the device [19], [20]. Past experimental investigations of these devices have examined the energy and spatial distributions of particles, potential structures, and neutron production rate scaling with parameter variations up to 175 kV device operation. A review of past work in these areas is presented in Chapter 2, and a theoretical and computational description of IEC device operation is described in Chapter 3. If the dominant physics and neutron producing effects are well described, then neutron production rate scaling may be predicted for IEC devices and validated by experimental parameter studies at these previously unachieved levels.

To support this experimental investigation, hardware with the capability of reliably sustaining 200 kV operation must be developed for the IEC device. A goal of this work is to construct a high voltage vacuum feedthrough capable of meeting these demands while being

mechanically and electrically robust with a hardware lifetime suitable for conducting numerous experimental studies. Previous work has demonstrated that a multi-stage feedthrough technique can increase high voltage standoff levels in plasma devices in comparison to single stage insulator feedthroughs, and high voltage operation of an IEC device was previously demonstrated at 175 kV using this technique [21]. A review of past high voltage feedthrough development and achievements for IEC devices is presented in Chapter 2. An advanced hardware design with a multi-stage feedthrough has been developed for this work, and its use produced a record 200 kV operations in an IEC device. Parametric studies were then conducted to study neutron production scaling in this previously unexplored parameter space.

For this work, the neutron production rate from deuterium-deuterium fusion reactions is identified as a key physical quantity of interest to be measured. Several parameters may affect the neutron production rate output of an IEC device, including: device dimensions and geometry, chamber pressure, cathode voltage, cathode current, and experimental chamber conditions. A goal of this work is the measurement of the neutron production rate scaling with device voltage, current, and pressure for a single cathode-anode grid geometry. A previous study has indicated that the chamber conditions may be responsible for an upward drift in absolute neutron production rate performance of the device when observed over many runs and operational days while holding all other input parameters constant [21]. It is hypothesized that a build up over time of deuterium implanted into the chamber wall may contribute to the observed increase in absolute neutron production rates due to fast deuterium particles fusing with these wall targets, and an investigation into the rise in absolute neutron production rates is made.

A description of the hardware and experimental methods used in this thesis is presented in Chapter 4, and the results and discussion of this new hardware is presented in Chapter 5. Parametric

measurements of the neutron production rate scaling are presented in Chapter 6, and these results are compared theoretical expectations and the VICTER model. Repeat measurements of experimental conditions are analyzed in Chapter 7 to investigate the impact of impurity gas and estimate the contribution of fusion rates due to the presence of embedded fusion. Finally, an executive summary and key conclusions from this work are presented in Chapter 8 along with recommendations for future work in Chapter 9.

1.3 References

[1] R. Aymar, P. Barabaschi, and Y. Shimomura, "The ITER design," *Plasma Phys. Control. Fusion*, vol. 44, no. 5, pp. 519–565, 2002.

[2] E. I. Moses, "Ignition on the National Ignition Facility: a path towards inertial fusion energy," *Nucl. Fusion*, vol. 49, no. 10, p. 104022, 2009.

[3] H.-S. Bosch, et al., "Technical challenges in the construction of the steady-state stellarator Wendelstein 7-X," *Nucl. Fusion*, vol. 53, no. 12, p. 126001, 2013.

[4] S. S. Nargolwalla and E. P. Przybylowicz, *Activation and Analysis with Neutron Generators*. John Wiley and Sons, Inc., New York, 1973.

[5] J. Rynes, et al., "Gamma-ray and neutron radiography as part of a pulsed fast neutron analysis inspection system," *Nucl. Instruments Methods Phys. Res. Sect. A Accel. Spectrometers, Detect. Assoc. Equip.*, vol. 422, no. 1–3, pp. 895–899, 1999.

[6] J. T. Cremer, et al., "Large area imaging of hydrogenous materials using fast neutrons from a DD fusion generator," *Nucl. Instruments Methods Phys. Res. Sect. A Accel. Spectrometers, Detect. Assoc. Equip.*, vol. 675, pp. 51–55, 2012.

[7] S. H. Maslen, "Fusion for Space Propulsion," *IRE Trans. Mil. Electron.*, vol. MIL-3, no. 2, November, pp. 52-57, Apr. 1959.

[8] J.F. Santarius, "Lunar Helium-3, Fusion Propulsion, and Space Development," *Second Conference on Lunar Bases and Space Activities of the 21st Century* (NASA, Houston, TX, 1988), NASA Conf. Pub. 3166, Vol. 1, p. 75 (1992).

[9] B. Cipiti, "The Fusion of Advanced Fuels to Produce Medical Isotopes Using Inertial Electrostatic," Ph.D. dissertation, University of Wisconsin-Madison, 2004.

[10] J. Weidner, "The production of 13N from inertial electrostatic confinement fusion," M.S. thesis, University of Wisconsin-Madison, 2003.

[11] "Shine Medical Technologies." [Online]. Available: http://shinemed.com/. [Accessed: Apr. 30, 2018].

[12] G. L. Kulcinski, et al., "Progress in the Understanding of Gridded Inertial Electrostatic Confinement Devices at the University of Wisconsin," *Fusion Sci. Technol.*, vol. 68, no. 2, 2015.

[13] T. A. Thorson, "Fusion reactivity characterization of a spherically convergent ion focus," Ph.D. dissertation, University of Wisconsin-Madison, 1998.

[14] S. K. Murali, "Diagnostic study of steady state advanced fuel fusion in an IEC device," Ph.D. dissertation, University of Wisconsin-Madison, 2004.

[15] G. Piefer, "Performance of a Low-Pressure, Helicon Driven IEC 3He Fusion Device," Ph.D. dissertation, University of Wisconsin-Madison, 2006.

[16] R. F. Radel, "Detection of Highly Enriched Uranium and Tungsten Surface Damage Studies Using a Pulsed Inertial Electrostatic Confinement Fusion Device," Ph.D. dissertation, University of Wisconsin-Madison, 2007.

[17] A. L. Wehmeyer, "The Detection of Explosives Using an Inertial Electrostatic Confinement D-D Fusion Device," M.S. thesis, University of Wisconsin-Madison, 2005.

[18] K. M. Johnson, "Neutronics Analysis on an Explosives Detection System Using an Inertial Electrostatic Confinement Neutron Source and Unmanned Aerial Vehicles," M.S. thesis, University of Wisconsin-Madison, 2017.

[19] G. A. Emmert and J. F. Santarius, "Atomic and molecular effects on spherically convergent ion flow. I. Single atomic species," *Phys. Plasmas*, vol. 17, no. 1, pp. 1–13, 2010.

[20] G. A. Emmert and J. F. Santarius, "Atomic and molecular effects on spherically convergent ion flow. II. Multiple molecular species," *Phys. Plasmas*, vol. 17, no. 1, p. 13503, Jan. 2010.

[21] M. K. Michalak, "Increasing the High Voltage Capabilities and Exploring Parameter Space of an Inertial Electrostatic Confinement Fusion Neutron Source for the Detection of Chemical Explosives," Ph.D. dissertation, University of Wisconsin-Madison, 2017.

2. Previous Work on Inertial Electrostatic Confinement Devices

An introduction to the working principles and past studies of inertial electrostatic confinement devices is presented in this chapter. Numerous previous studies of the IEC device have informed theoretical understanding of device operational regimes, and extensive diagnostic work at the University of Wisconsin-Madison has experimentally studied particle distributions for IEC devices. The understanding gained from these past works has informed the theory of operation, which may be used to predict the neutron production scaling of the device at higher operational voltages and is discussed in Chapter 3. To achieve higher voltage operation, the development of a specialized, new vacuum-compatible electrical feedthrough has been the subject of research efforts in the past by the University of Wisconsin-Madison and other research institutions. A review of these past developments is presented here.

2.1 The inertial electrostatic confinement fusion device

The use of an electrostatic confinement device to create a potential trap as seen in Figure 2-1 for the confinement and acceleration of ions to fusion relevant energies was first conceptualized by Elmore, Tuck, and Watson [1]. Using a positively biased grid, electrons are injected into the center of the device creating a virtual potential well to accelerate the positive ions which may collide and fuse. Experimental work on electrostatic confinement for fusion was first conducted by Farnsworth and Hirsch who replaced the positive grid with a semi-transparent, negatively biased grid to accelerate the ions toward the center of the device [2]. This simplified gridded cathode concept is the basis of the IEC devices used at several universities and institutions,

including at the University of Wisconsin-Madison, and this concept is discussed with more detail in Section 2.1.2.

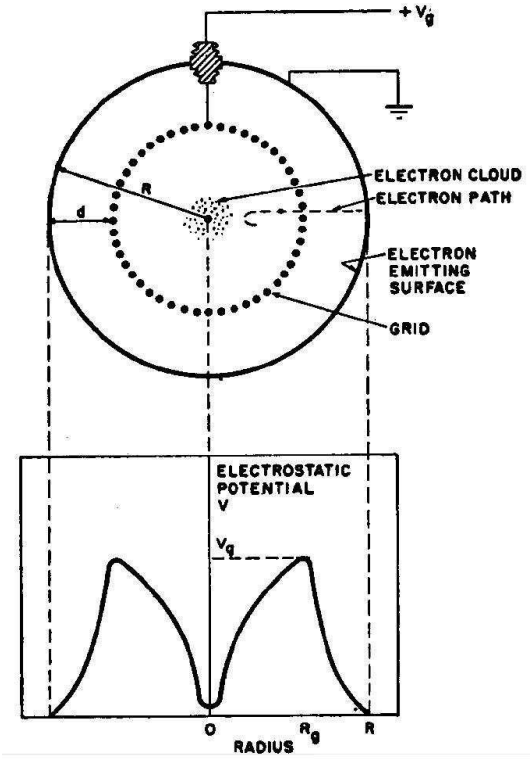

Figure 2-1. Original electron-injected IEC concept by Elmore, Tuck, and Watson [1].

Since these devices were first proposed, several academic, government, and private research programs have studied inertial electrostatic confinement for fusion production and are listed in Table 2-1. A history of the early development of inertial electrostatic confinement fusion work and a comprehensive review of work published by the research community has been well documented in a book published by Miley and Murali [3].

Table 2-1. Contributors in the IEC Fusion Research Community, adapted from [4].

	Laboratory	D-D	D-^{3}He	^{3}He-^{3}He	D-T	
United States	Inter. Tele. And Telegraph (Farnsworth/Hirsch)	X			X	Industry
	Directed Technologies Inc.	X				
	Energy Matter Conversion Corp. (EMC2)	X				
	FP Generation	X				
	Rockford Industries	X				
	Starfire Industries	X				
	Idaho National Lab	X				Gov't
	Los Alamos National Lab	X				
	Marshall Space Flight Center	X				
	University of Illinois	X				University
	University of Wisconsin	X	X	X		
	University of Maryland	X				
	MIT	X				
	University of Missouri*					
International	Kyoto University (Japan)	X	X			
	Kansai University (Japan)	X			X	
	Osaka University (Japan)				X	
	Tokyo Institute of Technology (Japan)	X				
	University of Sydney (Australia)	X				
	Canada*					Mixed
	NSD-Fusion (Germany)	X				
	India	X				
	Russia	X				
	Iran	X				
	China	X				

*Theory based programs

2.1.1 U.S. and international university contributions to IEC development outside the University of Wisconsin

Most of the recent studies published in the last 20 years on inertial electrostatic confinement devices have originated from universities in the United States, Japan, and Australia, listed in Table 2-1. At the University of Illinois at Urbana-Champagne (UIUC), experimental studies have been conducted on fundamental research of glow discharge IEC devices [5] and on applications of IEC devices used as radiation sources [6] or space propulsion [7]. Advanced gridded IEC concepts have also been studied by researchers at MIT and the University of

Maryland, which look at the use of multiple concentric grids to enhance focus and confinement of particles [8], [9]. Researchers at Kyoto University in Japan have studied gridded IEC devices theoretically and experimentally to develop compact IEC neutron generators for the detection of conventional explosives [10]–[12], and at the Tokyo Institute of Technology, experimental and simulation work has been conducted to look at enhanced ion confinement [13] and proton sources for positron emission tomography isotope production [14]. At Kansai University in Japan, a campaign to study deuterium-tritium fusion reactions using an IEC device has been pursued in collaboration with Osaka University [15]. The University of Sydney in Australia has worked on simulation and experimental studies of gridless multi-cusp inertial electrostatic confinement devices [16], [17].

2.1.2 University of Wisconsin-Madison contributions to IEC development

The University of Wisconsin-Madison has conducted extensive research on the experimental and theoretical operation of IEC devices and applications of these devices as radiation sources [18], and several of these studies will be discussed in the following sections. The inertial electrostatic confinement device uses a potential structure, and a source of ions is needed to create the conditions necessary for fusion reactions and was first studied by Thorson at the University of Wisconsin [19]. Figure 2-2 shows a schematic of this gridded IEC experiment, named HOMER. A spherical gridded cathode is suspended within a vacuum chamber, and a highly negative voltage is applied with respect to a grounded anode grid to create a potential well. Ions in this device are generated either by filament assisted electron impact ionization or by operating in a glow discharge regime. Typical device operating parameters in HOMER are: cathode voltage from 30 to 200 kV, cathode currents 30 to 100 mA, and background gas pressure from 0.3 to 2

mTorr (0.04-0.27 Pa). Fusion reaction products are measured using charged particle detectors mounted to the device or an external neutron detector. The actual HOMER IEC device and a view of the gridded electrodes during glow discharge operation are pictured in Figure 2-3.

Several diagnostics approaches have been adapted to IEC devices to better characterize the complex particle interactions within the device, and a comprehensive review has been provided by Miley and Murali [3]. A summary of selected diagnostic work conducted at the University of Wisconsin-Madison and the results pertaining to the proposed research are discussed in the following sections.

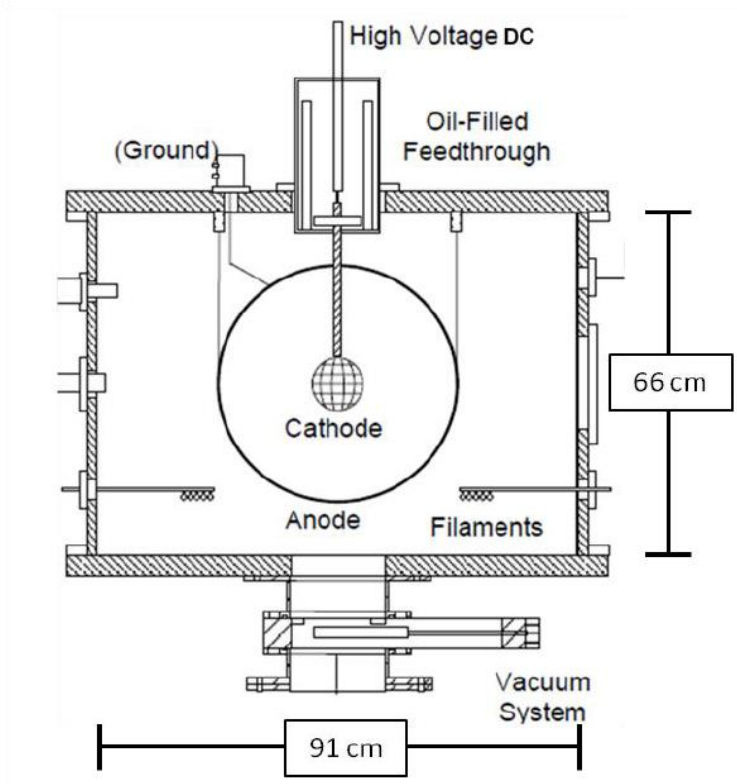

Figure 2-2: Schematic of a Gridded IEC Device, HOMER, at the University of Wisconsin-Madison.

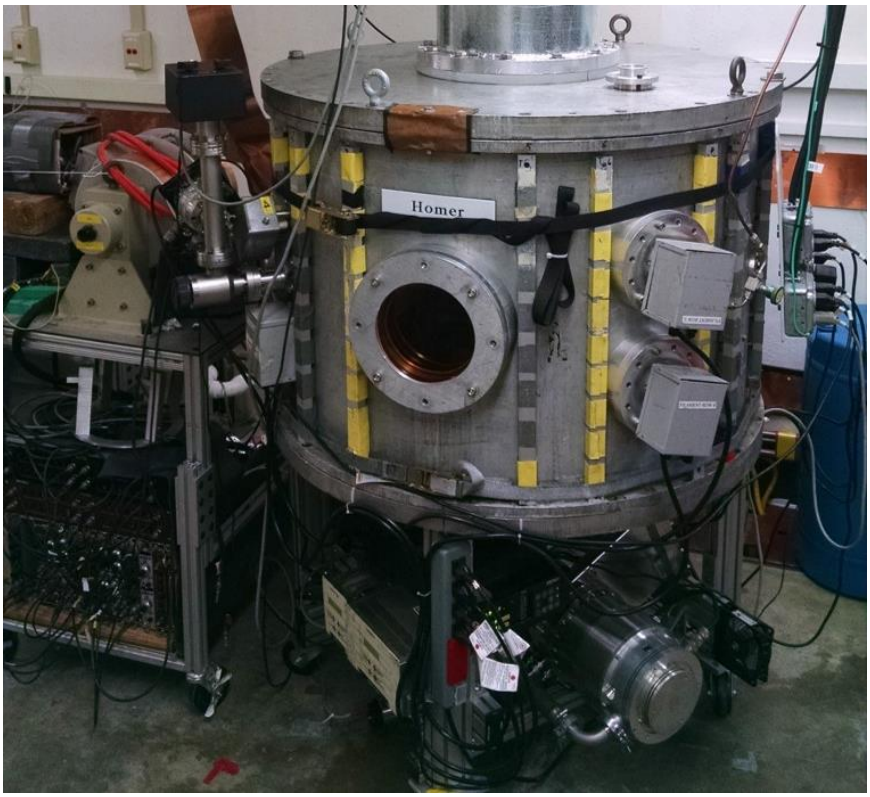

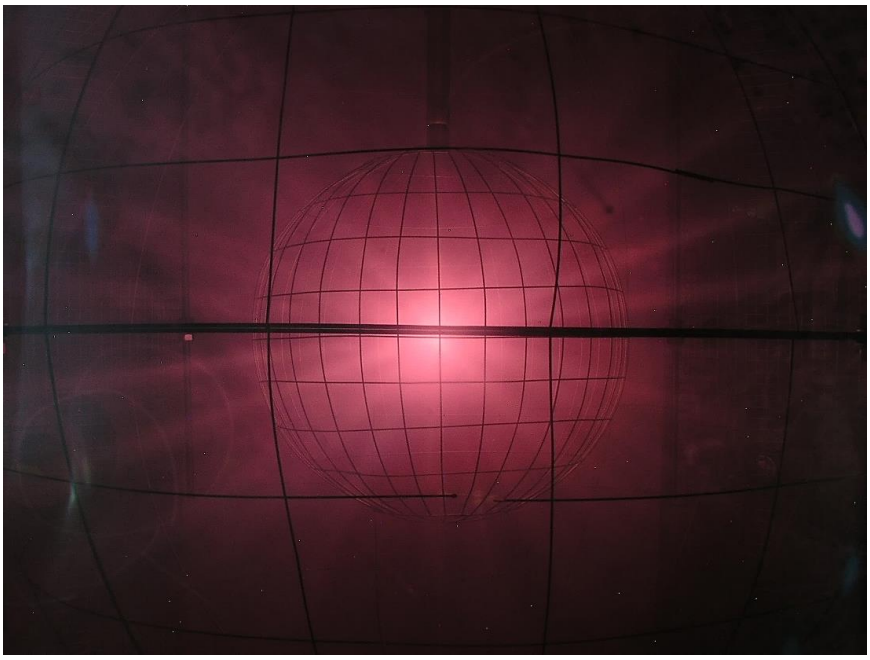

Figure 2-3: (Top) Photo of the HOMER IEC experiment at the University of Wisconsin-Madison, (Bottom) an inside view of the grids during glow discharge operation.

2.1.2.1 Fusion Ion Doppler-Shift (FIDO)

A Fusion Ion Doppler-Shift diagnostic was developed by Boris to measure the Doppler shift in reaction product velocities due to the center of mass velocity of the reacting ions [20]. This diagnostic, pictured in Figure 2-4, uses a magnetic field to selectively bend charged particle trajectories based on their momentum into a detector. Charged particles and x-rays streaming from the reaction chamber travel down a tube where they are collimated, and a tuneable electromagnet bends the charged particle flight path. The electrons and x-rays are prevented from reaching the detector by colliding with the wall, and only charged particles with the proper momentum and charge are transmitted to the detector.

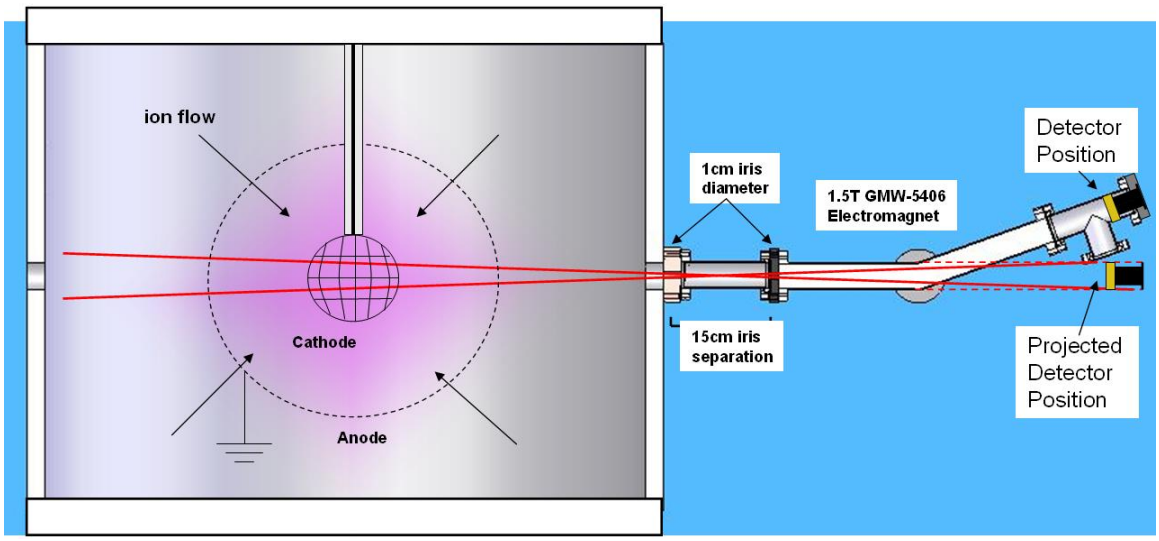

Figure 2-4: Schematic view of the FIDO diagnostic [20].

This diagnostic was used to infer the reacting ion energy distribution from the Doppler shift in the reaction product velocities for a range of cathode voltages, cathode currents, chamber pressures, and grid geometries. Figure 2-5 shows a typical spectrum measurement with the Doppler

shifted proton peaks from D+D → p(3.02 MeV) + T(1.01 MeV) reactions. Using this diagnostic, Boris [19] concluded that the energy distribution at 1.25 mTorr D_2 background pressure is dominated by 10-20 keV deuterons in HOMER for cathode voltages ranging 50-100 kV and that increasing the cathode voltage results in a modest increase in the mean and peak velocities of the deuterium energy spectra at 1.25 mTorr.

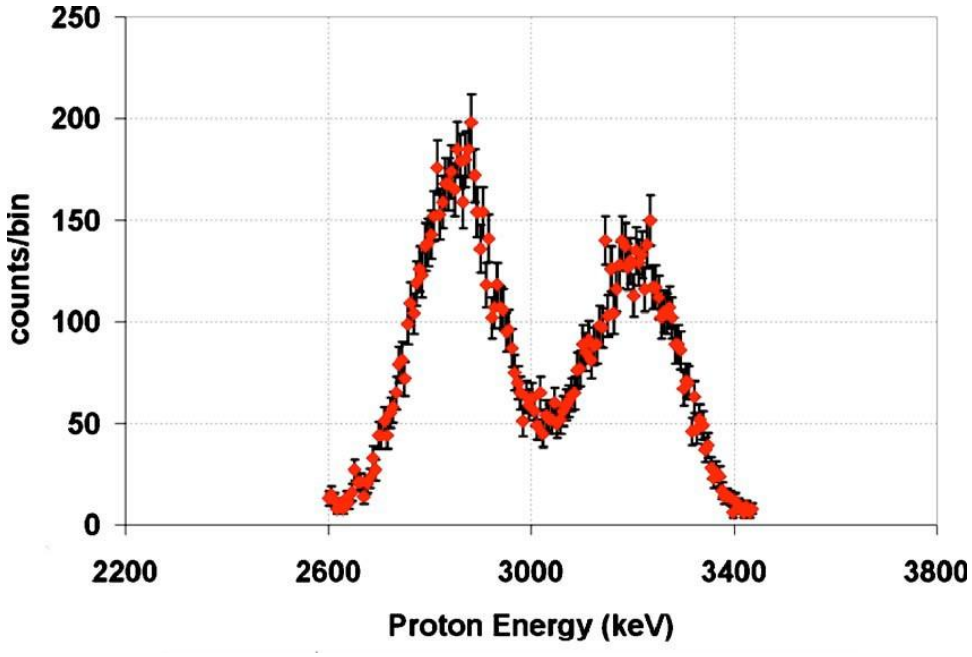

Figure 2-5: Experimentally measured D-D proton energy spectrum using the FIDO diagnostic for HOMER operation at 70 kV, 30 mA, 1.25 mTorr D_2 [20].

2.1.2.2 Time of Flight Diagnostic

By aligning two FIDO diagnostics opposite each other along a chord line through the device center, a time of flight (TOF) measurement can be made by coincidence counting of the reaction products shown in Figure 2-6. The time of flight information is used to reconstruct the radial profile of the proton-tritium producing channel of D-D fusion reactions within HOMER;

profiles using the TOF diagnostic were first studied by Boris [20] and later by Donovan [21] and McEvoy [22].

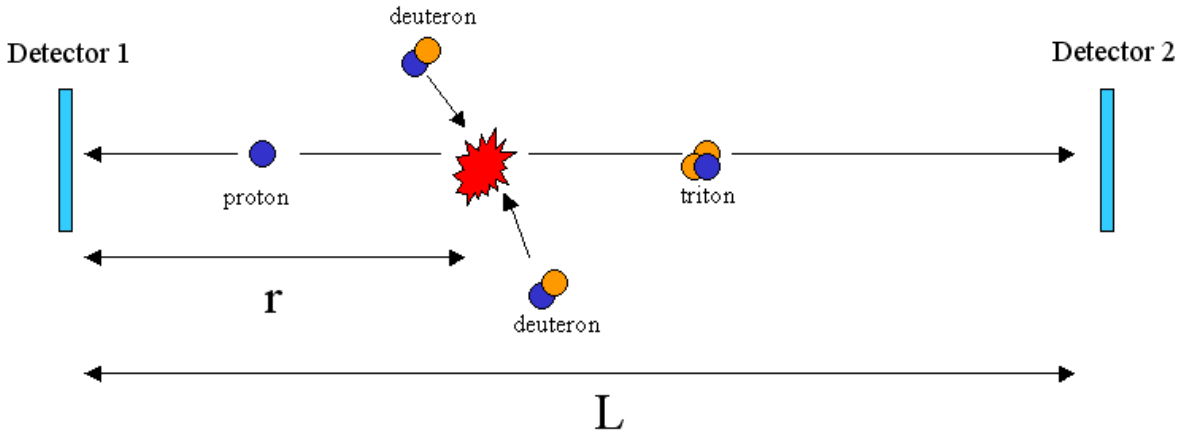

Figure 2-6: Reacting particles may be spatially located by coincidence counting and measuring the reactants time of flight [21].

The results from these time of flight measurements showed a spatial reaction profile strongly peaked in the center of the spherical cathode grid with a symmetry about the center of the device and showed fusion rates are higher in microchannel regions, ions able to flow through grid openings, than in regions where grid wires obstruct ion flow [21]. A detailed model developed by McEvoy carefully weighed the physical factors that may affect the accuracy of the time of flight results, and he was able to construct a more accurate profile of measured fusion events shown in Figure 2-7 [22].

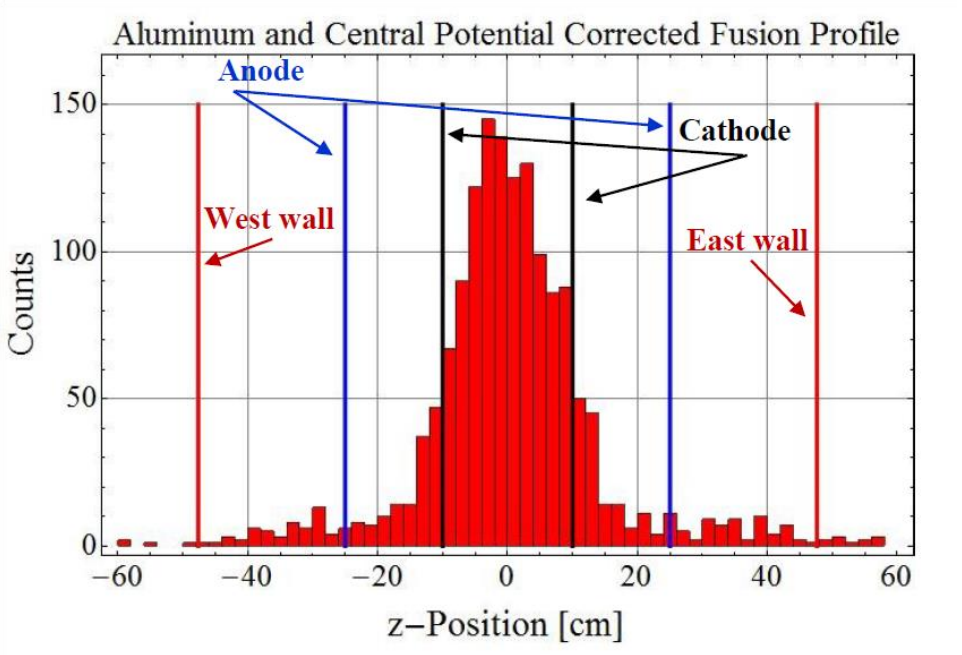

Figure 2-7: Spatial distribution of DD fusion reactions inside HOMER operating at 60 kV, 30 mA, and 1.5 mTorr D_2 [22].

2.1.2.3 Negative Ion Measurements

Initial results from the FIDO diagnostic work suggested the presence of deuterium anion formation in the IEC device [23], and a detailed study of negative ion formation was conducted by Alderson [24]. A movable Faraday cup was positioned outside the spherical anode grid to measure the profile of negative ions streaming radially outward from the HOMER device center. Figure 2-8 shows a peaked profile of negative ions leaving the device from an azimuthal scan in the microchannel region between two of the cathode grid wires, and an increase of negative ions with applied cathode voltage. Alderson showed that negative ion formation in the device increases linearly with cathode current, increases with cathode voltage, and decreases when the deuterium chamber pressure is increased from 2 to 4 mTorr.

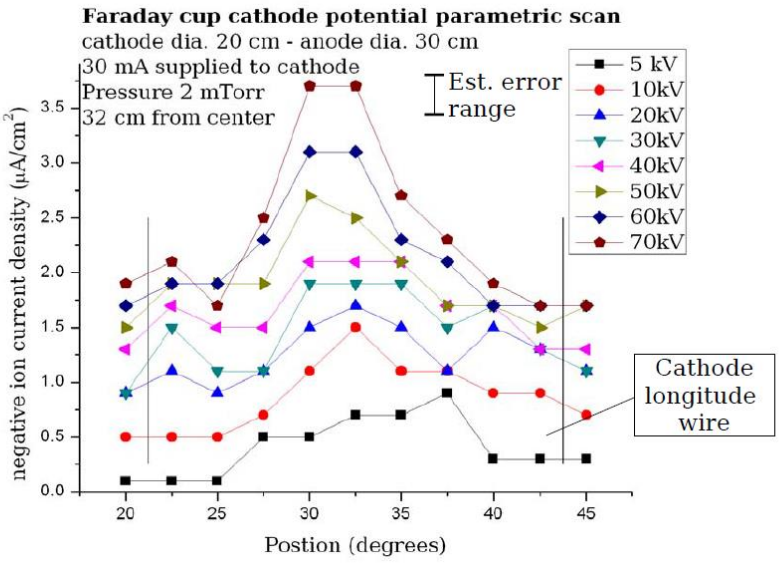

Figure 2-8: Azimuthal profile of negative ions streaming radially outward between cathode grid wire segments [24].

2.1.2.4 Neutral Particle Analyzer

A neutral particle analyzer was developed by Becerra as a diagnostic approach to study the energy distribution of neutral particles escaping from device confinement [25]. The analyzer used a thin carbon stripping foil to remove charge from the fast neutral particles before reaching an electrostatic bending stage, as pictured in Figure 2-9. Particle trajectories are bent based on their incident energy, allowing for only selected particle energies to be transmitted to a charged particle detector.

Measurements were taken of neutral particle energy distributions for two different deuterium chamber pressures in HOMER using a filament assisted mode. Data shown in Figure 2-10 using this diagnostic present a complex distribution of peaks in the neutral particle energy spectrum while using the IEC device in a filament assisted operating mode. Becerra concluded

that the prevalence of D_3^+ ions and negative ions in the source plasma may allow for many additional atomic and molecular reaction channels that may create such a complex structure.

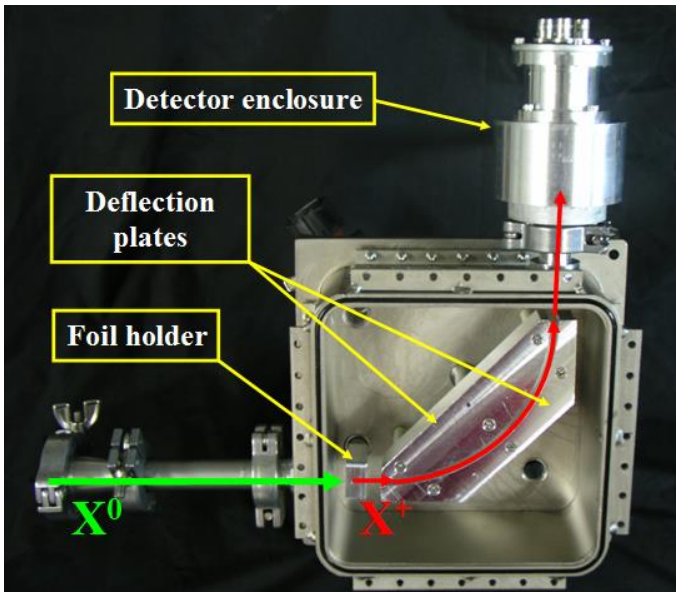

Figure 2-9: Flight path of particles through the neutral particle analyzer diagnostic [25].

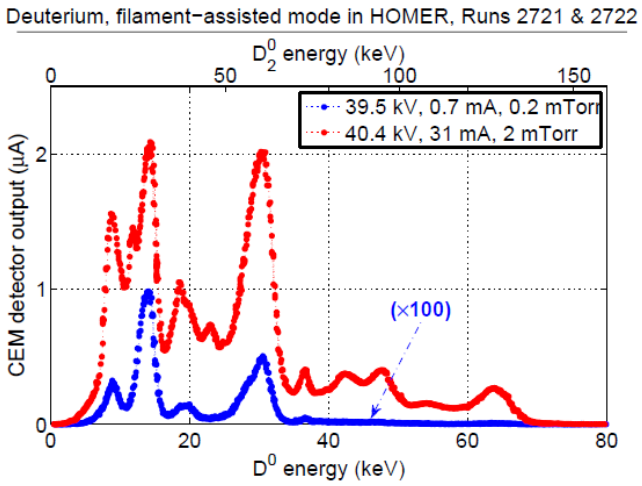

Figure 2-10: Energy distribution of fast neutral deuterium particles streaming outward from the center of HOMER during filament assisted operation [25].

2.1.2.5 Previous IEC device parameter study at voltages above 150 kV

An investigation of the neutron production rate scaling with cathode voltage, cathode current, and chamber pressure in the HOMER device for cathode voltages up to 175 kV was pursued by Michalak [26], [27] . To achieve reliable high voltage operation above 150 kV, a new multi-staged feedthrough design was developed, and the details of this hardware design are discussed in Section 2.2.2.3. Michalak was able to measure the neutron generating yield of the device for variations of the cathode voltage from 30 to 175 kV, cathode current from 30 mA to 100 mA, and for deuterium chamber pressures of 0.3 mTorr and 1.0 mTorr; these measurements are shown in Figure 2-11 and Figure 2-12. Michalak found the neutron rate scaling at these cathode voltages and pressures varied linearly with the device cathode current, and at cathode voltages above 50 kV, the neutron production rate scaling was also seen to vary linearly with voltage. A peak steady state D-D neutron production rate of 3.3×10^8n/s at 175 kV, 100 mA, and 1.0 mTorr D_2 was achieved in the HOMER IEC device.

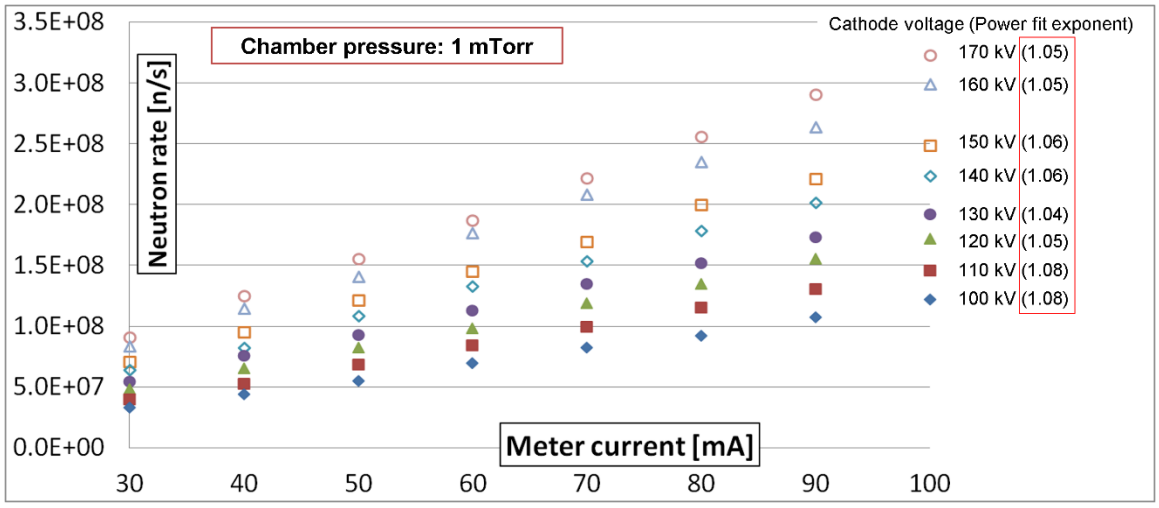

Figure 2-11: Neutron production rate scaling with cathode current shows near linear scaling of rates with cathode voltages ranging 100-170 kV [27].

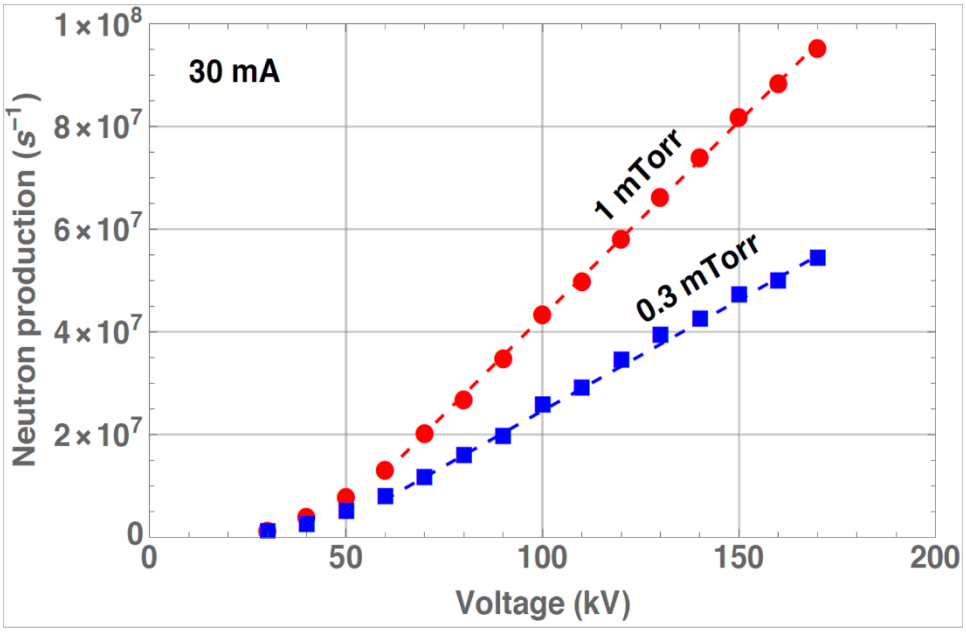

Figure 2-12: Neutron production measurements show near linear scaling of rates for HOMER with a 20 cm dia. cathode and 50 cm dia. anode configuration [27].

During the high voltage conditioning process of the new feedthrough hardware, Michalak noted a general upward trend in neutron production rate from the device while operating the same parameters over a period of many days. This upward trend shown in Figure 2-13 showed a factor of 4 for 30 kV and a factor of 3 for 80 kV improvement in device performance over a span of 57 days. Michalak concluded that the neutron production rate performance increase was partly due to the vacuum conditioning and removal of impurity gas sources over time and postulated that a buildup of deuterium targets in the chamber walls may also contribute to the increase in neutron production performance.

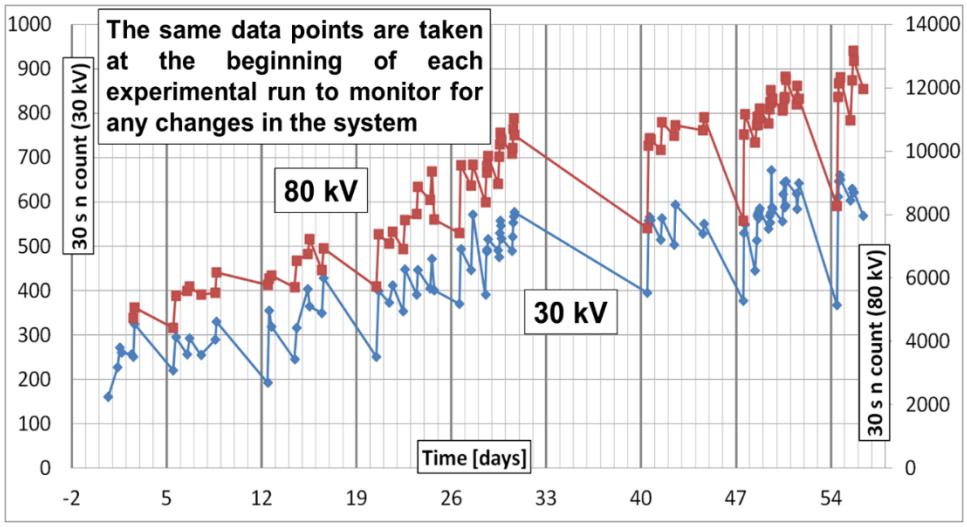

Figure 2-13: Neutron counts taken under the same device set points at the beginning of each run show an upward trend in neutron production over time [27].

2.2 High voltage feedthrough design for IEC devices

The engineering challenge of transporting high voltage through a grounded enclosure is not unique to IEC devices and is commonly implemented in power transmission, plasma systems, particle accelerators, spacecraft, and numerous other instruments used in scientific and medical fields. What sets the IEC fusion devices apart from these applications is the demand to standoff tens to hundreds of kilovolts during the generation of energetic charged particles and radiation to the electrodes and insulating materials. In a gridded IEC system, this high voltage must be fed through a grounded chamber boundary and connect to the cathode via a ridged support, sometimes referred to as a high voltage stalk. While commercial high voltage vacuum feedthroughs do exist, they are not typically designed with a sufficiently ridged center conductor to support the cathode and are not readily available at voltages greater than 100 kV standoff. Custom high voltage

feedthroughs have been in development at the University of Wisconsin-Madison to meet the demand of the gridded IEC environment and to push the voltage boundaries beyond the limits of commercially available products. A timeline of progress in increasing the cathode grid operational capabilities is shown in Figure 2-14. Work performed by the author and collaborators has led to the development of hardware capable of operating with cathode voltage of 210 kV, a 24% improvement over peak operating conditions from efforts prior to the author's involvement.

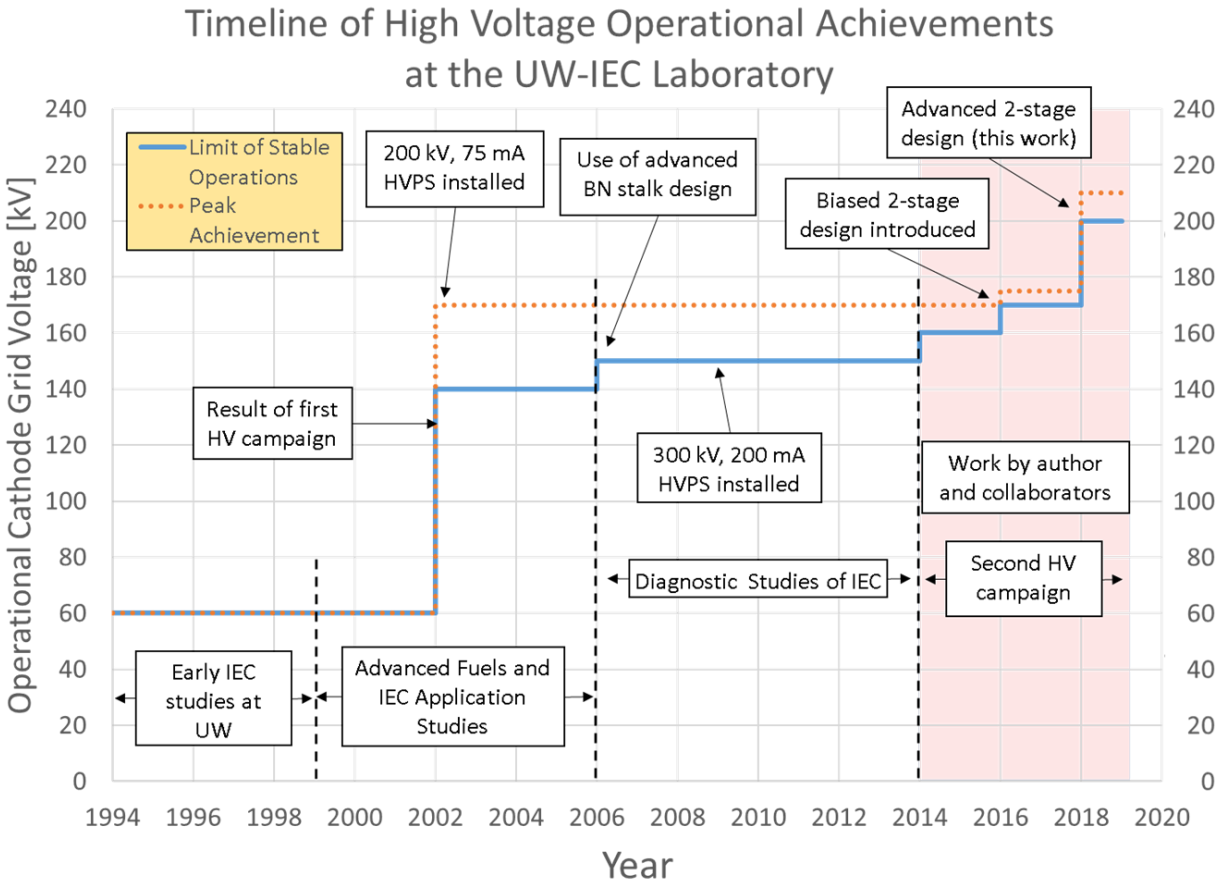

Figure 2-14: Progress in the development of high voltage capabilities at the University of Wisconsin-Madison IEC Laboratory.

2.2.1 Previous high voltage feedthrough work at the UW-Madison IEC Laboratory

High voltage feedthrough and stalk design has been an integral part of the development of gridded IEC devices since the beginning of the program at the University of Wisconsin-Madison. The earliest designs used a 100 kV commercial feedthrough that was modified by adding a vacuum-tight radial compression fitting to the high voltage lead of the feedthrough to allow flexibility in axial grid location and rotation for ease of alignment [28]. These early designs typically included an alumina insulating sleeve, which shields the center conducting stalk from ion bombardment and extends from the bulk insulator to the cathode grid. There were two issues with this early design. First, a metalized coating, probably caused by ion sputtering of the cathode material over time, would cover this ceramic sleeve, leading to the formation of a conductive surface breakdown path. Second, the cathode voltage was limited to 100 kV operations, and any studies to be made at higher voltages would need a different feedthrough design.

A novel feedthrough design was created at the University of Wisconsin-Madison to extend the IEC operational capability greater than 100 kV operation, and this approach replaced the modified commercial 100 kV feedthrough with a custom-made conductor and insulator combination [29]. Figure 2-15 shows a schematic of two variants of the insulator-conductor stalk designs used. In this approach, a 4.8 mm diameter molybdenum rod was used as the center conductor of the stalk, which connects the grid to the high voltage power supply cable through the vacuum barrier. The molybdenum rod is epoxied to a hollowed 2.54 cm diameter boron nitride insulator to provide voltage standoff, and a compressed nylon ferrule is used around the boron nitride insulator to create a vacuum seal. The non-vacuum side is immersed in a dielectric oil where the high voltage power supply cable connection was made. Boron nitride was chosen as an electrical insulator for its excellent bulk dielectric strength of 67 kV/mm, operational temperature

up to 1150 ºC, and machinability to make custom geometries. Due to the porous quality of the boron nitride insulator, the oil immersed surfaces were coated with a thin layer of polyimide to prevent oil permeating the solid rod. This design was demonstrated to operate stably up to 150 kV and achieved peak standoff operation near 170 kV.

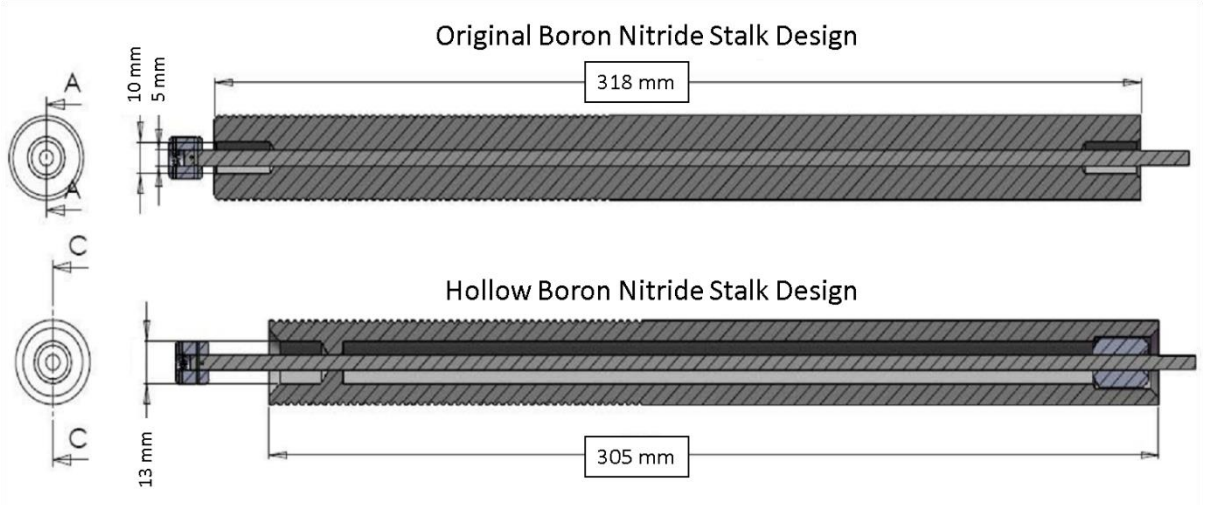

Figure 2-15: Boron nitride insulated stalk designs developed at the University of Wisconsin-Madison, adapted from [20].

The lifetime and durability of a stalk using this design were eventually found to be limited. This stalk still had issues where sputtered metal would collect on the insulator surface, giving it a finite lifetime before the insulating surface would form a conductive coating and need to be resurfaced. In the region near the compression fitting nut, high electrical stresses would result in partial discharge formation through the bulk insulating material leading to a pinhole type failure [29]. These pinhole failures of the stalk would compromise the electrical standoff and would often result in a vacuum breach. Additionally, the boron nitride insulator was found to be fragile in assembly, and the ceramic would tend to fracture if the compression fitting was overtightened.

In 2009, the laboratory received a new power supply capable of delivering -300 kV DC output up to 200 mA, and a new feedthrough design was pursued to accommodate the new voltage capabilities which sought to eliminate the electrical pinhole type failures that plagued the previous design. A new insulated feedthrough design was introduced by Donovan to improve standoff and reduce electric fields over the previously feedthrough stalk design by increasing the electrode gap distances using bulk insulators [21]. This design, pictured in Figure 2-16, moved the presence of any grounded surfaces away from the high voltage conducting rod by using a quartz bowl insulator to standoff and increase surface path length between the high voltage conductor and ground. The initial design was able to reduce the electric fields at the critical vacuum interface region as predicted by an electrostatic simulation as shown in Figure 2-17. This new design used a compression O-ring seal between a quartz bowl and the high voltage stalk; however, once the hardware was constructed and installed, the quartz insulator fractured under mechanical loading. A revised design by Becerra [25] was made using blue nylon type MC 901 as the insulator replacement and an added ceramic ion shield plate to protect the plastic from plasma degradation.

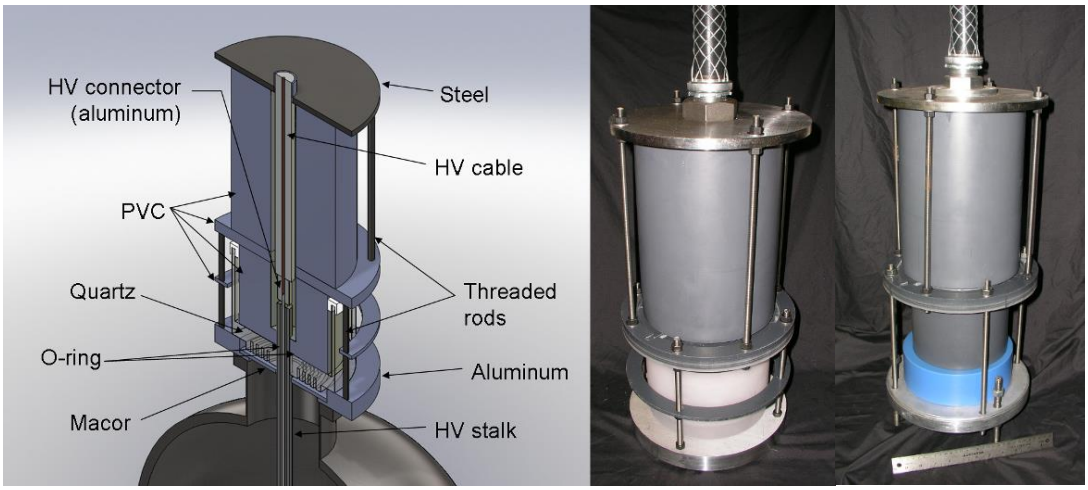

Figure 2-16: From left to right, 300 kV feed through design, assembled hardware with quartz standoff, and with blue nylon standoff [25].

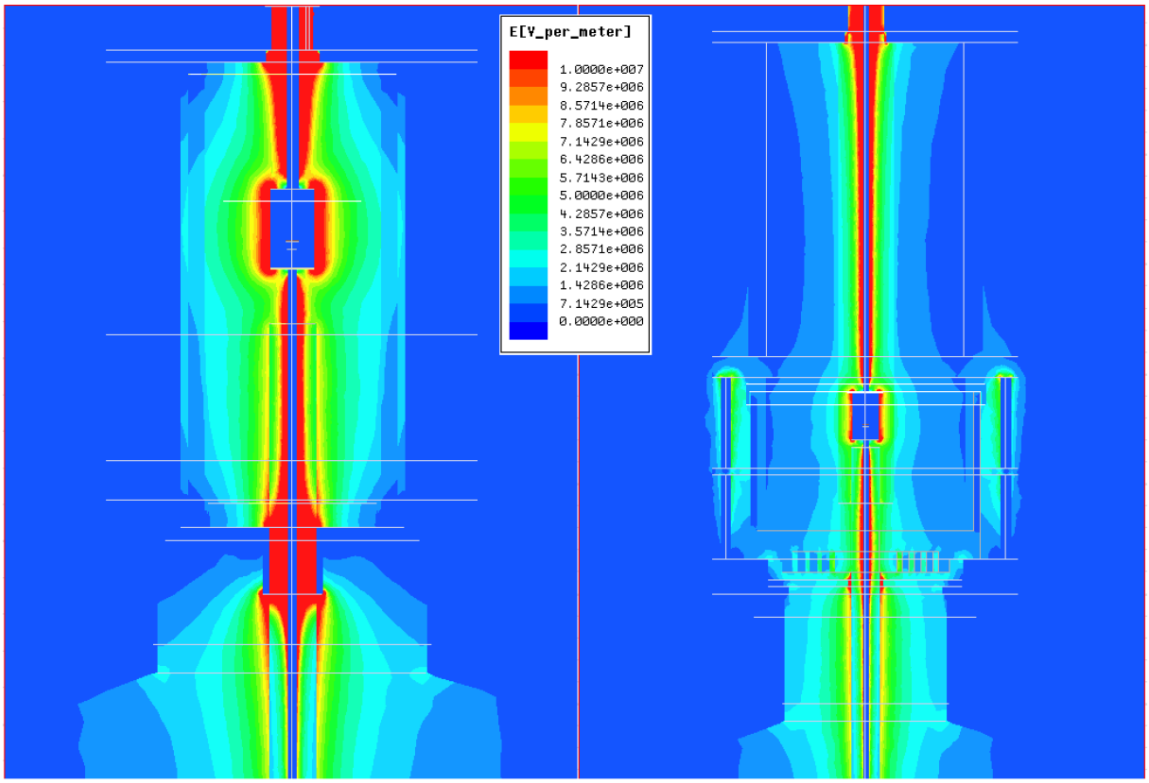

Figure 2-17: A reduction of fields is achieved in the insulating design (right) compared to the boron nitride stalk design (left) using ANSYS Maxwell simulation of electric field inside the high voltage feedthrough designs at an applied voltage of 250 kV [21].

The author, in collaboration with Michalak, was involved with the iterative design and testing of high voltage hardware for operations beyond -200 kV [27], and a timeline of this hardware development and testing is shown in Figure 2-18. For this work, the author was responsible in part for testing, redesigning, and manufacturing parts of several feedthrough prototypes. Numerous flaws were found in the insulated feedthrough hardware design that were not anticipated from electrostatic modeling alone. Initial testing of the blue nylon configuration gave poor vacuum sealing performance by the radial O-ring compression against the coated boron nitride stalk, which resulted in dielectric oil being sucked into the chamber and compromised the vacuum system. The compression O-ring seal was replaced by epoxying the stalk to a small diameter ceramic disk and using an O-ring face seal between the blue nylon and ceramic to hold vacuum. This configuration achieved a peak operating voltage standoff of -175 kV before a destructive arc passed across the O-ring vacuum seal between the HV cable connecter and the plasma facing insulator, resulting in a major vacuum breach and a large dielectric oil contamination in the chamber.

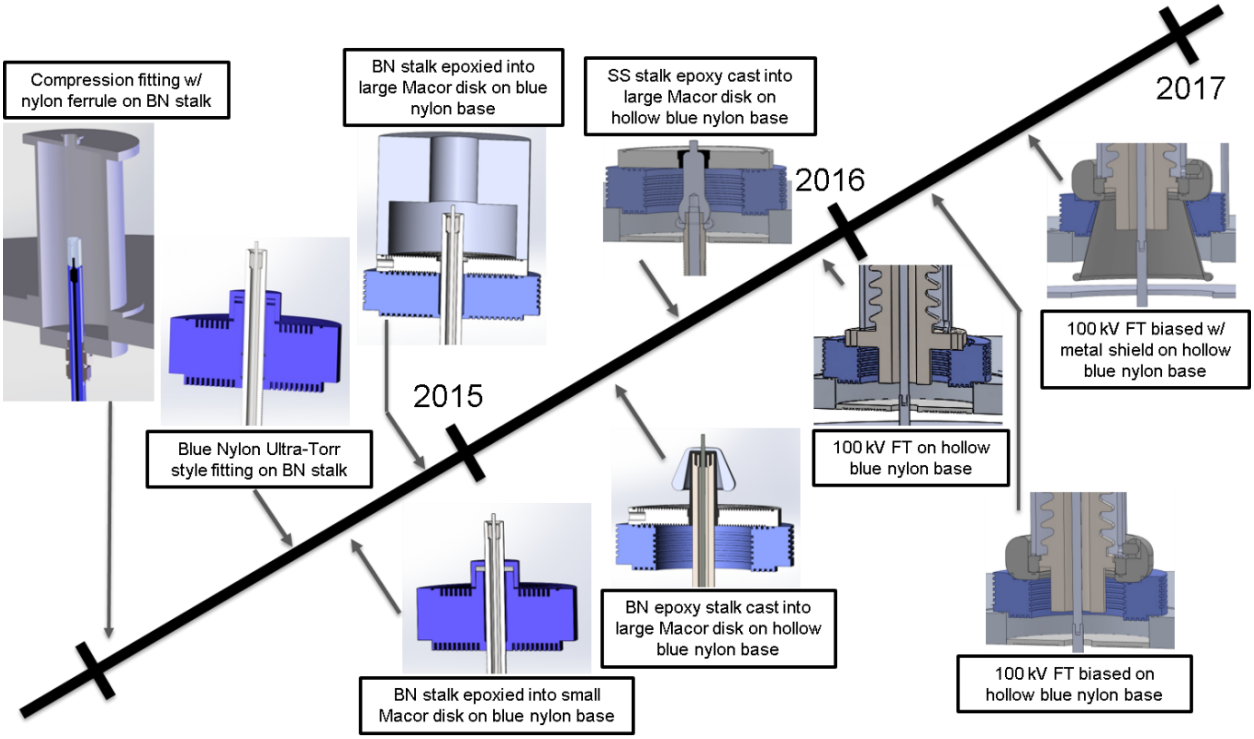

Figure 2-18: Timeline of feedthrough designs tested in pursuit of a robust feedthrough for high voltages greater than 150 kV.

The next iteration attempted to prevent this issue from happening again by potting in the boron nitride stalk to a 17.8 cm diameter machinable ceramic disk using a dielectric epoxy and moving the O-ring seal to outside the oil-vacuum boundary. To avoid void formation, a mold casting procedure was co-developed by the author which used a vacuum grade, low viscosity epoxy, where the mixture is degassed under low vacuum, gently heated to lower its viscosity, and flowed into the casting mold using a syringe to avoid trapping air bubbles. The epoxied assembly is then cured using an oven. Figure 2-19 shows two prototypes of epoxy cast high voltage stalks constructed for testing.

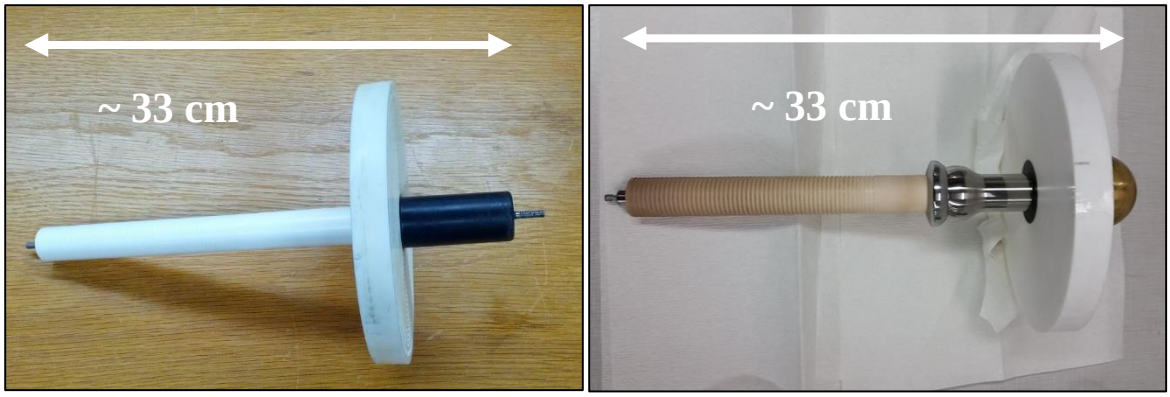

Figure 2-19: Feedthrough prototype using boron nitride stalk with molybdenum conductor epoxy casted to ceramic plate (left) and a prototype using a metal conductor epoxy cast to ceramic plate (right).

The epoxy casted boron nitride stalks all failed when high voltage conditioned to near -150 kV. In each case the failure was an electric arc tracking along the epoxy interface resulting in a vacuum breach; autopsies were conducted in each case to find the failure mechanism. It was suspected that voids were the cause of failure, and indeed the initial stalks were found to have significant voids in the epoxy. However, a revised epoxy selection chosen by the author and procedures co-developed by the author eliminated voids found in the next round of epoxied stalks, yet they failed in the same manner. It is now believed that significant charge build-up occurred on the insulating surface until a destructive discharge path formed along the epoxy and insulator boundary.

A revised design developed by Michalak aimed to eliminate electrical failure through a vacuum barrier by allowing the molybdenum center conductor to be exposed to the chamber on the vacuum side of the insulator [27]. This design prevents any excessive charge build-up to find a discharge path without breaking vacuum. The design was successful in eliminating any further vacuum breaches during failure; however, testing done by the author showed electrical failures in

the range of -120 kV to -150 kV were still a persistent issue where charge may build up on insulators used to shield the primary insulating standoff. Numerous configurations of this non-conductive, insulating feedthrough design were tried, but none showed drastic improvement. The next feedthrough design pursued sought to use a multi-staged standoff technique to improve the high voltage capability for the HOMER device.

2.2.2 The multi-stage high voltage feedthrough approach

One advanced concept of high voltage feedthrough design uses multiple nested electrodes biased or floated to intermediate voltages between the center conductor and grounded enclosure. By controlling the gap voltages, the peak electric field in the design may be reduced, allowing improved standoff capability; the high voltage engineering principles and theory of breakdown are discussed in Chapter 3. The use of multi-staged voltage standoff platforms to control electrical stress is not a new idea, and this concept has been used in power transmission high voltage bushings [30] and high voltage accelerator columns [31]. Additionally, this multi-staged approach has been pursued at other institutions which have sought to develop high voltage vacuum feedthroughs at voltages greater than 100 kV.

2.2.2.1 ITER 1 MV neutral beam injector feedthrough

The neutral beam injectors for ITER have been designed for 1 MV operation using a multiple stage electrostatic shield approach [32]. Figure 2-20 shows a schematic of a 1 MV bushing test bed called SINGAP used to validate the design concepts used for the ITER high voltage feedthrough. In this design, a resistive voltage dividing circuit is used to bias nine intermediate voltage stages between the 1 MV center conductor to ground resulting in a 111 kV standoff

between each gap. Nested cylindrical electrodes are used to control the electric fields and shield the insulators from charged particle bombardment on the vacuum side, and the non-vacuum side is insulated using a pressurized SF_6 vessel.

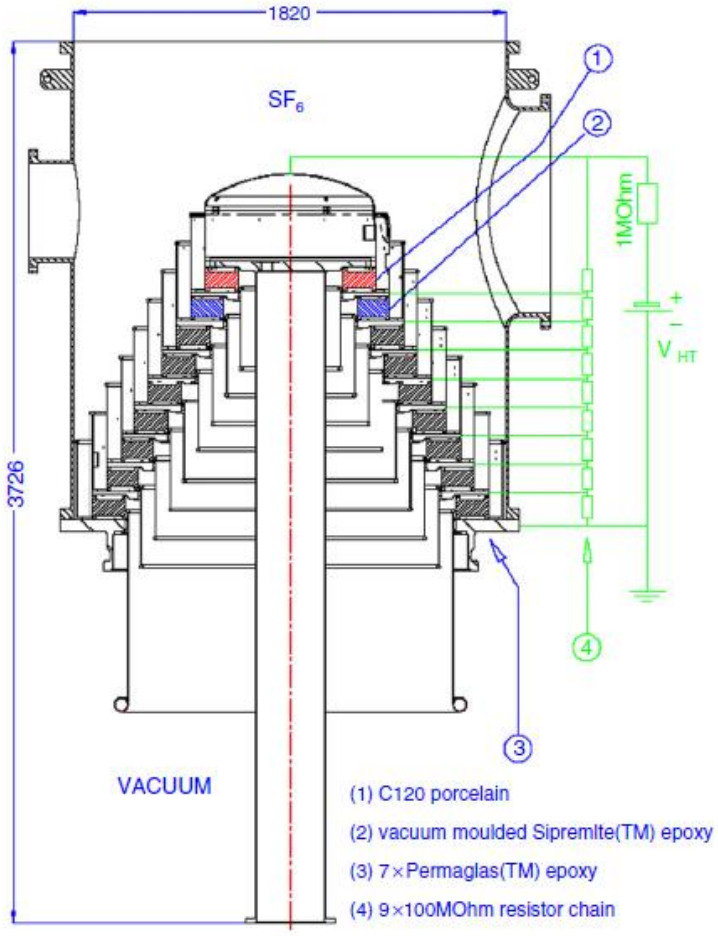

Figure 2-20: Schematic of the SINGAP test bed 1 MV feedthrough in development for the ITER neutral beam injectors [32].

A conservative electrostatic field limit of 40 kV cm^{-1} was chosen as the maximum field on the high vacuum cathodes to provide an adequate factor of safety for voltage standoff in the range of 100-200 kV. Figure 2-21 shows a 2D axisymmetric electrostatic model of the voltage stage and

insulating gap was created to analyze the fields at the critical regions. The results of the SINGAP test bed showed that this multi-staged voltage dividing technique is successful at controlling the electrical stresses in the feedthrough gap and insulating junctions.

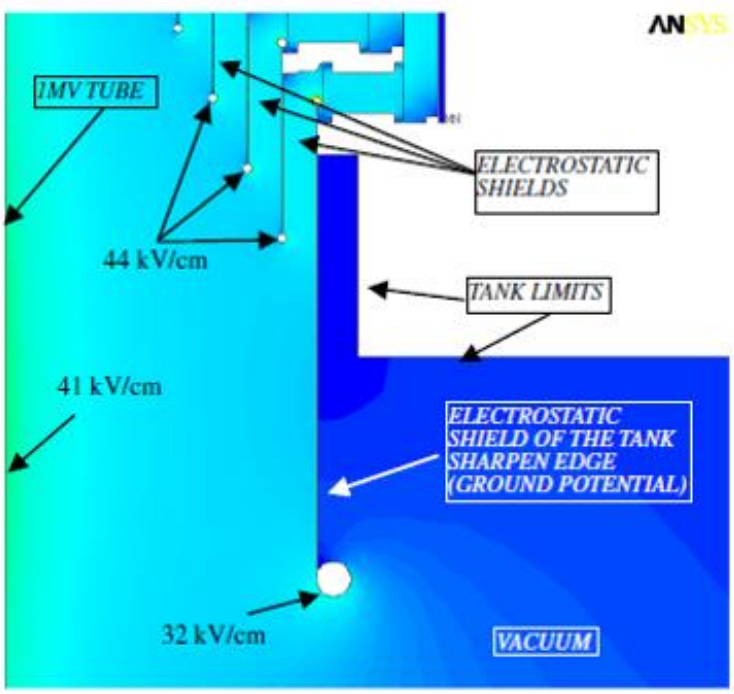

Figure 2-21: Modeling of the electrical stresses at the electrostatic shields in the SINGAP feedthrough [32].

2.2.2.2 Kyoto University multi-stage IEC feedthrough

The multi-staged feedthrough approach was first applied to an IEC device feedthrough at Kyoto University in Japan to for the purposes of improving the spherical symmetry of the electric field around the high voltage stalk to enhance ion recirculation and to improve the high voltage standoff [33]. Figure 2-22 shows this design which uses five stages to grade the voltage along the length of the feedthrough and shape the electric field. Each stage is connected by a resistance of

80 MΩ to drop the voltage by 40 kV when 200 kV is applied to the center conductor and cathode. This results in a drain current of 0.5 mA along the resistance path of the feedthrough. On the vacuum side, the electrostatic shields consist of nested solid annular tubes in the feedthrough column and transition to transparent grids in the chamber region. This design uses no insulating surface to protect the center conductor from charged particle bombardment.

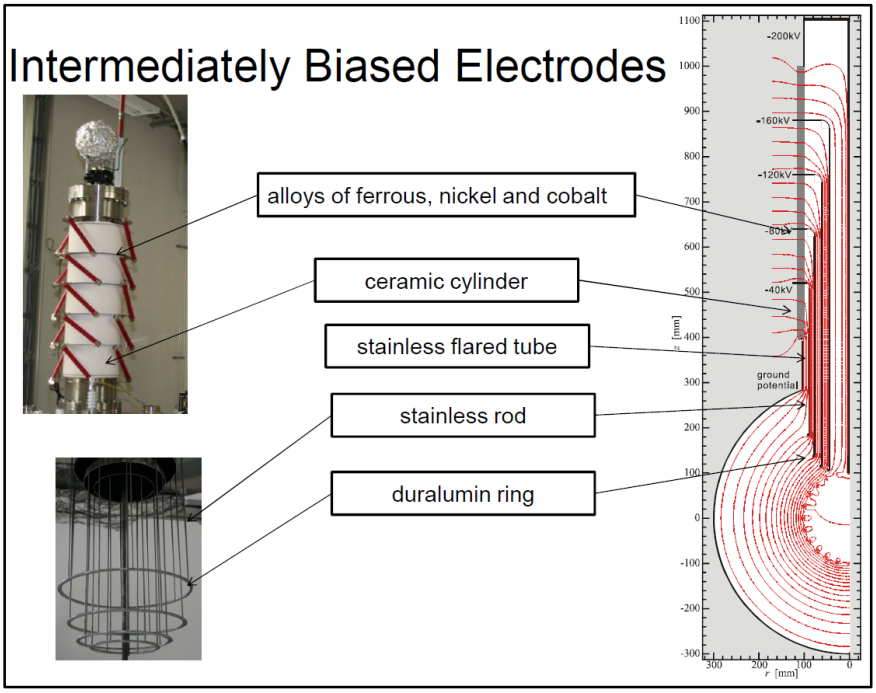

Figure 2-22: Kyoto University 200 kV 5-stage feedthrough design for an IEC device [34].

Initial results from testing this hardware showed the design was successful in conditioning up to 180 kV standoff without a plasma load and was successful in operating up to 130 kV under glow discharge conditions using a chamber deuterium gas pressure of about 0.32 Pa (2.4 mTorr) and cathode currents ranging from 10 to 30 mA [34]. Figure 2-23 shows calculations of the electrostatic potential structure in the inter electrode regions generated for single and multi-stepped

voltage designs and ion trajectories simulated using a particle-in-cell code to compare the ion recirculation paths for different electrostatic field structure designs [33]. The result was a factor of ~3 improvement in ion recirculation using a multi-staged feedthrough designed to increase field symmetry near the high voltage stalk. In addition to the 5-stage feedthrough design, a scaled down 120 kV 3-stage feedthrough design was also developed for work on compact IEC neutron sources for nondestructive inspection systems of special nuclear materials [10].

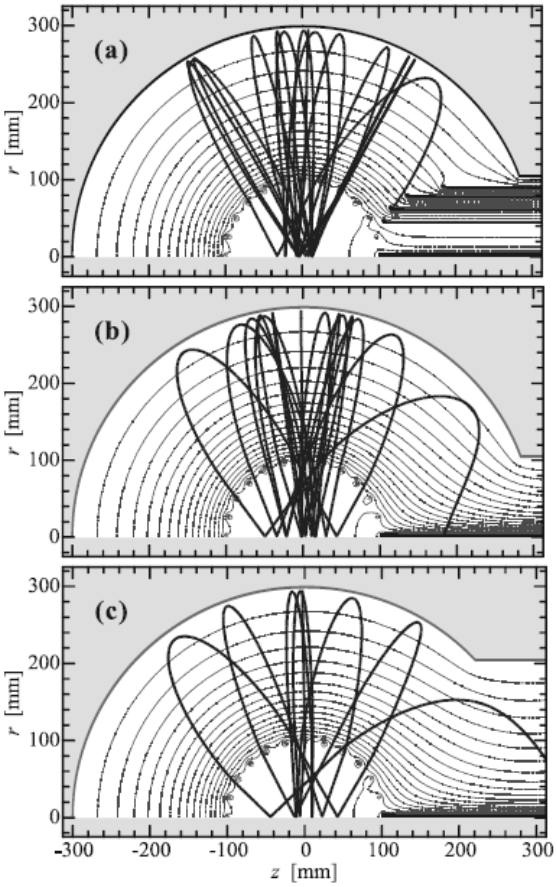

Figure 2-23: PIC simulation of ion trajectories show increased recirculation before reaching the high voltage stalk due to modified electrostatic field symmetry using a multi-staged approach [33]: (a) multi-staged potential shaping of the feedthrough, (b) narrow feedthrough port, (c) wide feedthrough port.

2.2.2.3 UW-Madison biased 2-Stage IEC feedthrough

Following the previous work of these multi-stage feedthrough approaches, a 2-stage feedthrough was constructed by Michalak which uses a modified commercially available off-the-shelf 100 kV vacuum feedthrough electrically isolated by a blue nylon standoff [27]. Figure 2-24 shows a model of the feedthrough that was tested on HOMER. A 12.7 mm diameter stainless steel rod was added to the commercial 100 kV feedthrough for rigidity and reduced electrical stresses. An electrical connection is made on the top using an aluminum ball to reduce stress at the cable connection, which is immersed in dielectric oil contained by a PVC sleeve. The torus platform is biased to a fixed voltage during normal operation to grade the electric field. In vacuum, a 12.7 mm diameter molybdenum conductor threads into the stainless steel conductor which supports the cathode grid. An electrostatic shield constructed from stainless steel is installed to prevent ions from reaching the inside of the feedthrough standoff where the blue nylon standoff is at risk of plasma degradation.

The vacuum flange of the alumina feedthrough is biased to an intermediate potential between the cathode and ground by an independent -75 kV power supply. The feedthrough power supply circuit, shown in Figure 2-25, uses a ballast resistor to protect the power supply from current transients due to arcing events and a megaohm resistance path to ground from over-volting the supply. By fixing an intermediate potential between the cathode and ground, the electric fields in the feedthrough region may be actively controlled. In operation, the voltage platform is set such that the design voltage of the 100 kV feedthrough is not exceeded across the bulk alumina insulator. The result of this design was the achievement of 175 kV cathode grid standoff with a current of 100 mA and chamber pressure of 1 mTorr D_2, yielding a neutron production rate of 3.3×10^8 neutrons/s in the HOMER IEC experiment.

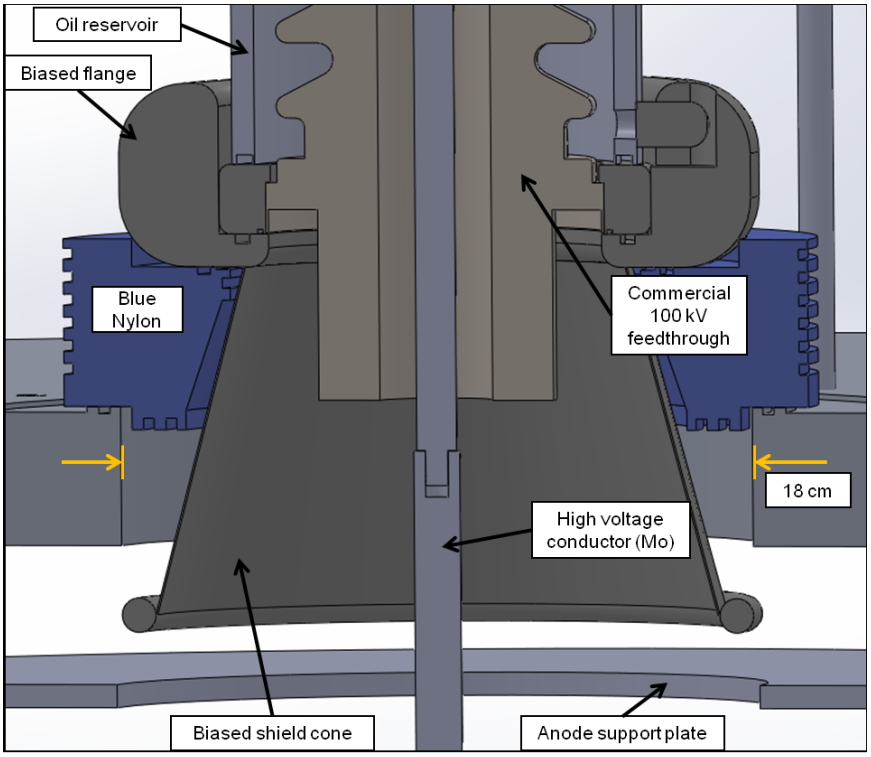

Figure 2-24: CAD model of a 2-stage biased feedthrough approach pursued at the University of Wisconsin-Madison [27].

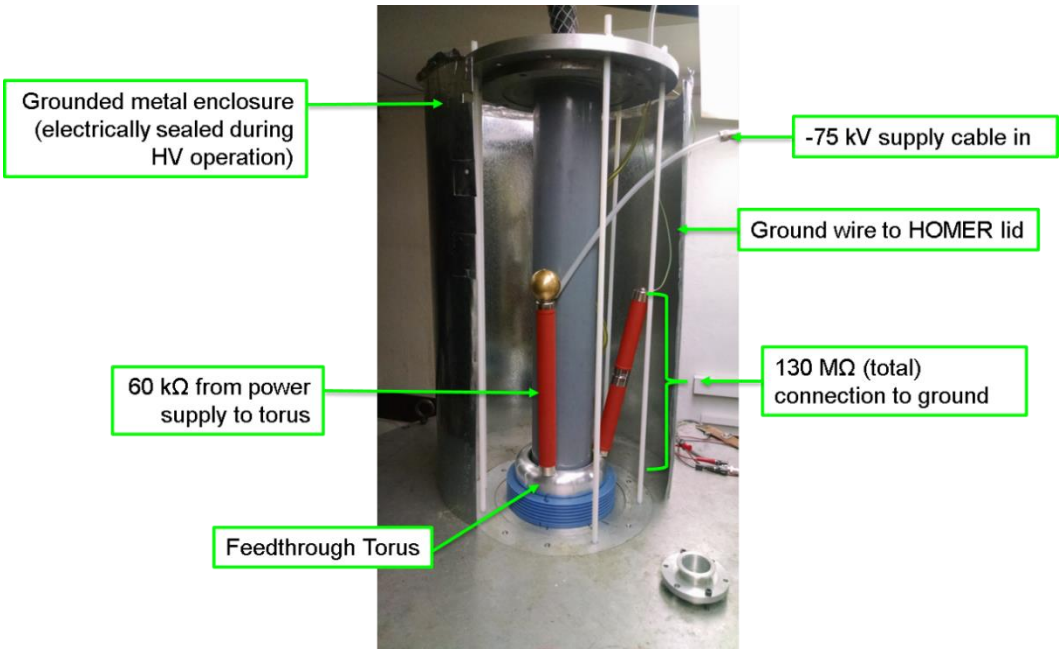

Figure 2-25: Photo of the biasing circuit used in the 2-stage feedthrough approach.

2.3 References

[1] W. C. Elmore, J. L. Tuck, and K. M. Watson, “On the Inertial-Electrostatic Confinement of a Plasma,” *Phys. Fluids*, vol. 2, no. 3, p. 239, 1959.

[2] R. L. Hirsch, “Inertial-electrostatic confinement of ionized fusion gases,” *J. Appl. Phys.*, vol. 38, no. 11, pp. 4522–4534, 1967.

[3] G. H. Miley and S. K. Murali, *Inertial Electrostatic Confinement (IEC) Fusion*. New York, NY: Springer New York, 2014.

[4] G. L. Kulcinski and J. F. Santarius, “Non-Electric Applications of the Inertial Electrostatic Confinement Fusion Concept,” *Fusion Sci. Technol.*, vol. 64, no. 2, pp. 365–372, Aug. 2013.

[5] J. H. Nadler, Y. B. Gu, and G. H. Miley, “Potential profile measurements using a collimated proton detector in spherical inertial-electrostatic plasma confinement,” *Rev. Sci. Instrum.*, vol. 63, no. 10, pp. 4810–4812, 1992.

[6] G. H. Miley, “A portable neutron/tunable X-ray source based on inertial electrostatic confinement,” *Nucl. Instruments Methods Phys. Res. Sect. A Accel. Spectrometers, Detect. Assoc. Equip.*, vol. 422, no. 1–3, pp. 16–20, Feb. 1999.

[7] G. H. Miley *et al.*, “IEC Thrusters for Space Probe Applications and Propulsion,” in *AIP Conference Proceedings*, 2009, pp. 164–174.

[8] T. J. McGuire and R. J. Sedwick, “Improved Confinement in Inertial Electrostatic Confinement for Fusion Space Power Reactors,” *J. Propuls. Power*, vol. 21, no. 4, pp. 697–706, 2005.

[9] A. M. Chap and R. J. Sedwick, “A Hybrid Particle-in-cell Simulation for a Multiple Grid Magnetic Core Inertial Electrostatic Confinement Device,” in *50th AIAA/ASME/SAE/ASEE Joint Propulsion Conference*, 2014.

[10] H. Ohgaki *et al.*, “Non-destructive inspection system for special nuclear material using inertial electrostatic confinement fusion neutrons and Laser Compton Scattering Gamma-rays,” in *2012 IEEE Conference on Technologies for Homeland Security (HST)*, 2012, vol. 64, no. 7, pp. 666–671.

[11] K. Noborio, Y. Yamamoto, Y. Ueno, and S. Konishi, “Confinement of ions in an inertial electrostatic confinement fusion (IECF) device and its influence on neutron production rate,” *Fusion Eng. Des.*, vol. 81, no. 8–14, pp. 1701–1705, Feb. 2006.

[12] Y. Takahashi *et al.*, “Development of landmine detection system based on the measurement of radiation from landmines,” *Appl. Radiat. Isot.*, vol. 68, no. 12, pp. 2327–2334, 2010.

[13] K. Tomiyasu, K. Yokoyama, M. Watanabe, and E. Hotta, “Particle-in-cell simulation of magnetic-assisted electrostatic confinement device,” *Fusion Eng. Des.*, vol. 85, no. 5, pp. 728–733, Aug. 2010.

[14] K. Yamauchi *et al.*, “Fundamental study of proton source based on inertial electrostatic confinement fusion for medical positron emission tomography,” in *The 31st IEEE International Conference on Plasma Science, 2004. ICOPS 2004. IEEE Conference Record - Abstracts.*, pp. 139–139.

[15] M. Ohnishi *et al.*, “Tritium burning in inertial electrostatic confinement fusion facility,” *Fusion Eng. Des.*, vol. 109–111, pp. 1709–1713, Nov. 2016.

[16] D. V. Gummersall, M. Carr, S. Cornish, and J. Kachan, “Scaling law of electron confinement in a zero beta polywell device,” *Phys. Plasmas*, vol. 20, no. 10, p. 102701, Oct. 2013.

[17] M. Carr and J. Khachan, “A biased probe analysis of potential well formation in an electron only, low beta Polywell magnetic field,” *Phys. Plasmas*, vol. 20, no. 5, p. 52504, May 2013.

[18] G. L. Kulcinski *et al.*, “Progress in the Understanding of Gridded Inertial Electrostatic Confinement Devices at the University of Wisconsin,” *Fusion Sci. Technol.*, vol. 68, no. 2, pp. 314–318, Sep. 2015.

[19] T. Thorson, “Ion Flow and Fusion Reactivity Characterization of a Spherically Convergent Ion Focus,” Ph.D. dissertation, University of Wisconsin-Madison, 1996.

[20] D. R. Boris, “Novel Diagnostic Approaches to Characterizing the Performance of the Wisconsin Intertial Electrostatic Confinement Plasma,” Ph.D. dissertation, University of Wisconsin-Madison, 2009.

[21] D. C. Donovan, “Spatial Profiling Using a Time of Flight Diagnostic and Applications of Deuterium-Deuterium Fusion in Spatial Profiling Using a Time of Flight Deuterium-Deuterium Fusion in Inertial,” Ph.D. dissertation, University of Wisconsin-Madison, 2011.

[22] A. McEvoy, “Time of Flight Diagnosis of Fusion Profiles in Spherical Inertial Electrostatic Confinement Devices,” Ph.D. dissertation, University of Wisconsin-Madison, 2014.

[23] D. R. Boris *et al.*, “Deuterium anions in inertial electrostatic confinement devices,” *Phys. Rev. E*, vol. 80, no. 3, p. 36408, Sep. 2009.

[24] E. C. Alderson, “Experimental and Theoretical Characterization of Negative Deuterium Ion Distributions in a Gridded Inertial-Electrostatic Confinement Device,” Ph.D. dissertation, University of Wisconsin-Madison, 2012.

[25] G. E. Becerra, “Neutral Particle Analysis in Inertial Electrostatic Confinement Fusion Devices,” Ph.D. dissertation, University of Wisconsin-Madison, 2014.

[26] M. K. Michalak, A. N. Fancher, G. L. Kulcinski, and J. F. Santarius, "Expanding Operational Space in Inertial Electrostatic Confinement D-D Neutron Generators," *Fusion Sci. Technol.*, vol. 72, no. 3, pp. 1–6, Jun. 2017.

[27] M. K. Michalak, "Increasing the High Voltage Capabilities and Exploring Parameter Space of an Inertial Electrostatic Confinement Fusion Neutron Source for the Detection of Chemical Explosives," Ph.D. dissertation, University of Wisconsin-Madison, 2017.

[28] S. K. Murali, "Diagnostic study of steady state advanced fuel fusion in an IEC device," PhD dissertation, University of Wisconsin-Madison, 2004.

[29] R. F. Radel, "Detection of Highly Enriched Uranium and Tungsten Surface Damage Studies Using a Pulsed Inertial Electrostatic Confinement Fusion Device," Ph.D. dissertation, University of Wisconsin-Madison, 2007.

[30] M. Abdel-Salam, *High-Voltage Engineering Theory and Practice*, 2nd Ed. CRC Press, 2000.

[31] D. C. Weisser, *Electrostatic Accelerators*. Berlin/Heidelberg: Springer-Verlag, 2005.

[32] A. Masiello, "Adaptation of the 1 MV bushing to the SINGAP concept for the ITER NB injector test bed," *Nucl. Fusion*, vol. 46, pp. 340–351, 2006.

[33] K. Masuda, Y. Yamagaki, T. Kajiwara, and J. Kipritidis, "Numerical Study of Ion Recirculation in an Improved Spherical Inertial Electrostatic Confinement Fusion Scheme by Use of a Multistage High Voltage Feedthrough," *Fusion Sci. Technol.*, vol. 60, no. 2, pp. 625–629, Aug. 2011.

[34] Y. Yamagaki, K. Masuda, G. Hashimoto, Y. Kamiya, and K. Nagasaki, "Experimental Results from an IEC Device Employing a 5-stage High Voltage Feedthrough," in *13th US-Japan Workshop on IECF*, 2011.

3. Inertial Electrostatic Confinement Theory and High Voltage Engineering Principles

This chapter describes the physics of inertial electrostatic confinement fusion and high voltage engineering concepts relevant to this work, and some key principles are elaborated here. As an IEC discharge is sustained, some collisions may result in measurable fusion reactions, but the majority of particle collision events occurring will result in charge exchange, ion impact ionization, or molecular dissociations while operating a deuterium discharge. Due to the complex nature of these collisional processes, a transport model is used to account for the spatial and energy distribution of ions entering the potential well from the source region and the subsequent ion generations formed due to collisional processes, and this model may be used to predict the fusion rate in a spherical IEC device. In addition, some of the engineering principles for high voltage used in the hardware design of the experimental setup for this work is discussed here.

3.1 Inertial Electrostatic Confinement Theory

The inertial electrostatic confinement device used in this work operates by accelerating ions radially inwards toward the device center by establishing an electric potential well using concentric, transparent spherical grids. A gridded cathode is biased to a negative voltage with respect to a grounded, transparent anode to form the potential, and the transparency allows confined ions to recirculate up and down the potential until their removal by a destructive collision or neutralization. A schematic of this operating principle is shown in Figure 3-1.

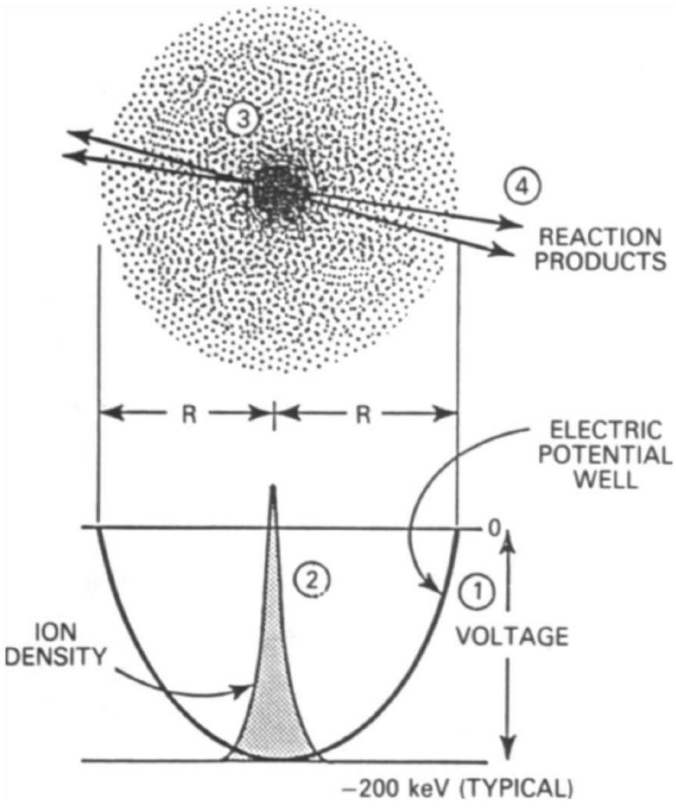

Figure 3-1: A deep negative electric potential well traps positive ions in spherically radial oscillations [1].

For the case of spherical, concentric electrodes, the vacuum potential, $\phi(r)$, is determined by solving Poisson's equation for this geometry as a function of radial position, r. Here r_c and r_a represent the cathode and anode radius, and the cathode voltage, V_c, is set with respect to a grounded anode:

$$\phi(r) = \begin{cases} -V_c & (r < r_c) \\ -\dfrac{r_c}{(r_a - r_c)}\left(\dfrac{r_a}{r} - 1\right)V_c & (r_c < r < r_a) \\ 0 & (r > r_a) \end{cases} \qquad 3\text{-}1$$

The radial electric field, $\boldsymbol{E}(r)$, is determined as $\boldsymbol{E}(r) = -\nabla\phi(r)$, and is maximized at the cathode radius:

$$\boldsymbol{E}(r) = \begin{cases} \frac{r_a r_c}{(r_a - r_c)r^2} V_c \hat{\boldsymbol{e}}_r & (r_c < r < r_a) \\ 0 & (r < r_c, r > r_a) \end{cases} \quad \text{3-2}$$

An ion with charge, q_i , can accelerate to a kinetic energy, E_i, by moving across this potential:

$$E_i = |q_i \Delta\phi| \quad \text{3-3}$$

The potential structure can be modified in regions of high charge densities, such as in the core of the device where space charge can build up due to the convergence of ion trajectories. The peaked density of ions can in principle, although very difficult in practice, lead to the formation of a virtual anode inside the cathode region, and a subsequent virtual cathode can form as electrons are convergent to the virtual anode. This nested set of potential wells, predicted by Farnsworth [2], would repeat; however, work by Gu and Miley [3] showed the number of potential structures is limited practically by ion energy spread and angular momentum in the experimental system. Additionally, perturbations to the potential structures exist in the experimental system due to the geometry of the gridded electrodes and high voltage stalk used to support and bias the grid, which can affect ion trajectories and lead to ion flow micro-channelling effects [4].

3.1.1 Fusion Reaction Regimes in an IEC device

For fusion reactions to occur, conditions require that two nuclei have sufficiently high kinetic energy to overcome enough of the Coulomb repulsion force to have a significant

probability to fuse. In the IEC device, the kinetic energy of the ion is gained by moving down the potential well, and reactants with kinetic energies on the order of tens to hundreds of keV can fuse, resulting in the formation of products with MeV level kinetic energies. These reactions are described in terms of their fusion cross sections, a measure of relative probability for the reaction to occur, which vary with the center-of-mass energy and among reaction types as seen in Figure 3-2. The IEC device has the capability of fusing a variety of fuels, and several reactions of interest to IEC studies are shown in Table 3-1. These fusion fuels sometimes are classified as first, second, or third generation fuels based on the input reaction energy needed to achieve significant rates of fusion. This work focuses exclusively on the D-D reaction for neutron production; however, some authors consider the use of aneutronic (low neutron production) reactions of the second and third generation fuels advantageous in advanced fusion energy concepts [5].

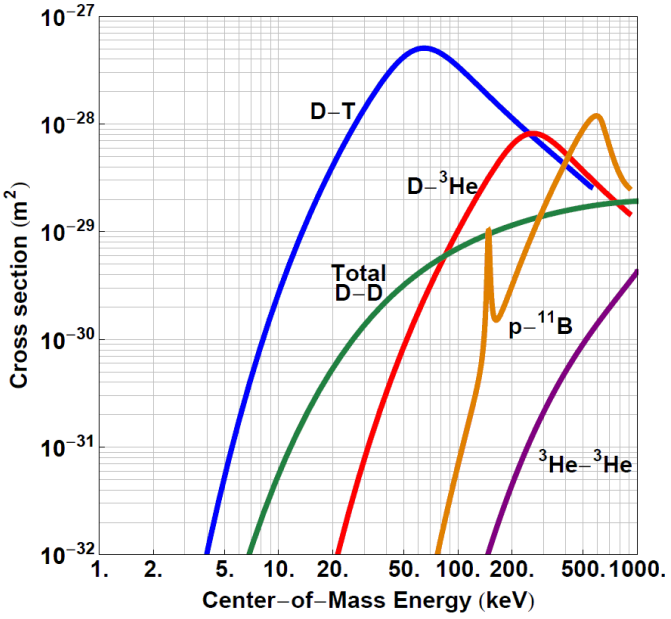

Figure 3-2: Reaction cross sections for fusion fuels of interest in an IEC device, data from [6]–[8].

Table 3-1: Fusion fuel reactions of interest to IEC devices.

First Generation	$D + T \rightarrow {}^{4}He\ (3.52\ MeV) + n\ (14.07\ MeV)$ $D + D \rightarrow \begin{cases} {}^{3}He\ (0.82\ MeV) + n\ (2.45\ MeV) \\ T\ (1.01\ MeV) + p\ (3.02\ MeV) \end{cases}$
Second Generation	$D + {}^{3}He \rightarrow {}^{4}He\ (3.67\ MeV) + p\ (14.68\ MeV)$
Third Generation	${}^{3}He + {}^{3}He \rightarrow \begin{cases} {}^{4}He + 2p\ (12.86\ MeV\ total) \\ {}^{5}Li^{(g.s.)} + p \rightarrow \underbrace{{}^{4}He + p}_{(3.79\ MeV\ total)} + p\ (9.07\ MeV) \end{cases}$ $p + {}^{11}B \rightarrow 3\ {}^{4}He\ (8.68\ MeV\ total)$

*Here (g.s) refers to ground state of the nucleus, and * represents an excited state of the nucleus*

The reaction rate per unit volume, R_{ij}, of the two interacting species will depend on the density of each species, $n_{i,j}$, the reaction cross section, σ_{ij}, and the relative velocity between the two species, v:

$$R_{ij} = n_i n_j \sigma_{ij} v \qquad 3\text{-}4$$

This general form can be applied to describe different reaction regimes common to the IEC operation. In a gridded IEC device, energetic (fast) ions or neutral particles can collide with other fast particles in beam-beam collisions, with background gas in beam-background collisions, or with embedded atoms in beam-embedded collisions, which can result in fusion reactions taking place.

3.1.1.1 Beam-beam reactions

Collisions between two fast particles, or beam-beam collisions, will have the greatest reaction energy available for fusion in the IEC device. Ions converging to the core region of the device can produce these beam-beam reactions; however, the likelihood of these collisions is rare due to a much larger presence of background gas density during typical operation, which these ions are more likely to interact with. These fast particles may be described in terms of their particle current, I, flowing through a surface within the device, and the reaction rate from equation 3-4 due to collisions of two fast populations would scale as $\sim I^2$. This fusion rate scaling has yet to be observed in an IEC device since operating in a beam-beam dominant reaction regime would require a significantly lower background gas density and is more technically challenging to achieve. A more detailed discussion of beam-beam reaction regimes in an IEC device is provided elsewhere [9].

3.1.1.2 Beam-background reactions

Collisions can occur as fast particles move through the background gas density present in the IEC chamber during operation, which can result in a beam-background fusion rate contribution. If the fast particles with a mass, m_i, are accelerated into a stationary background particle of mass, m_b, then the energy available to the fusion reaction in the center-of-mass frame, E_{fus}, can be transformed from the ion energy from the laboratory frame energy of the fast particle:

$$E_{fus} = \frac{m_b}{m_i + m_b} E_{Lab} \qquad 3\text{-}5$$

For ions accelerating down the potential well, the energy in the laboratory frame is gained by the charge moving across the potential, and in the case of like-mass particles colliding, the energy available to the fusion reaction is half of the laboratory frame energy.

A reaction rate per unit volume for beam-background collisions may be expressed in terms of the fusion cross section, σ_{fus}, ion density, n_i, background density, n_b:

$$R_{b-b} = n_b n_i \sigma_{fus}(E_{fus}) \sqrt{\frac{2E_{fus}}{m_i}} \qquad 3\text{-}6$$

This reaction rate per unit volume scales with a linear relationship to the current of fast particles, I, moving through the background gas:

$$R_{b-b} \sim n_b I \sigma_{fus}[E_{fus}] \qquad 3\text{-}7$$

3.1.1.3 Beam embedded reactions

Fast particles impacting solid surfaces loaded with a fuel density can fuse with trapped atoms embedded in the material as the fast particles slow down over the distance travelled. The energy attenuation of the incident particles as they travel through the substrate is represented by the stopping power $S(E_i) = -dE_i/dx$ of the material, and the embedded density of fusible atoms, n_{emb}, may vary as a function of depth in the solid. The incident particle flux, Φ_i, is represented by the total fast particle current divided by the substrate surface area. For the simple 1-dimensional case of fast particles traveling normally into the surface, the total embedded fusion rate may be calculated by integrating over the range of the particles to the final depth, x_f.

$$R_{emb} = \int_0^{x_f} n_{emb}(x)\Phi_i\sigma_{fus}\left[E_{fus}(x)\right]dx \qquad 3\text{-}8$$

The fuel density accumulated in the substrate can arise from the implantation of fast unconfined neutral or negative ion particles escaping radially from the spherical potential. These fast unconfined fuel particles are the result ions colliding with background gas species, and their origin in the system is discussed in the next section.

3.1.2 Atomic and Molecular Collisions in the IEC Device

The recirculating ion population trapped by the potential well of an IEC device becomes complex for deuterium fuel operation due to the presence of atomic and molecular collisions with the background gas which can lead to the formation of fast unconfined neutral or negative ions and a redistribution of ion energy by molecular dissociation. Ions born in the source region outside the potential well may be created by ionization of the background gas, and the experimental setup in this work uses electron impact ionization by a filament-assisted dc discharge to generate these source ions. These first generation ions born outside the potential well are unconfined to the system and can contribute to the subsequent generation of ions within the potential which become trapped. Table 3-2 shows possible deuterium ion formation processes due to electron impact ionization for these source ions. A previous study [10] of the HOMER IEC experiment has measured the source density ~10^7-10^8 cm^{-3} and electron temperature ~2 eV in this region, and distribution of deuterium ion species for typical operating parameters of 2 mTorr chamber pressure is estimated to be 71% D_3^+, 23% D_2^+, 6% D^+.

Table 3-2: Atomic and molecular processes in the formation of ions in the plasma source region external to anode grid [10].

Process	Interaction
1. Ionization of D_2	$e+D_2 \rightarrow D_2^+ + 2e$
2. Dissociation of D_2	$e+D_2 \rightarrow 2D+e$
3. Ionization of D	$e+D \rightarrow D^+ + 2e$
4. Dissociation of D_2^+	$e+D_2^+ \rightarrow D^+ + D + e$
5. Dissociative ionization of D_2	$e+D_2 \rightarrow D^+ + D + 2e$
6. Dissociative recombination of D_2^+	$e+D_2^+ \rightarrow 2D$
7. Interchange reactions producing D_3^+ ions	$D_2+D_2^+ \rightarrow D_3^+ + D$
8. Dissociative recombination of D_3^+ ions	$e+D_3^+ \rightarrow D_2+D$

Energy loss in the system due to charge exchange reactions occurs when a fast ion interacts with a slow neutral particle by electron exchange, resulting in a newly formed slow ion and a fast, unconfined neutral particle:

$$X^+(fast) + Y\ (slow) \rightarrow\ X(fast) + Y^+\ (slow) \qquad 3\text{-}9$$

If this process occurs part way down the electric potential well, this newly formed second generation ion will recirculate with a lesser maximum kinetic energy with respect to the first generation fast ion that created it. This neutralized first generation particle and its energy are lost to the chamber wall unless another particle interaction takes place. The second generation ion may recirculate through the system until it also interacts with another background species, collides with the cathode grid structure, or is lost to recombination, and subsequent generations of slow ions can

be generated. Table 3-3 gives a list of possible fast deuterium interactions with the neutral background gas population.

Table 3-3: Fast deuterium ion interactions with the background gas by atomic or molecular collisions resulting in ion destruction, stationary ion formation, or fast ion species formation [11].

Reaction	Process
$D^+ + D_2 \rightarrow$ various products	Total destruction of D^+
$D^+ + D_2 \rightarrow D^+ + \cdots$	Stationary D^+ production
$D^+ + D_2 \rightarrow D_2^+ + \cdots$	Stationary D_2^+ production
$D_2^+ + D_2 \rightarrow$ various products	Total destruction of D_2^+
$D_2^+ + D_2 \rightarrow D^+ + \cdots$	Fast D^+ production
$D_2^+ + D_2 \rightarrow D^+ + \cdots$	Stationary D^+ production
$D_2^+ + D_2 \rightarrow D_2 + D_2^+$	Stationary D_2^+ production
$D_3^+ + D_2 \rightarrow$ various products	Total destruction of D_3^+
$D_3^+ + D_2 \rightarrow D^+ + \cdots$	Fast D^+ production
$D_3^+ + D_2 \rightarrow D_2^+ + \cdots$	Fast D_2^+ production
$D_3^+ + D_2 \rightarrow D^+ + \cdots$	Stationary D^+ production
$D_3^+ + D_2 \rightarrow D_2^+ + \cdots$	Stationary D_2^+ production

Next generation ions may also be created by ion impact ionization reactions occurring when a fast incident ion strips an electron off a slow background molecule:

$$X^+(fast) + Y^0\,(slow) \rightarrow X^+(fast) + Y^+\,(slow) + e^- \qquad 3\text{-}10$$

The stripped electron is accelerated away from the negative potential and is lost to the system, while the parent and next generation ions recirculate in the potential well. These ion impact ionization reactions will have a higher likelihood of occurring at higher energies due to the reaction cross section, in contrast to the charge exchange reactions which can occur at a lower fraction of the cathode potential. Dominant reaction regions within the spherical potential of an IEC device for these types of interactions are highlighted in Figure 3-3.

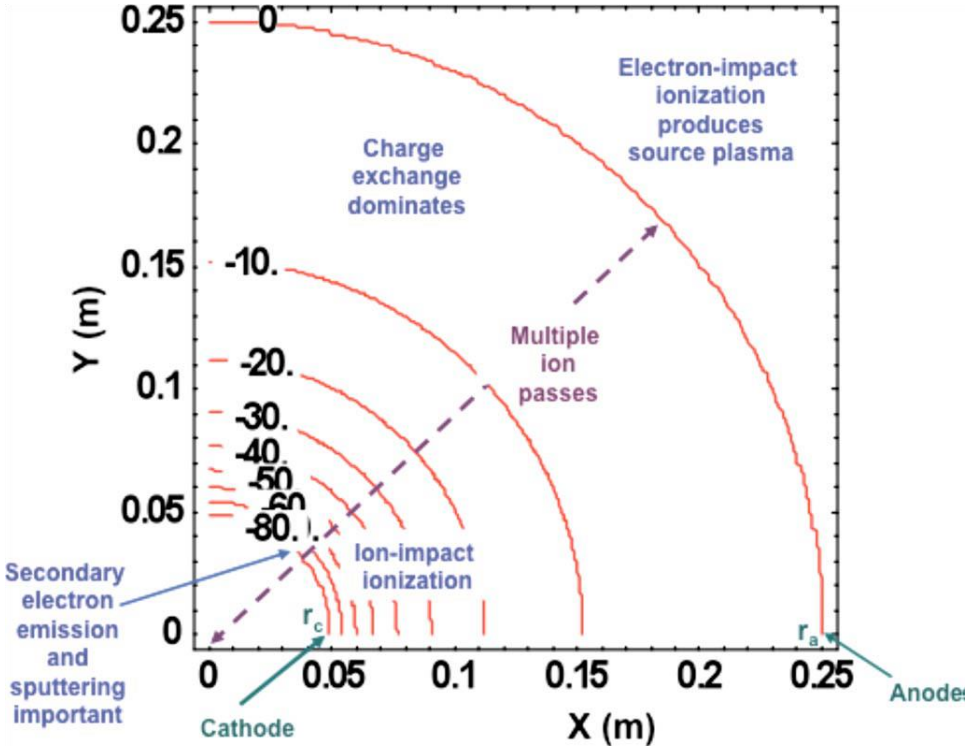

Figure 3-3: Regions of dominant atomic and molecular physics effects for typical spherical IEC operating with a cathode voltage of 80 kV [12].

Negative ion formation is also a possibility in a deuterium fueled IEC device, and their presence has been characterized experimentally in a past study for the HOMER IEC experiment

to contribute ~5% of the total ion current [13], [14]. Anion formation from electron attachment or molecular dissociation processes can occur, and several possible reaction channels are given in Table 3-4. Electrons may also be stripped from anions by reacting with background gas, either neutralizing the deuterium or resulting in the formation of a positive ion.

Table 3-4: Table of reactions involving the formation or destruction of negative ions [14].

Reaction	Process
$D + D_2 \rightarrow D^- + D^+ + D$	Dissociative
$D_2 + D_2 \rightarrow D^- + D^+ + D_2$	Dissociative
$D^+ + D_2 \rightarrow D^- + 2\mathrm{D}^+$	Dissociative
$D_2^+ + D_2 \rightarrow D^- + 2\mathrm{D}^+ + D$	Dissociative
$D_3^+ + D_2 \rightarrow D^- + 2\mathrm{D}^+ + 2\mathrm{D}$	Dissociative
$D_2 + e^- \rightarrow D_2^- \rightarrow D^- + D$	Electron attachment
$D^- + D_2 \rightarrow D + D_2 + e^-$	Electron stripping
$D^- + D_2 \rightarrow D^+ + D_2 + 2\,e^-$	Electron stripping

3.1.3 VICTER code

An integral transport approach describing the atomic and molecular physics present in an IEC device was created by Emmert and Santarius to model these processes and predict physical quantities of an operational device [11], [12]. This code, named Volterra Integral Code for Transport in Electrostatic Reactors (VICTER), models the flow of ions in the presence of a background gas density for a spherical electrode IEC device geometry and accounts for these charge exchange and molecular dissociation reactions described in the previous section. Several

assumptions are made in the 1-dimensional model. The model uses perfectly spherical concentric electrodes with a uniform transparency to the ion flow, in contrast to the grid wire structure and supporting stalk in the experimental setup, and the potential structure takes the form of the vacuum potential or the Child-Langmuir space-charge limited case. Background gas in the system is accounted for by a uniform constant density, and elastic collisions with the background gas are assumed negligible for the chamber pressures considered. Charge exchange and ion impact ionization processes are assumed to occur with negligible transfer of energy from the fast to slow species, which is valid at the energies of interest here. This results in fast neutrals and the formation of slow ions, and reionization of the fast neutral particles is considered negligible in the system.

First generation ion contributions to the initial ion source term, A, are born outside the anode radius in the external source region and are unconfined from the system, while the generation of subsequent ions within the anode region contribute to the total ion source term, S. These are confined until a process occurs that results in the removal of the ion from the system. For the case of deuterium, atomic, D^+, and molecular, D_2^+ and D_3^+, ions are included in the source terms, and the coupled set of equations shown in 3-11 and 3-12 is used to solve for the interactions. The kernel, K, relates the source term at one location to a new radial position, accounting for the various reaction cross sections and attenuating processes of the source ions as they are transported. The coupled set of equations take the form of a Volterra integral when summed over an infinite number of radial passes:

$$S^1 = A^1 + \int_r^b K^{11} S^1 dr' + \int_r^b K^{12} S^2 dr' \qquad 3\text{-}11$$

$$S^2 = A^2 + \int_r^b K^{21} S^1 dr' + \int_r^b K^{22} S^2 dr' \qquad 3\text{-}12$$

The model inputs the several IEC device parameters: the electrode and chamber wall radii, electrode transparencies, cathode voltage, ion current, background gas pressure, ion source species distribution. The result from solving for this source term is information about the energy spectrum of the ions and energetic neutral particles along with other macroscopic quantities of interest, and the neutron production rate of the system may be predicted for the device inputs.

3.2 High voltage and electrical breakdown of materials

Special consideration must be given to the application of high voltage to vacuum systems where gas discharge mechanisms may play a role in the breakdown of voltage standoff across a gap. Electrical breakdown in a high voltage vacuum system may occur across a physical gap, and often in plasma system, such as an IEC device, this breakdown is necessary to sustain a plasma discharge in a controlled manner. Uncontrolled breakdown of a high voltage gap can occur when a low resistance path forms in an unintended region of the hardware, resulting in the formation of a current path and often leaving a destructive path through the solid or along the surface of an insulator from high amounts of energy dissipation. Several features of a high voltage vacuum system that may lead to these types of uncontrolled breakdown have been identified by researchers and well-studied in the past [15]. Some of the high voltage breakdown mechanisms and principles of design relevant to the high voltage operation of an IEC device are presented here.

3.2.1 Breakdown mechanisms of high voltage electrodes and insulators

Breakdown of a high voltage system can originate by electron ejection from field emission sites under high electrical stress at the cathode surface, and Figure 3-4 shows possible

configurations involving multiple interfaces between vacuum, insulator, and a metallic electrode. Imperfections at the electrode surfaces may be the result of microparticles loosely adhered to the surface, sharp protruding features of a metallic surface, and weakened portions of an insulator where a pinhole has formed. These features result in a concentration of electric field, shown in Figure 3-5, which can eject electrons by field emission where the electric field is ~10-30x10^6 V/m. These ejected electrons are accelerated across the voltage gap, which can lead to the formation of streamers or avalanche discharges if the background pressure is high enough to sustain these types of discharges. If the gap conditions are low enough pressure, the ejected charged particles may impact the opposite electrode with high enough energies to vaporize some of the solid material, resulting in a return of ionized gas, which may create a breakdown path [15].

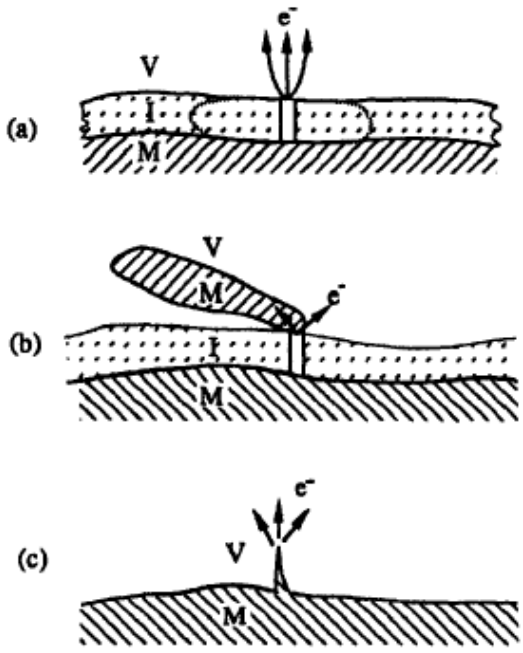

Figure 3-4: Electron emission processes at the cathode for different interface regimes: (a) Metal-Insulator-Vacuum, (b) Metal-Insulator-Metal, (c) Metallic-Microprotrusion [15]

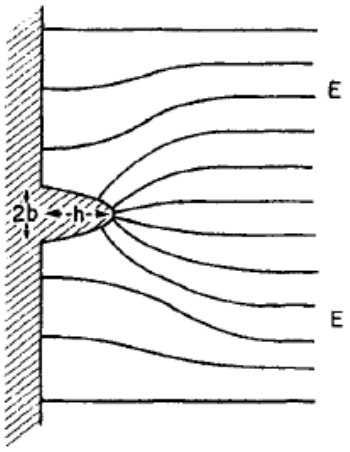

Figure 3-5: Illustration of electric field enhancement of the macroscopic field due to a microscopic protrusion [15]

When using insulators subject to high voltage environments, care must be given to ensure no voids or small gaps are introduced into the materials or at material interfaces. Discontinuity in the dielectric constant of the void or gap with the surrounding material causes field enhancement in this region which can lead to the formation of partial discharges and accelerated failure of the hardware [16]. The use of an insulator to bridge the gap between two high voltage electrodes under vacuum can also lead to a weak point in the design where electron emission from the cathode triple point may initiate a breakdown path as illustrated in Figure 3-6. Electrons emitting from the triple point junction may initiate an avalanche along the surface of an insulator which can cause outgassing from the surface, leading to the formation of a gas discharge along the surface ultimately leading to a full electrical breakdown in the desorbed gas, typically referred to as a flashover of the insulating material [16].

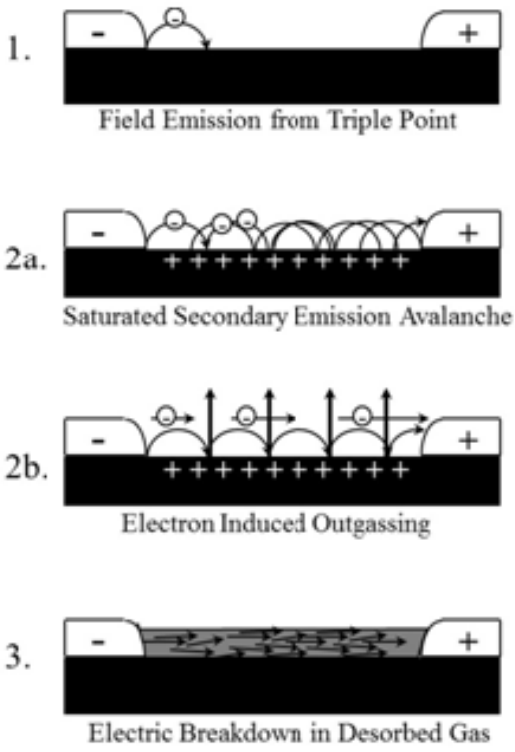

Figure 3-6: Illustration of a surface flashover initiated by the cathode triple junction [17].

Breakdown forming imperfections at the surface and emitting micro-features may be mitigated by proper surface preparation, cleaning procedures, and careful hardware assembly. To reduce the presence of surface flashover phenomena and breakdown, the following best practices are recommended in the design of high voltage insulating systems [18], [17]:

- Decrease macroscopic field by properly shaping electrodes and insulators to minimize the electrostatic field enhancement, recess insulators in electrodes, use metal inserts in insulators, and use external metal shields.
- Decrease microscopic field by minimizing voids at the triple point junction, use graded permittivities, bonded interfaces between insulators and conductors, apply pressure on soft insulators, and high voltage condition the insulator.

- Minimize quantities of adsorbed gases by selecting appropriate vacuum materials, practice clean assembly, perform a heated bakeout of the system, and high voltage condition the insulator.
- Minimize sites available for adsorption of gasses by applying surface treatments such as mechanical and electro-polishing at electrodes, minimize the surface damage during fabrication.
- Maximize binding energy of adsorbed gases by the use of surface treatments or quasi-metallizing.

3.2.2 High Voltage Conditioning

Reliable standoff of a high voltage system may be improved by the gradual increase of applied voltage, allowing for the careful quenching of current-emitting sites at the electrodes in a technique called high voltage conditioning, and several techniques have been identified to condition a system to higher voltages [15]. The process of current conditioning is performed by increasing the voltage in steps and allowing for small transient current producing events to occur until their rate of occurrence subsides, and Figure 3-7 illustrates a characteristic current-voltage trace of this process. Each spike in the trace represents an event where an emission site has been removed the destruction of the feature, typically by thermally blunting the sharp feature by bombardment with high energy charged particles. After some duration at voltage, the rate of current transients can be reduced significantly, and this process is repeated at increasing voltages no further progress is made. Additionally, high voltage conditioning by operating a helium glow

discharge is often used as an initial treatment of electrodes to remove field enhancing features, adsorbed gasses, and loose micro-particles on the surfaces of electrodes.

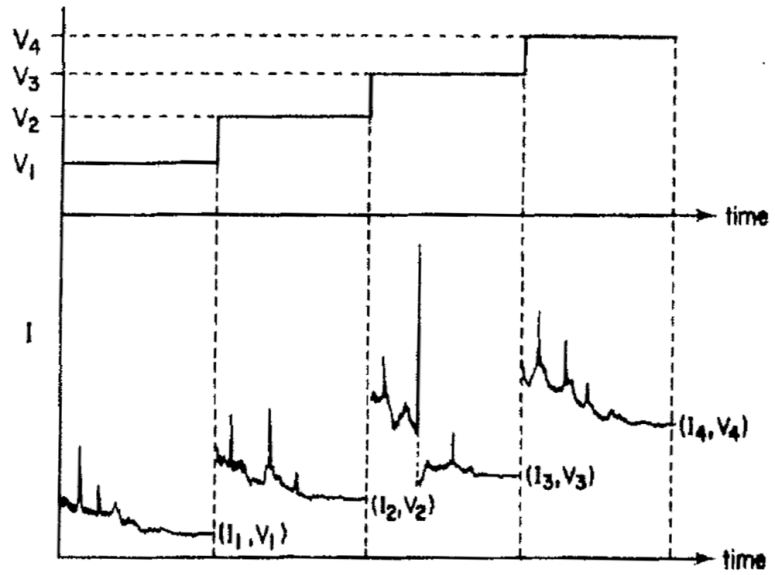

Figure 3-7: Schematic illustration of current conditioning technique applied to a high voltage system [15].

3.3 References

[1] R. W. Bussard, "Some Physics Considerations of Magnetic Inertial-Electrostatic Confinement: A New Concept for Spherical Converging-Flow Fusion," *Fusion Technol.*, vol. 19, no. 2, pp. 273–293, Mar. 1991.

[2] P. T. Farnsworth, "Method and Appartus for Producing Nuclear-Fusion Reactions," U.S. Patent 3 386 883, June, 1968.

[3] Y. Gu and G. H. Miley, "Experimental study of potential structure in a spherical IEC fusion device," *IEEE Trans. Plasma Sci.*, vol. 28, no. 1, pp. 331–346, 2000.

[4] S. K. Murali, G. L. Kulcinski, and J. F. Santarius, "Study of ion flow dynamics in an inertial electrostatic confinement device through sequential grid construction," *Phys. Plasmas*, vol. 15, no. 12, p. 122702, Dec. 2008.

[5] J.M. Dawson, "Advanced Fusion Reactors," in E. Teller, ed., *Fusion, Vol. 1 Magnetic Confinement, Part B* (Academic Press, New York, 1981), Chapter 16, p. 453.

[6] H.-S. Bosch and G. . Hale, "Improved formulas for fusion cross-sections and thermal reactivities," *Nucl. Fusion*, vol. 33, no. 12, pp. 1919–1919, Dec. 1993.

[7] W. Nevins and R. Swain, "The thermonuclear fusion rate coefficient for p- 11 B reactions," *Nucl. Fusion*, vol. 40, no. 4, pp. 865–872, Apr. 2000.

[8] M. R. Dwarakanath and H. Winkler, "3He(3He,2p)4He Total Cross-Section Measurements Below the Coulomb Barrier," *Phys. Rev. C*, vol. 4, no. 5, pp. 1532–1540, Nov. 1971.

[9] G. H. Miley and S. K. Murali, *Inertial Electrostatic Confinement (IEC) Fusion*. New York, NY: Springer New York, 2014.

[10] D. R. Boris and G. a. Emmert, "Composition of the source region plasma in inertial electrostatic confinement devices," *Phys. Plasmas*, vol. 15, no. 8, p. 83502, Aug. 2008.

[11] G. A. Emmert and J. F. Santarius, "Atomic and molecular effects on spherically convergent ion flow. II. Multiple molecular species," *Phys. Plasmas*, vol. 17, no. 1, p. 13503, Jan. 2010.

[12] G. A. Emmert and J. F. Santarius, "Atomic and molecular effects on spherically convergent ion flow. I. Single atomic species," *Phys. Plasmas*, vol. 17, no. 1, p. 13502, Jan. 2010.

[13] D. R. Boris *et al.*, "Deuterium anions in inertial electrostatic confinement devices," *Phys. Rev. E*, vol. 80, no. 3, p. 36408, Sep. 2009.

[14] E. C. Alderson, "Experimental and Theoretical Characterization of Negative Deuterium Ion Distributions in a Gridded Inertial-Electrostatic Confinement Device," Ph.D. dissertation, University of Wisconsin-Madison, 2012.

[15] R. Latham, *High Voltage Vacuum Insulation*. Author House, 2006.

[16] D. C. Faircloth, "Technological Aspects: High Voltage," in *CERN-2013-007*, 2014, p. 39.

[17] H. C. Miller, "Flashover of insulators in vacuum: the last twenty years," *IEEE Trans. Dielectr. Electr. Insul.*, vol. 22, no. 6, pp. 3641–3657, Dec. 2015.

[18] H. C. Miller, "Flashover of insulators in vacuum: review of the phenomena and techniques to improved holdoff voltage," *IEEE Trans. Electr. Insul.*, vol. 28, no. 4, pp. 512–527, 1993.

4. Experimental Design and Procedure

This chapter provides a description of the experimental hardware used for the results presented in this work, along with the design, construction, and configuration of hardware upgrades made by the author. A major goal of this work was the development of a vacuum high voltage feedthrough that would allow for 200 kV cathode operation biased negatively with respect to a grounded anode, a milestone that has previously not been met in any IEC device. To achieve this goal, the previous 175 kV feedthrough design was analyzed and examined for high voltage performance limiting features. A new feedthrough design was developed from these studies and tested successfully, allowing for cathode operations to 210 kV. In addition, the cathode grid design was also reconsidered for this work, and improvements were made to the design to increase high voltage stability during operation. A discussion of the hardware and design is presented here.

4.1 Description of the HOMER IEC experiment

Figure 4-1 shows a schematic of a gridded IEC experiment named HOMER at the University of Wisconsin-Madison, which highlights some common hardware components used for operation. In this device, a spherical gridded cathode is suspended within a vacuum chamber, and a highly negative voltage is applied with respect to a spherical, grounded anode to create electrostatic fields which accelerate ions toward the center of the device. Deuterium is the fuel typically used, but helium-3 fuels have also been studied in the past using this device. In HOMER, ions are typically generated by operating in a filament assisted electron impact ionization mode at chamber pressures less than 1.5 mTorr or in a glow discharge regime at chamber pressures greater than this level. Typical operating parameters of this device are: cathode voltages from 30 to 200

kV, anode grounded, metered cathode currents 30 to 100 mA, and background gas pressure from 0.3 to 1.5 mTorr. Measurements of fusion products are typically made by using an external neutron proportional counter setup or by using charged particle detectors mounted to the device ports. During higher power operations, a large fan directs a forced air flow around the chamber to convectively cool the chamber walls during operation and reduce chamber cool down time between operations.

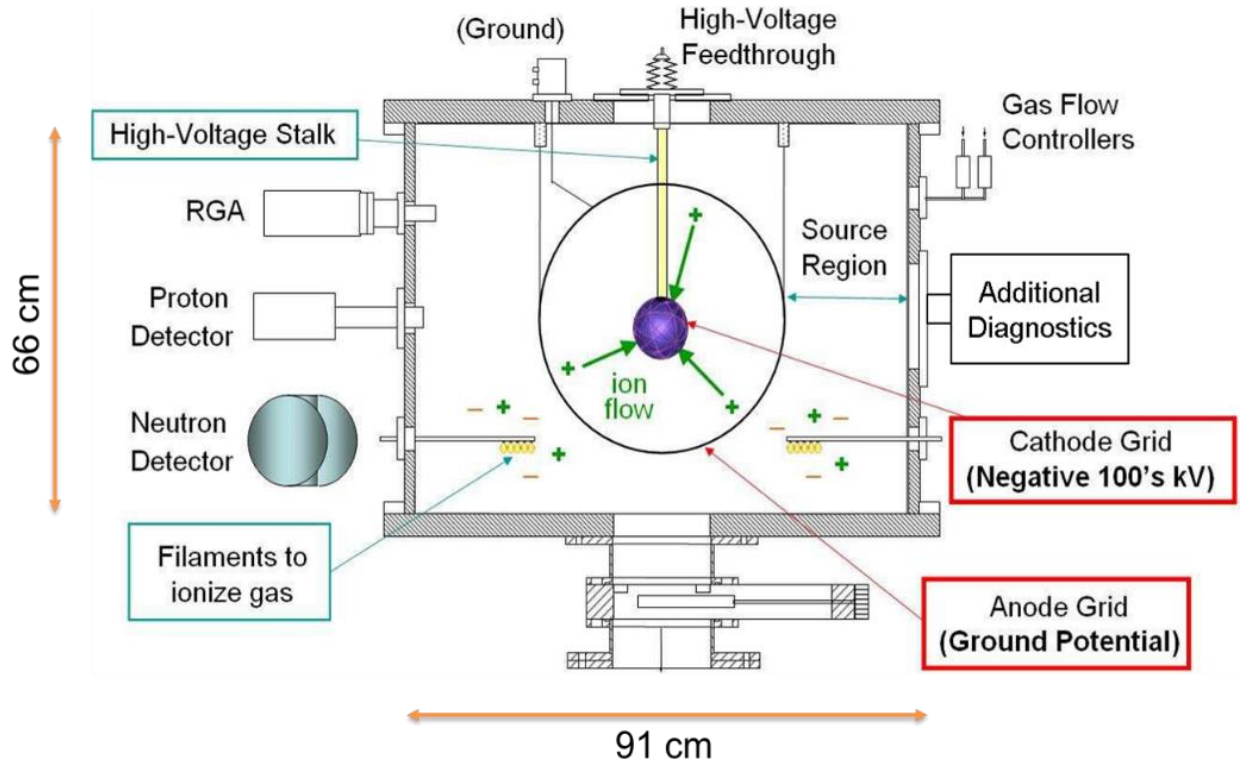

Figure 4-1: Schematic of the UW IEC HOMER device and several diagnostic capabilities.

4.1.1 Vacuum system and gas distribution

Vacuum is primarily achieved using a 550 L/s turbo molecular pump mounted on a vacuum Tee located at the bottom of the chamber which is backed by a 30 m^3/hr rough pump. The chamber features predominantly elastomer seals at the ports and achieves a base pressure of 4.3E-7 Torr as read from an ion gauge attached to the chamber. Deuterium flow is regulated using a mass flow controller and is routed to the chamber through a gas manifold capable of supplying gas feed to several other experiments in the laboratory. The mass flow controller is capable of supplying up to 50 standard cubic centimeter per minute N_2 equivalent gas flow to the HOMER chamber; the flow rate may be adjusted to set the deuterium chamber pressure during operation. The absolute pressure in the chamber is monitored during operations using a pressure transducer gauge which has a working range from 0.05 to 50 mTorr.

To monitor the fuel and vacuum quality during operations, a quadrupole type residual gas analyzer (RGA) is attached to a chamber port for sampling the chamber gas constituents. The RGA is used to monitor the background gas impurities (non-deuterium species) during IEC operation and is differentially pumped to maintain a lower pressure within the instrument while the chamber is held at the millitorr range during IEC operation. The RGA partial pressure spectrum represents a relative measure of the partial pressures of the gas species within the chamber rather than absolute partial pressures, and care must be given to account for the gas conductance and preferential pumping of different mass species if absolute measurements are to be determined. In this work, the RGA is used as a qualitative measure of chamber conditions and the presence of impurity gas by monitoring for the presence of higher mass gas species. Under clean chamber conditions, typical background gas impurities observed are due to water, nitrogen, oxygen, helium, and argon;

during operation, the impurity levels are observed to make up less than 1% chamber fill pressure with deuterium species dominating the neutral gas population.

4.1.2 High voltage distribution

High voltage is supplied to HOMER by a 300 kV negative polarity, 200 mA rated DC power supply built for the laboratory by Phoenix, LLC, a nuclear technology company headquartered in Monona, WI. The supply, shown in Figure 4-2, is controlled remotely by the operator outside of the radiation bunker and features an adjustable overload protection ranging in threshold from 0-200 mA that is capable of shutting the supply off in < 50 microseconds due to current excursions. This feature acts to protect the IEC device in the event of an arcing event in which a low resistance current path may form across a voltage gap that may lead to a destructive breakdown of hardware. To help protect against current surges due to arcing events, a 250 kΩ ballast resistor assembly is inserted between the high voltage power supply (HVPS) and the IEC device to limit the current draw from the supply. The resistor ballast circuit was originally designed for 200 kV operation; however, after testing the in-air performance, the voltage standoff is expected to be much higher, allowing operations beyond 200 kV. High voltage is routed from this supply to the ballast resistors and IEC feedthrough using 300 kV rated coaxial cable.

Figure 4-2: Negative Polarity 300 kV DC high voltage power supply control (left) and high voltage tank (right) used for this work; manufactured for the laboratory by Phoenix, LLC.

4.1.3 Data collection

Instrumentation data is collected and recorded using a LabVIEW program which receives inputs from a data acquisition device (DAQ). Signals containing information about the HVPS voltage and current, filament power supply settings, chamber pressure, chamber wall temperatures, deuterium flow rate, and neutron detector hardware are displayed in real time and are also sampled and written to an output text file for every two seconds of operation time. In addition to the data collected by LabVIEW, the experimental conditions are manually logged on a separate computer using a custom database log in which measured neutron counts from a multichannel analyzer are recorded for the nominal voltage, current, pressure, and chamber temperature set points along with any other information of interest.

4.1.3.1 Neutron detector hardware and calibration

Neutrons generated from the device are detected using a single ^{3}He proportional counter which is placed in a Long Counter moderating geometry [1] located in a corner of the lab at a chamber standoff distance of approximately 3.5 meters. The ^{3}He tube signal is shaped and amplified using the hardware described in Figure 4-3, and the raw signal processed using two different methods. First, the amplified detector signal is fed into a single channel analyzer which discriminates against low level noise and sends the output trigger pulses to a LabVIEW driven counting circuit which integrates the neutron counts over every 2 seconds and writes the output to the output text file along with the instrumentation data for the count. The LabVIEW program records the raw counts along with a calculation of the neutron production rate which compensates for the detector system deadtime and applies a calibration factor. The second process uses the amplified signal output fed to a multichannel analyzer configured to count only events which generate a signal proportional to the helium-3 neutron absorption reaction products within the energy deposition range inside the detector tube.

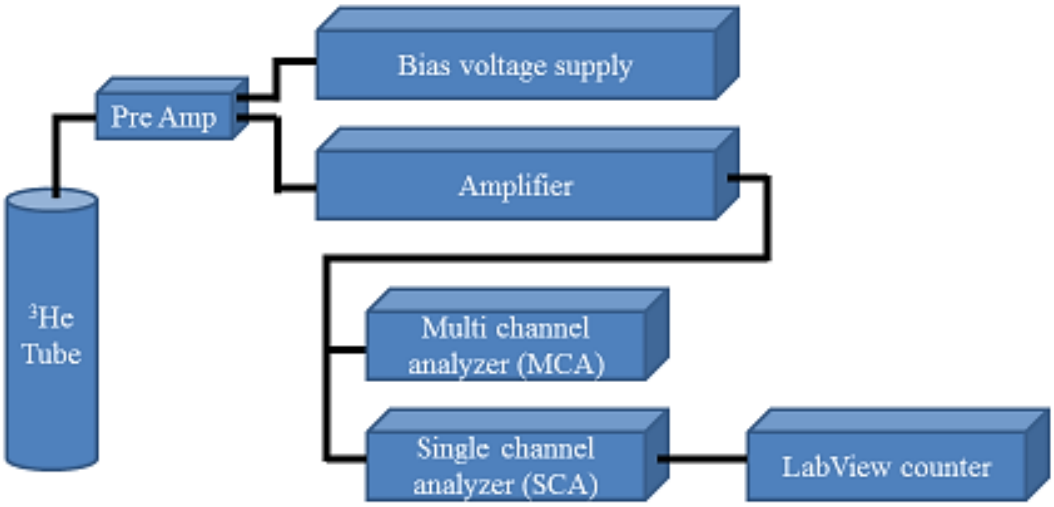

Figure 4-3: Neutron detector counting hardware configuration.

The detector response is calibrated using a PuBe calibration source which is placed in the center of the HOMER device. Counts are then recorded using both the SCA/LabVIEW and the MCA/Database log systems. The calibration source is measured until at least 10,000 counts have been reached using both systems, thereby reducing the counting error to 1% uncertainty. The count rate measured is then corrected for the system deadtime on the LabVIEW computer and a count rate is obtained from the integrated counts over the region of interest in the MCA divided by the MCA counter live time. These measured count rates are then compared to the original source strength to give a calibration factor using equation 4-1.

$$Calibration\ Factor = \frac{Source\ Strength}{Measured\ Count\ Rate} \qquad 4\text{-}1$$

Uncertainty in this measurement is dominated by the degree to which the calibration source is known. The plutonium-beryllium (PuBe) source is reported to have a strength of 2.2E6 neutrons/s with an uncertainty of ± 0.05E6 neutrons/s (Date: 10/13/2017); it should be noted this uncertainty in the calibration source strength dominates the uncertainty in the counting system for the determination of the calibration factor. The measured neutron calibration factors used in this work are reported in Table 4-1.

Table 4-1: ^{3}He neutron detector calibration factors for this work.

Counter	Calibration Factor
SCA	39780 ± 920
MCA	39320 ± 940

4.1.3.2 HOMER operational procedure

To achieve peak high voltage performance, HOMER is subjected to high voltage conditioning after bringing the chamber up to air and whenever any new electrical insulator or electrode is introduced, replaced, or modified. For a gridded IEC device, high voltage conditioning may be achieved by operating under plasma conditions where ion bombardment of the cathode may help to clean surface impurities and remove micro-features of the electrode surfaces which may cause field enhancement and premature breakdown of the voltage gap. Operating at higher power inputs will rapidly heat the chamber walls and electrodes to encourage evolution of gasses from the structures and subsequent removal by pumping. Over time, the effect of conditioning is the minimization of outgassing impurities during operations and the increased high voltage standoff performance of the system. There is a limit to the upward progress of high voltage standoff improvement due to conditioning processes, after which standoff no longer can be improved by surface modification at the microscopic level [2].

Some imposed limits of the system are in place due to the limitations of the hardware used. The external chamber wall temperature is not allowed to exceed 80 °C due to the use of a nylon insulator standoff and elastomer seals. The maximum steady-state current draw from the system is limited to 100 mA by the resistive power dissipation in the ballast resistor assembly, which has a design rating of 2500 W. An upper chamber pressure during operation is determined by the high voltage breakdown of background gas into a glow discharge regime, which is noted to be in the range of 1.2 to 2.0 mTorr for the hardware configuration presented in this work.

The measurements taken for this work were typically done using two different data collection procedures. The first is that during each operation data is collected from LabVIEW, the IEC logbook, the RGA, and a document containing computer screen captures of the operating/LabVIEW computer and operator notes, which provides a quick snapshot reference to the operating conditions within a run. At the beginning of each operation, a set of fixed device parameters are operated for system monitoring. These fixed conditions represent operating parameters which fix the cathode voltage (30, 80, 120, 160 kV), cathode current (30 mA), and chamber pressure (1.0 mTorr) while measuring the neutron production rate. A comparison may then be made run-to-run and day-to-day to check for abnormalities and look for any long term trends of the system neutron production rate performance. This data is collected for all runs including conditioning and data collection runs.

The second is a more specific data collection process that focuses on isolating specific parameters and conditions. At the start of the run day, a special program called a “priming run” is commenced to operate the chamber at the fixed conditions and to heat the chamber walls, which encourages outgassing and removal of impurities after an extended period of no operations (typically after not being operated overnight). A data collection day is planned to measure the

neutron production rate for the variation of one of the following: cathode voltage, cathode current, or chamber pressure while holding the other two constant. The set points of the parameter to be varied for the day are randomized in the order that they are to be measured. Each data run for the day consists of the fiducial startup sequence followed by a brief shutdown of the system followed by the acquisition of data at the selected set point(s) to be measured. This process typically takes no longer than 15 minutes and the experiment is then left to cool down and pump out over the next 1.5 hours to reestablish baseline conditions of the chamber wall temperature and base pressure.

4.2 High voltage feedthrough design

A major focus of this work has been the advancement of the high voltage feedthrough design, and this allowed for previously unachieved operational voltages up to 210 kV cathode voltage. In the previous work, the author collaborated with Michalak on the development of a 2-stage feedthrough [3]. This previous feedthrough utilized a separate -75 kV power supply to bias the intermediate voltage stage to control the voltage gaps and reduce the electric fields, and this design was successfully operated up to its anticipated cathode voltage design limit of 175 kV. The feedthrough was then disassembled and studied, looking for any regions of degradation and component wear due to electrical stresses and charged particle bombardment. Significant degradation of the blue nylon insulator near the grounded chamber lid was found where partial discharges had begun to bore holes through the bulk material in regions of high electrical stress. Additionally, electrical degradation was seen on the surfaces of the shield cone and grounded chamber lid and anode support plate where the electric field of the voltage gap was highest and evidence of arcing had occurred.

The design of this new feedthrough applied field reducing geometries to eliminate some critical regions of enhanced field stress. It also eliminated the need for a second, high voltage power supply to actively control the intermediate voltage gap by using a passive resistive voltage divider design. This new design and some of the hardware features are pictured in Figure 4-4. A commercially available 100 kV vacuum feedthrough is integrated into a 2-stage voltage standoff approach and was modified by replacing the original conductor with a highly polished 12.7 mm diameter stainless steel conductor to reduce fields at the conductor and add rigidity to the stalk. The vacuum flange of the feedthrough rests on a toroidal voltage platform which also supports the electrostatic shield horn. The 100 kV feedthrough vacuum flange, torus platform, and shield horn are all electrically connected and biased to an intermediate voltage level determined by the voltage divider. The HVPS cable is plugged into the first stage voltage platform which connects the center conductor, cathode grid, and the first stage resistors. The first stage resistors connect to the second stage voltage platform via the torus, and a second set of resistors connect the second stage to the chamber ground. A small, 1 kΩ resistor is placed between the second stage resistors and the ground to monitor current draw of the voltage divider during operations. The resistor divider circuit and insulating standoffs are immersed in dielectric oil to improve voltage standoff and eliminate atmospheric corona. The body of the oil tank is constructed out of PVC and is coated externally with a conformal conductive spray coating and wrapped with sheet steel and conductive tape cover which are electrically connected to the grounded chamber.

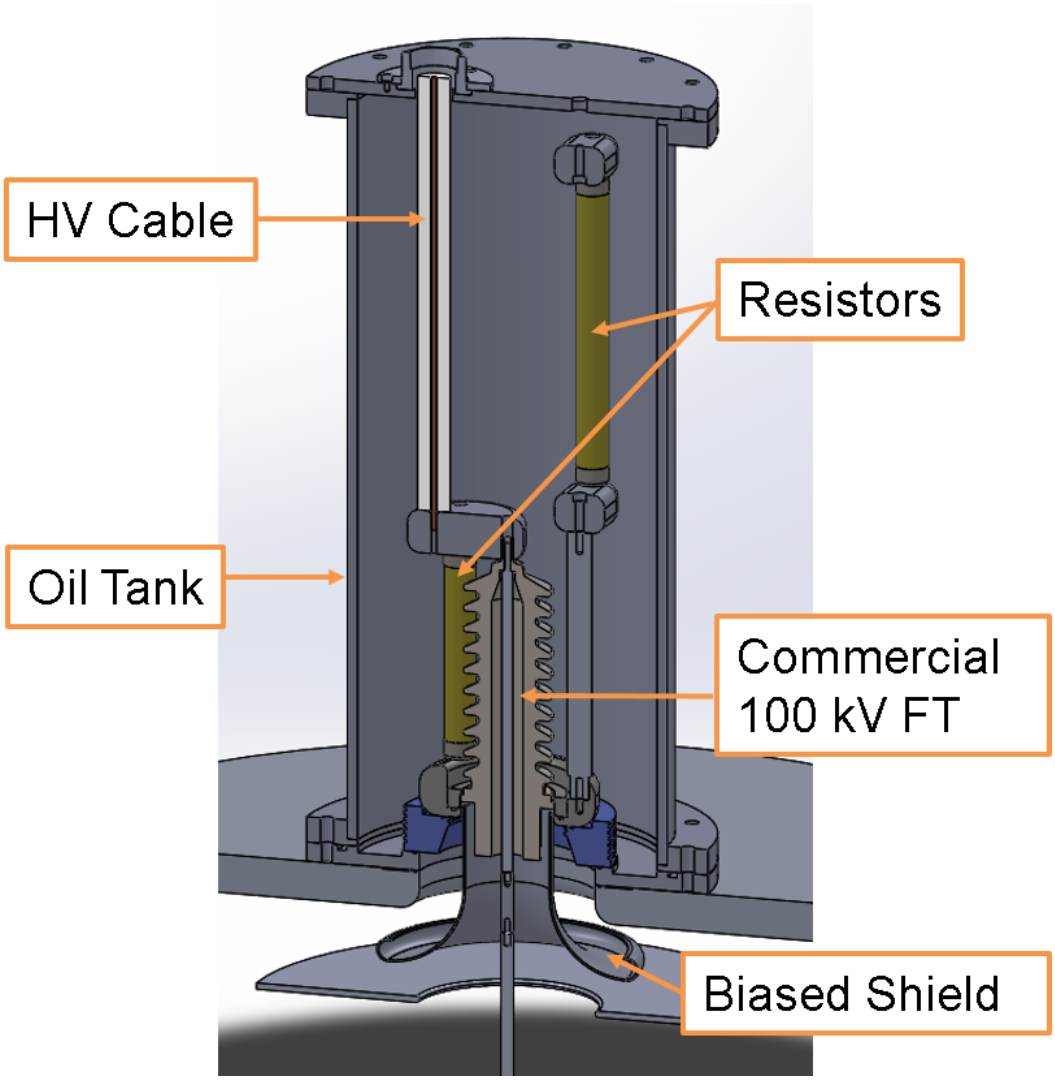

Figure 4-4: A cutaway CAD model of the 2-stage resistively divided feedthrough design that was constructed for this work.

4.2.1 Circuit model of the feedthrough design

A simple DC circuit model was created to evaluate the current draw of the shield electrode due to the plasma interaction under operating conditions. Ions collected on the shield along with secondary electrons emitted contribute to the power supply current. The performance of the 2-

stage biased feedthrough was analyzed in order to inform the design needs of the resistively divided 2-stage feedthrough.

4.2.1.1 Circuit analysis of the previous 2-stage biased feedthrough design

To estimate the current contribution to the system at the shield electrode for the resistive voltage divider design, a circuit model of the previous 2-stage biased feedthrough was evaluated. The circuit for this design is show in Figure 4-5, and a more detailed derivation of the following equations using Kirchhoff's laws is given in the appendix. In this model, the plasma resistivity is represented by a total resistance across the plasma gaps at the cathode, R_{p-c}, and at the shield R_{p-s}; the plasma resistance is treated as unknown in this analysis. The high voltage power supply voltage, V_{HVPS}, sets the cathode voltage, $V_{cathode}$, and the feedthrough power supply, V_{FTPS}, sets the voltage at the shield electrode, V_{shield}.

By examining the feedthrough power supply circuit on the right side of Figure 4-5, the contribution of current collected at the shield through the plasma, I_{shield}, may be determined by setting the feedthrough power supply voltage, V_{FTPS}, and observing the current draw from the feedthrough power supply, I_{FTPS}.

$$I_{shield} = \left(\frac{R_1 + R_2}{R_1}\right) I_{FTPS} - \left(\frac{V_{FTPS}}{R_2}\right) \qquad 4\text{-}2$$

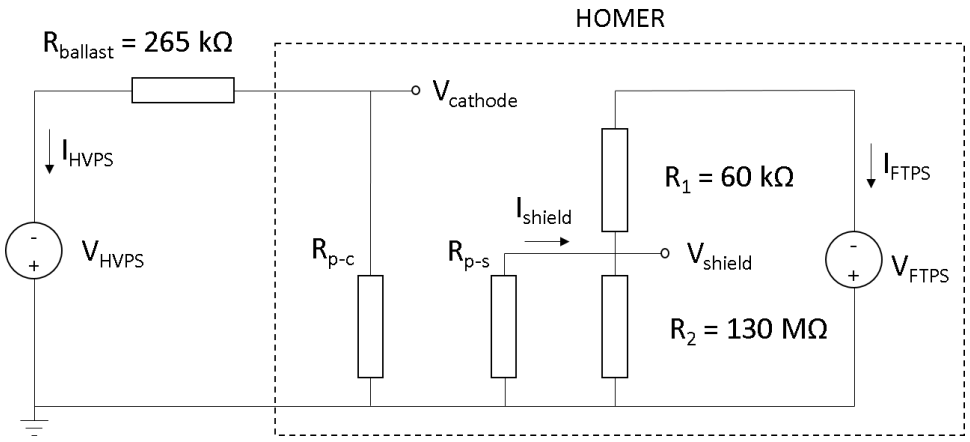

Figure 4-5: Circuit model of the previous 2-staged biased feedthrough design that used a second, external power supply to apply voltage to the shield electrode.

The current collected on the shield plate during operation was compared to the cathode current and cathode voltage while holding the feedthrough power supply at -60 kV. Figure 4-6 shows the shield current has a strong dependence on the chamber pressure and cathode current and a weak dependence on cathode voltage. For operations at 1 mTorr chamber pressure, the shield current varied from 0.05-0.2 mA for cathode currents ranging 30-100 mA, and the shield current varied from 0.3 to ~0.9 mA over this same range while operating at 0.3 mTorr chamber pressure.

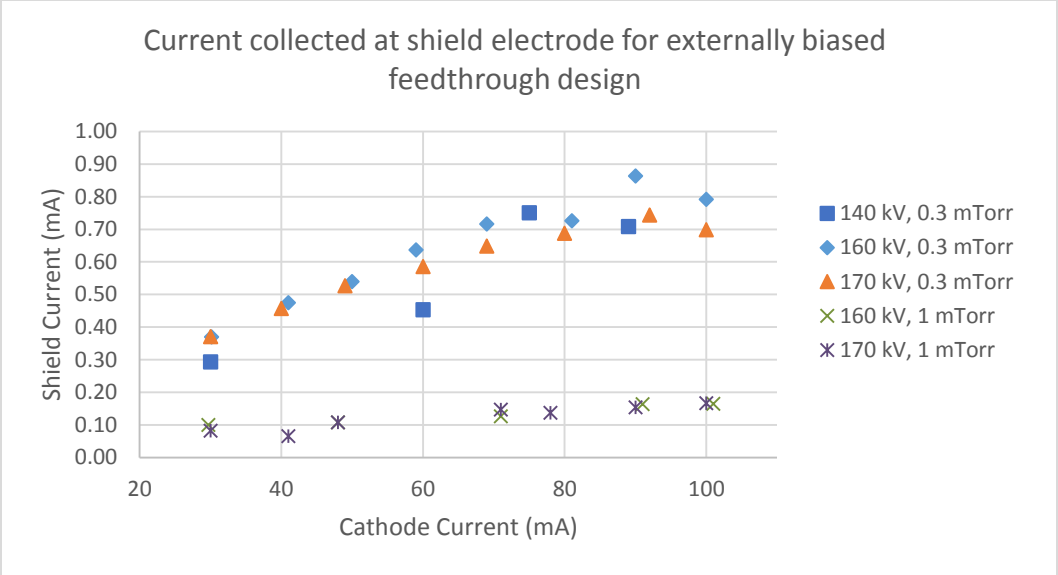

Figure 4-6: Current collected at the shield electrode is weakly dependent on cathode voltage and strongly dependent on chamber pressure and cathode current.

4.2.1.2 Circuit model for 2-stage resistive feedthrough circuit

Since the new 2-stage resistive voltage divider design does not rely on a regulated voltage supply to maintain a shield set point voltage, the estimated current collection was taken from the previous design and used to inform the selection of resistance values and power ratings for the divider resistors. A simple DC circuit was modeled for the resistive voltage divider design is shown in Figure 4-7. Here, a voltage platform and electrostatic shield are placed between two resistors which bias the shield at an intermediate potential with respect to the center conducting stalk and the grounded chamber. The plasma impedance at the cathode and the shield are represented by the resistive component of the plasma for the purposes of this DC circuit analysis.

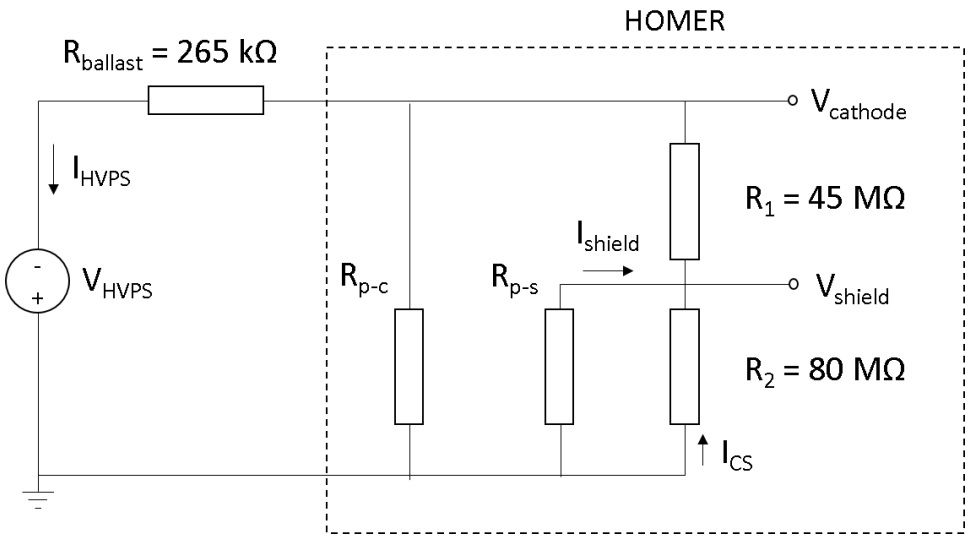

Figure 4-7: Circuit model of the 2-stage resistive feedthrough design.

To determine the current at the cathode grid and shield electrodes, this system may be solved in terms of the measured voltage and current at the high voltage power supply along with a measurement of the current draw, I_{CS}, through the resistive feedthrough via a 1 kΩ current sense resistor placed between R_2 and ground. A derivation of the following equations is provided in the appendix. Solving this system for the shield current gives:

$$I_{shield} = \frac{[V_{HVPS} - R_{Ballast} I_{HVPS} - (R_1 + R_2) I_{CS}]}{R_1} \quad \text{4-3}$$

And the current collected at the cathode is represented by:

$$I_{cathode} = I_{HVPS} - I_{shield} - I_{CS} \quad \text{4-4}$$

Under no plasma load, the system reduces simply to the current drawn, I_{drain}, from the high voltage power supply across the series resistance from the barrel and the two resistor stages.

$$I_{drain} = \frac{V_{HVPS}}{R_B + R_1 + R_2} \quad 4\text{-}5$$

The drain current is related to the current draw across the second stage current sense resistor by:

$$I_{CS} = I_{Drain} - I_{Cathode}\left(\frac{R_B}{R_B + R_1 + R_2}\right) - I_{Shield}\left(\frac{R_B + R_1}{R_B + R_1 + R_2}\right) \quad 4\text{-}6$$

The selected resistance of the voltage divider stages must divide the voltage drop across the feedthrough appropriately at no greater than 100 kV, maintain voltage stability at the second stage in the presence of a current draw from the shield electrode, and dissipate an acceptable amount of power in the resistors. The power dissipation, P, across each stage is:

$$P_1 = (I_{Shield} + I_{CS})^2 R_1 \quad 4\text{-}7$$

$$P_2 = I_{CS}^2 R_2 \quad 4\text{-}8$$

To maintain voltage stability of the shield, the current drawn by the voltage divider circuit was chosen to be 5-10 times greater than the expected current draw from the shield under plasma load to reduce the amount of skewing in the voltage divider ratio during plasma operations. For 1 mTorr operation, the shield current collected on the previous feedthrough design was near 0.2 mA for a cathode current operation at 100 mA and thus the voltage divider drain current should range

1-2 mA to provide adequate stability in the shield voltage due to perturbations. A total voltage divider resistance was chosen to be 125 MΩ to provide a drain current of 1.6 mA through the feedthrough resistor divider while setting the high voltage power supply to 200 kV under no plasma load. During plasma operation, the shield will draw a current from the plasma and contribute to the flow across the first stage resistors thus producing a larger voltage drop across the first stage and skewing the voltage divider ratio.

To account for this shift in voltage, the resistance values were divided asymmetrically, setting 45 MΩ for the first stage and 80 MΩ for the second stage. For cathode operation at 200 kV, 100 mA, this would give the first stage an estimated current of 1.73 mA, voltage drop of 77.8 kV, and power dissipation of 135 Watts. For the second stage, the estimated current would be 1.53 mA, voltage drop of 122.2 kV, and power dissipation of 187 Watts. To accommodate the voltage drops and resistive power dissipation during plasma operations, EBG MTX 969.105 and 969.71 series resistors were selected which are rated, respectively, for in-air operation at 96 kV and 64 kV standoff, 105 Watts and 71 Watts power dissipation, and both feature non-inductive windings. Each stage is comprised of two of resistors in parallel which are immersed in dielectric oil to increase voltage standoff and heat removal capabilities.

4.2.2 Electrostatic model of the feedthrough designs

An electrostatic model of the previous 2-stage biased feedthrough design was created to examine the electrical stress created by the electrode geometries at high voltages. The electrostatic models presented here were generated using a finite element approach which solves Poisson's equation for electrostatic potentials over a geometry for a given set of boundary conditions. A 1:1

scale CAD model was drawn using SOLIDWORKS which was then imported into Finite Elements Method Magnetics (FEMM) version 4.2 for analysis [4].

4.2.2.1 Electrostatic model of the 2-stage biased feedthrough design

Figure 4-8 shows a 2D axisymmetric model of the electrostatic fields of the previous 2-stage biased feedthrough design, which simulates -200 kV applied to the center conducting stalk and -100 kV applied to the high voltage platform and shield cone. In this model, the convoluted alumina feedthrough is surrounded by a column of dielectric oil supported by a PVC tube; outside this tube is an air gap and a grounded metal surround which is not shown in the CAD drawing. The model shows regions of strong electric fields at the rounded hoop of the shield horn and at the corners of the chamber lid and anode support plate where the fields are greater than 10^7 V/m at the electrode surfaces. In this simulation, 0.25 mm radii were added to 90° corners to reduce some artificial field enhancement positions not represented in the physical model. Additionally, field enhancement is also seen to occur at small gaps between dielectric interfaces near electrodes due to the discontinuity of the material permittivity. A list of the material permittivities used in the electrostatic models is shown in Table 4-2.

Table 4-2: Relative permittivity of dielectrics used in the electrostatic models generated using FEMM software [4].

Material	Relative Permittivity (ε)
Vacuum	1
Air	1
Alumina	9.3
Blue Nylon	3.6
PVC	3.4
Dielectric Oil	2.2

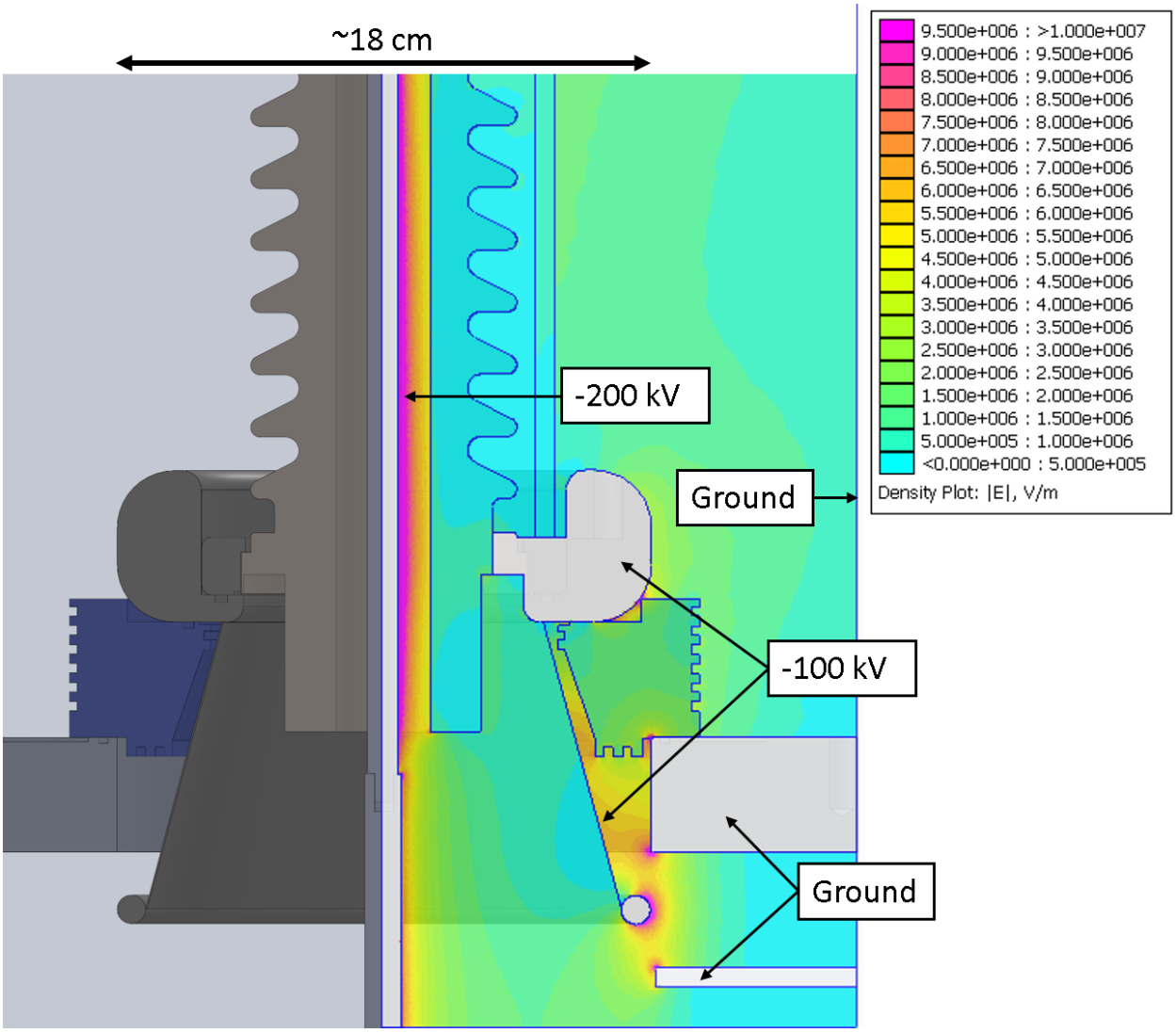

Figure 4-8: CAD model of the 2-stage biased feedthrough design overlaid with an axisymmetric electrostatic model showing electric field distribution created using FEMM software [4].

4.2.2.2 Electrostatic model of the new 2-stage resistive feedthrough design

A design goal of the new 2-stage resistive feedthrough was to modify the shield geometry to reduce the electric fields to below $5x10^6$ V/m in the feedthrough regions between the conducting stalk and shield, between the shield and the grounded chamber lid, and between the shield and anode support plate. Figure 4-9 shows the CAD with a 2D axisymmetric FEMM electrostatic calculation of the 2-stage resistive feedthrough design. To accomplish these field reductions, a flared horn geometry was chosen for the shield which smooths out many of the field enhancing features seen in the previous design. To reduce the field enhancement caused by the squared corner of the chamber lid, a 19 mm radius has been added to the lower edge. It should be noted that the grids shown in Figure 4-9 are modeled as solid surfaces of revolution rather than the true grid wire structure represented in the CAD drawing and the physical hardware. Additionally, the voltage divider resistors and hardware have been left out of this electrostatic model. In this design, an oil column surrounds the 100 kV ceramic feedthrough, blue nylon standoff, intermediate voltage platform, and resistors on the non-vacuum side, and the oil column is supported by a PVC enclosure which is grounded on the outside.

The simulation result shows the electric fields at the shield and lid are greatly reduced in comparison to the previous design (Figure 4-8) with a peak field reduction of greater than 2 times the previous design for the shield and chamber surfaces. The curvature of the shield to lid gap also creates a more uniform field distribution, and the vacuum gap lengths have been increased to reduce field enhancement.

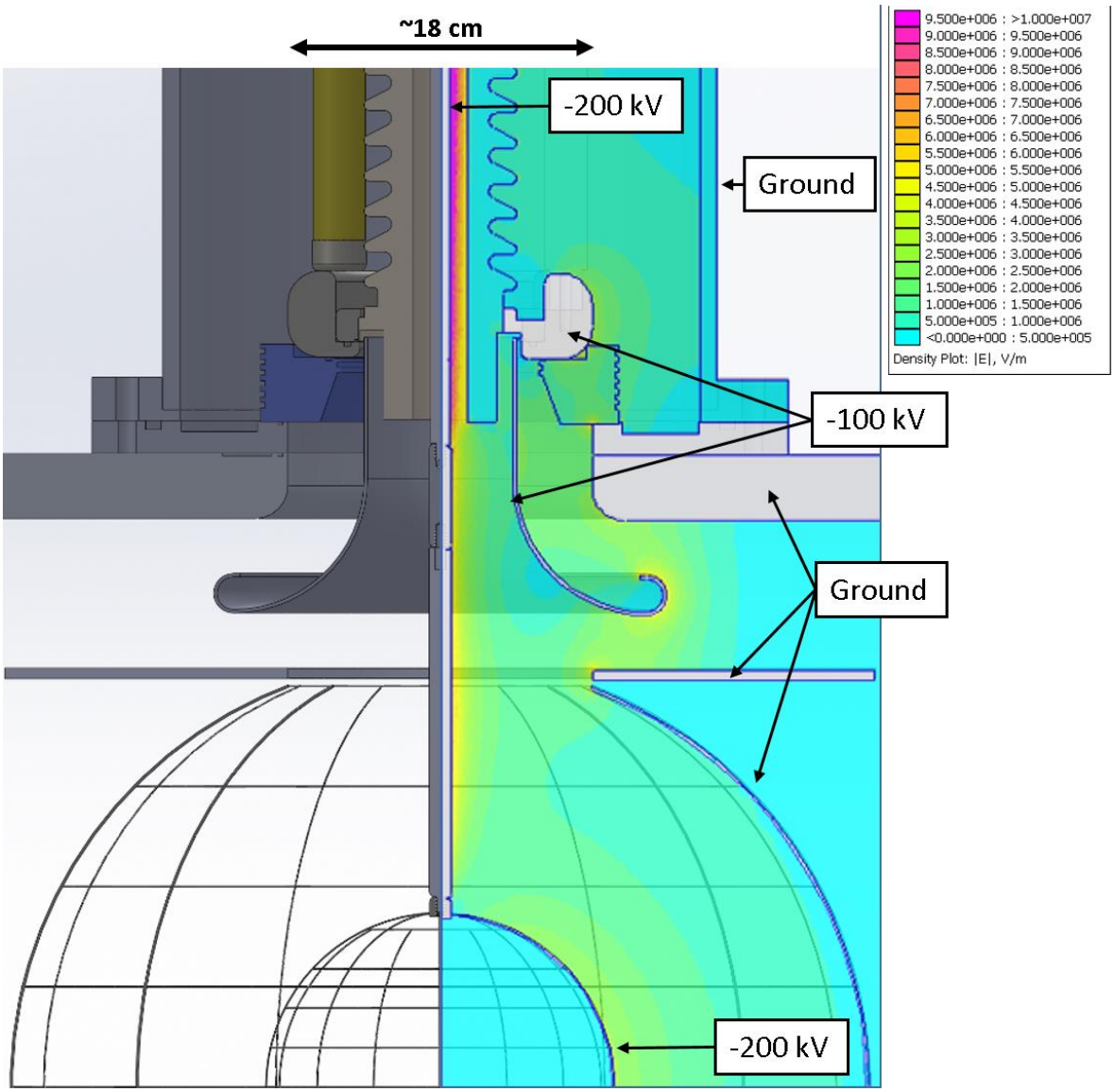

Figure 4-9: CAD model of the new 2-stage resistive feedthrough design with an overlaid axisymmetric electrostatic model showing the distribution of electric fields generated using FEMM software [4].

4.2.3 Construction, fabrication, and testing of the feedthrough

The construction of the feedthrough involved the fabrication of several pieces of hardware in addition to reusing the existing 100 kV ceramic feedthrough, aluminum torus HV platform, molybdenum stalk extender, and blue nylon standoff from the previous feedthrough design. Stages of the construction and testing of the feedthrough are shown in Figure 4-10. Custom 13 mm radius rounded high voltage platforms were machined from aluminum to connect resistors in both stages and facilitate the connection of the HVPS cable to the center conductor and the first stage resistors. The shield horn was produced using a spin manufacturing technique by an outside machine shop and is made of 2 mm thick 1100-O grade aluminum which is mechanically polished. The oil tank was fabricated out of PVC and coated with a conductive spray paint then wrapped with sheet metal and conductive tape to provide a well-defined ground plane. The top aluminum lid flange features ports allowing for the HVPS cable to pass through, a BNC connection for the current sense resistor voltage signal, and two access holes to allow the transfer of dielectric to and from the tank.

Figure 4-10: Assembly of the grids and shield electrodes (left), in air testing of the voltage divider circuit (center), full feedthrough assembly with dielectric oil tank (right).

Testing of the feedthrough circuit was conducted up to 100 kV cathode operation without the dielectric oil and tank assembly in place in order to test for corona formation from regions of high electrical stress and to validate the circuit model calculations of the stage voltages. The first and second stage resistors were assembled in air, and a high voltage probe was connected to either the first stage or second stage to independently measure the stage voltages under plasma operation. The stage voltages were calculated in LabVIEW during operation using the circuit model described previously in section 4.2.1.2. The voltage and current signals from the high voltage power supply along with the current sense resistor are used to determine the voltages at the cathode (first stage) and shield (second stage). The voltage measurements taken from the high voltage probe were found to be in agreement with the calculated values from the LabVIEW data acquisition.

4.2.4 Arc rate diagnostic

During the conditioning process, small arcs may form that are observed as brief spikes in the power supply current monitor signal. These fast transients in the current are about 50-1000 μs in duration and are generally attributed to the removal of high field producing micro features on the cathodes by localized ion bombardment, evolution of gas off an insulating surface creating a flashover event, or partial discharge events occurring within the insulators [2]. If an arcing event spikes the current beyond the power supply's overload current threshold, the power supply will shut down as a safety measure. These shutdowns are frequent in the conditioning process; however, with high voltage conditioning, the frequency of shutdowns at a voltage level may be reduced. Not all arcing events will trip the power supply overload current, and these events may be seen in the sampling of the HVPS signal outputs. An indicator that the conditioning process is working is the reduction in frequency of these small arcs, and a well-conditioned system will have no transient events during steady state operation. The voltage across the feedthrough current sense resistor is monitored by an oscilloscope, which triggers on the fast rise time of the transient voltage pulse from the arcing event shown in Figure 4-11. To prevent overvoltage damage to either the DAQ or oscilloscope, a 12 V transient suppression circuit consisting of back to back Zener diodes is placed between the feedthrough and these instruments. From this configuration, the frequency of arcing events may be monitored, but the magnitude of current excursion is lost due to the transient suppression when the current through the current sense resistor exceeds 12 mA.

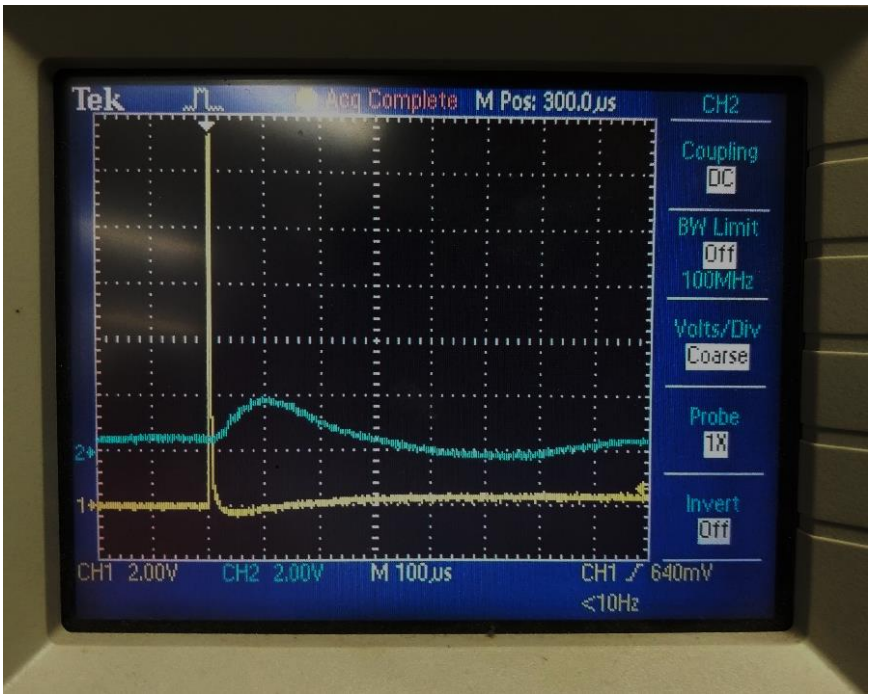

Figure 4-11: Oscilloscope trace of an arcing event captured during the conditioning process. The arc event captured from the current sense resistor (yellow) is more defined than the HVPS current signal (blue).

4.3 Design of the gridded electrodes

The electrode grid configuration chosen for this work was informed from the previous work at UW-Madison as discussed in Chapter 2. A 20 cm diameter cathode grid and 50 cm diameter anode grid were constructed previously by the author to increase the grid spacing uniformity and the rigidity over the earlier grid designs used at UW-Madison and are shown in Figure 4-12. Both the cathode and anode use a 16-9 latitudinal-longitudinal wire configuration to keep the grid holes uniform and symmetric. The cathode is constructed out of 0.76 mm diameter W-25%Re alloy wire, which was chosen for its high melting point (near 3200 ºC) and ability to be spot welded for construction purposes. Improved rigidity in the cathode was achieved by using a rounded molybdenum nut to anchor the longitudinal hoop base structure, spot welding the latitudinal hoops

in place, then spot welding the remaining longitudinal semi-arc segments to the latitudinal hoops, creating an interlacing structure. The anode was constructed using stainless steel wire with a diameter of 1.52 mm for the base structure and 0.76 mm diameter stainless steel wire for the grid wires.

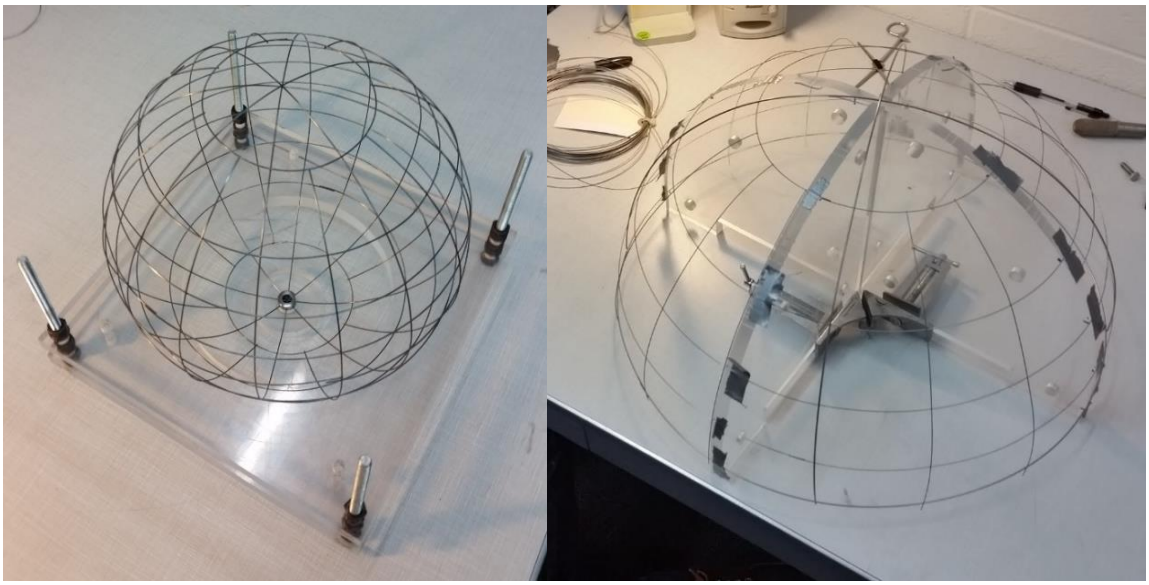

Figure 4-12: Construction of the 20 cm cathode grid (left) and construction of the 50 cm anode grid bottom hemisphere (right).

During the initial testing of the 2-stage resistive high voltage feedthrough, frequent arcouts would trip the high voltage power supply, shutting down the operation when trying to operate at cathode voltages beyond 180 kV. The feedthrough and electrodes were disassembled to check for any electrical wear spots on the insulators and electrodes. The feedthrough components showed little to no sign of electrical wear from the operation; however, there were many trouble areas observed on the anode grid and the chamber walls. Several portions of the anode grid wire had been melted through, along with burn marks observed on the aluminum chamber walls and a melt

spot on the quartz safety glass that protects the vacuum window. It is believed that these melt and burn spots are caused by localized electron heating from electron jets streaming from the cathode. An attempt to fix these issues was made by increasing the longitudinal wire count to 32 and ensuring careful alignment of the cathode-anode hole structures. The effect of adding additional grid wires to the cathode adds more surface area, reducing the geometric transparency of the cathode grid, and may alter the electric field at the wire surface. The upgraded 32-9 longitudinal-latitudinal cathode configuration is shown in Figure 4-13.

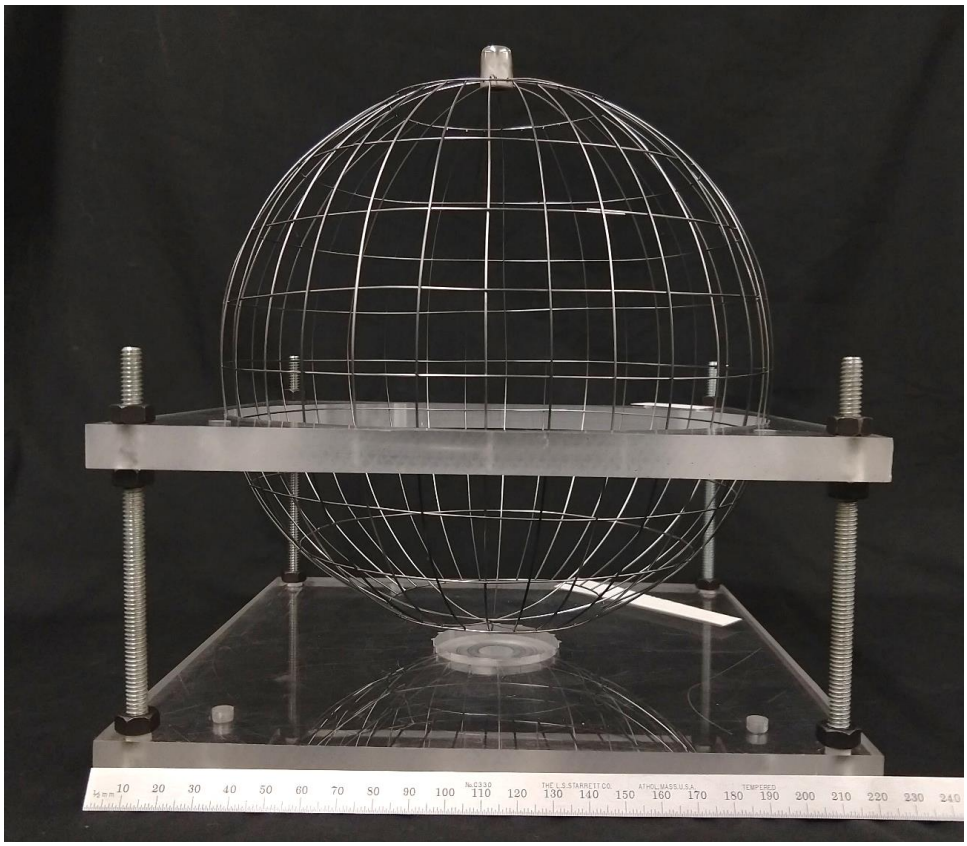

Figure 4-13: The 20 cm cathode modified to have 32 longitudinal wires.

4.4 References

[1] G. F. Knoll, *Radiation detection and measurement*. John Wiley & Sons, 2010.

[2] R. V Latham, *High voltage vacuum insulation: Basic concepts and technological practice*. Elsevier, 1995.

[3] M. K. Michalak, "Increasing the High Voltage Capabilities and Exploring Parameter Space of an Inertial Electrostatic Confinement Fusion Neutron Source for the Detection of Chemical Explosives," Ph.D. dissertation, University of Wisconsin-Madison, 2017.

[4] D. Meeker, "Finite Element Method Magnetics," 2015. [Online]. Available: http://www.femm.info/wiki/HomePage. [Accessed: 03-Dec-2018].

5. New 2-Stage Resistor Divider High Voltage Feedthrough and Modification of Cathode Grid Results and Discussion

This chapter describes the results and performance of the 2-stage resistor divider feedthrough design during hardware testing and plasma operations. An analysis of the feedthrough circuit model is used in predicting the system behavior during plasma operations to better define the system design limits to protect critical hardware components. The results of improving high voltage operations by following the conditioning procedures outlined in Chapter 4 are described. Lastly, the improvements to high voltage standoff due to a modification of the cathode grid are presented and discussed here.

5.1 Voltage divider circuit response under plasma load

Since the feedthrough shield electrode is exposed to charged particle bombardment, a current draw at this electrode will contribute to the high voltage power supply meter current and alter the voltage level of this intermediate platform. A circuit model of the 2-stage resistor divider feedthrough was presented in Chapter 4, which describes the relationship among the high voltage power supply current meter, shield current, and cathode current. Using this model, the voltage divider ratio (V_{shield} / $V_{cathode}$) is found to be dependent on the current collected by the electrostatic shield, I_{shield}:

$$\left(\frac{V_{shield}}{V_{cathode}}\right) = \left(\frac{R_2}{R_1+R_2}\right)(V_{HVPS} - R_{ballast}I_{HVPS})\left[1 - \frac{R_1 I_{shield}}{V_{HVPS} - R_{ballast}I_{HVPS}}\right] \quad 5\text{-}1$$

The ability to predict the voltage drop across the first and second feedthrough stages provides valuable insight in defining the system operational limits where voltage gaps are not to be overstressed and their likelihood of failure is reduced. The previous analysis of the original 2-stage biased feedthrough circuit, which used an independently controlled high voltage power supply, showed a predictable response of the shield electrode current for varying experimental parameters. A similar approach was taken in the initial testing of the new 2-stage resistor divider feedthrough hardware design, where plasmas were operated to map the current collected at the shield electrode as functions of cathode current from 30 to 100 mA, cathode voltage from 80 to180 kV, and chamber pressure at 0.3 and 1.0 mTorr D_2, and the result is shown in Figure 5-1. The relationship between the cathode current and shield current are found to be strongly dependent on the chamber pressure with no significant dependence on cathode voltage for voltages ranging 80 to 180 kV observed; each cluster of points represents data taken between 80 and 180 kV.

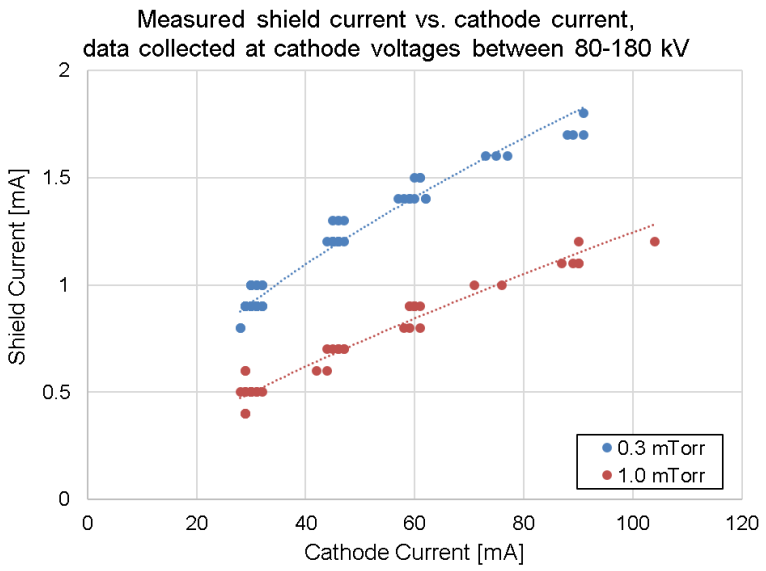

Figure 5-1: Electrostatic shield current draw from the plasma is a strong function of cathode current set point and chamber pressure.

By fitting a power law to the relationship between the cathode current and shield current in Figure 5-1, the circuit model may be used to predict the voltage divider circuit response to a range of cathode current and cathode voltage operating set points. An assumption is made that the shield current dependence on the cathode voltage is weak and is only dependent on the cathode current. For the case of 1.0 mTorr D_2 operation, a shield voltage response is plotted in Figure 5-2 for cathode voltages ranging 80 to 210 kV and cathode currents ranging 0 to 100 mA. As the cathode current goes to zero, the shield current contribution goes to zero; and the circuit response is the current drawn across the ballast resistor and the two resistor stages, all wired in series. With the first stage resistance of 45 MΩ and the second stage resistance of 80 MΩ, this gives a voltage divider ratio of 0.64 (V_{shield} / $V_{cathode}$) under no plasma conditions ($I_{cathode}$ = 0). As the cathode current is increased, the shield voltage is reduced while holding the cathode voltage at the same level.

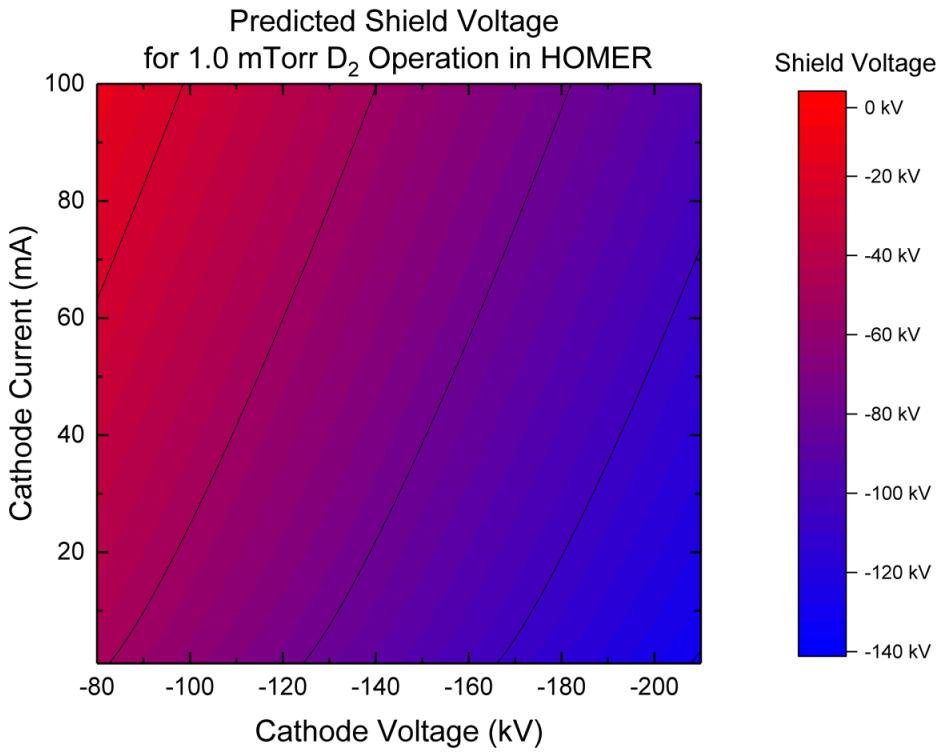

Figure 5-2: Predicted voltage response at the electrostatic shield for varying cathode voltage and cathode current set points during 1.0 mTorr D_2 operation in HOMER.

Holding the cathode current constant, the predicted voltage divider ratio may be examined over a range of cathode voltages using this model. Figure 5-3 shows the model prediction of voltage divider ratio over a cathode voltage range of 0 to 210 kV for cathode currents of either 30 or 100 mA. The assumption that the dependency between the cathode current and shield current is independent of the voltage fails when the shield voltage approaches zero, since the contribution of the shield current must also go to zero.

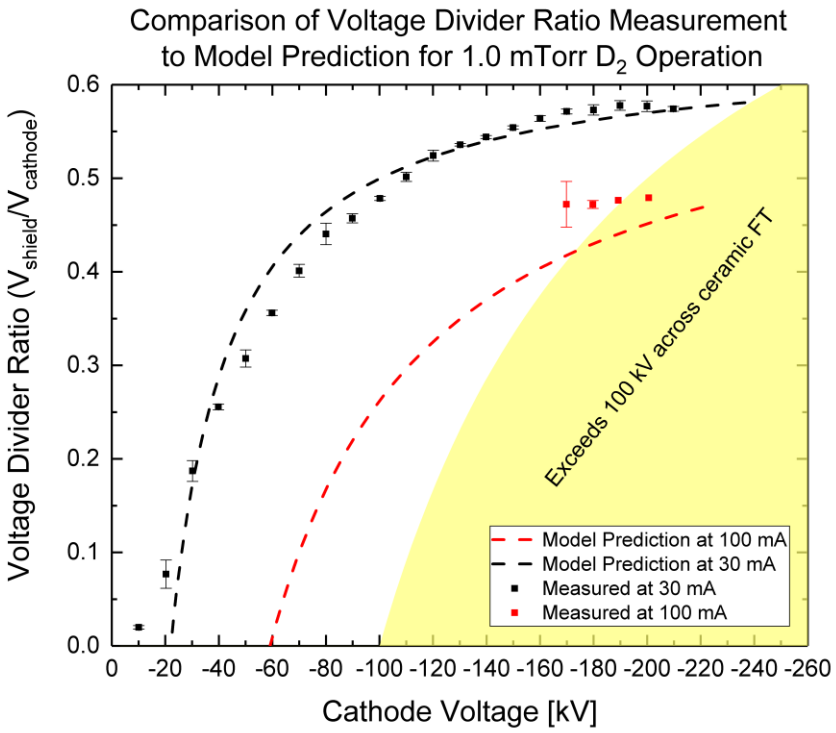

Figure 5-3: A comparison of the predicted versus measured response of the 2-stage feedthrough voltage divider ratio under plasma operating conditions. The yellow shaded region represents where the voltage design limit has been exceeded.

Measurements of the cathode and shield voltages were collected over numerous variations of the system parameters, and data for these two cases are included in Figure 5-3. These measurements represent the average data collected for every 10 kV increment of the cathode voltage (± 1 kV) at cathode currents of 30 or 100 mA (± 1 mA) and chamber pressure 1.0 ± 0.05 mTorr; the error bars represent the standard deviation of the sampled data. Limited measurements were available for the 100 mA case, and only data for 170 to 200 kV cathode operation were collected for this work. This model reasonably predicts the voltage divider ratio for the 30 mA case down to 30 kV at the cathode; however, the model underpredicts the voltage divider ratio for cathode operations at 100 mA.

This model may be used to predict a maximum operational voltage for this feedthrough design under the constraint that the first stage ceramic standoff gap does not exceed 100 kV where the cathode voltage is the sum of 100 kV and the shield voltage. The maximum shield voltage allowed to keep the first stage at 100 kV may be determined by examining the divider ratio:

$$Voltage\ Divider\ Ratio = \frac{V_{shield}}{V_{cathode}} = \frac{V_{shield}}{100\ kV + V_{shield}} \quad 5\text{-}2$$

For the 30 mA and 1.0 mTorr case, a voltage divider ratio near 0.58 is chosen, and a maximum shield voltage is predicted to be 138 kV. A combined shield voltage and 100 kV first stage voltage give a predicted maximum operational voltage of 238 kV at the cathode. The maximum achieved cathode voltage for these conditions was a cathode voltage of 210 kV and shield voltage of 122 kV, falling 28 kV short of the model predicted maximum. This is most likely due to electric fields overstressing the shield electrode gap or the anode-cathode grid gap, leading to arcouts and unstable voltage conditions, which are unable to be mitigated by high voltage conditioning strategies.

5.2 High voltage conditioning results

The installation of the new feedthrough and modified cathode grid required an extensive high voltage conditioning period to improve voltage standoff and stability in HOMER during operation. After installing the new hardware and evacuating the chamber, plasma high voltage conditioning procedures were initiated using deuterium fuel operations. This method of electrode conditioning has been found in the past to reduce the duration of chamber conditioning time when

compared to conditioning procedures using high potential conditioning under no plasma load. Additionally, deuterium plasma conditioning allows for neutron production rate data to be collected during this process and builds up a data set of device performance evolution which will be discussed in Chapter 7. In this system, the onset of significant arcing and voltage instability occurred while operating the cathode at 130 kV at 30 mA and 1.0 mTorr of deuterium. Once the hardware had endured these conditions long enough to significantly reduce the rate of arcing observed, the voltage at the cathode was increased in 5 or 10 kV increments and this new voltage level was held until the rate of arcing observed was reduced once again. To improve the system condition, this procedure was repeated until an upward advancement in voltage standoff could no longer be achieved. Conditioning procedures described in Chapter 4 were successfully implemented to achieve a maximum operational cathode voltage standoff of 210 kV at 30 mA cathode current and a chamber pressure of 1.0 mTorr of D_2 in HOMER.

Figure 5-4 compares two plots of the cathode and shield voltages and cathode current during run conditioning of the system. The top figure shows the device performance earlier in the conditioning process and highlights several features of an unconditioned system. As new voltage levels are reached, the electrode and insulating surfaces require some duration of exposure at these voltages to remove field enhancing or excess current producing features such as sharp micro-features, loose debris, or adsorbed gases on material surfaces. These features tend to burn off due to electron or charged particle bombardment at field enhanced spots on the surfaces under plasma operation, and it is believed that these types of events are responsible for the small current spikes observed in the high voltage trace for the unconditioned system. Large current spikes may trigger the high voltage power supply to shut down when it senses a current draw exceeding a set threshold (up to 200 mA). The high voltage power supply is able to shunt the voltage rapidly to protect the

IEC circuit from dissipating large amounts of energy due to a shorting event, and a high voltage power supply shutdown is seen in this top plot after a fast arc had surpassed the overcurrent limit. The bottom plot shows a later high voltage trace during operation after many conditioning runs where current spikes and fast shutdowns have been eliminated under the same operating parameters.

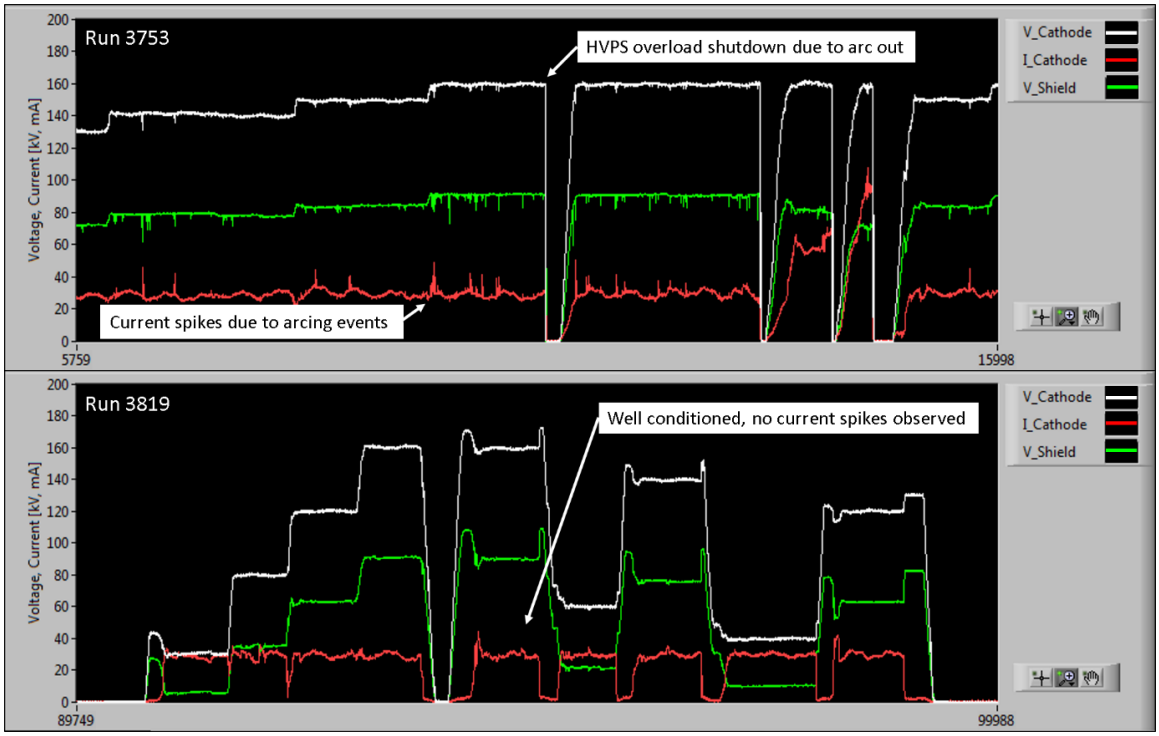

Figure 5-4: High voltage traces are recorded during operations where an unconditioned system (top) shows many arcing events and shutdowns while a conditioned system (bottom) shows stable high voltage operation. The horizontal axis is the data acquisition index and represents the elapsed time of the run.

5.3 Modification of the cathode grid

During the initial testing of the new feedthrough hardware, high voltage conditioning progress stalled at about 180 kV cathode operation. It was initially suspected that there may be a

system standoff limitation at either the feedthrough insulators or the shield electrode; however, no evidence of component degradation or arc spot formation was observed on the feedthrough insulators, shield electrode, or stalk. While examining the cathode and anode grids, several melted spots in the stainless steel anode wires and several burn spots were found inside the chamber as shown in Figure 5-5.

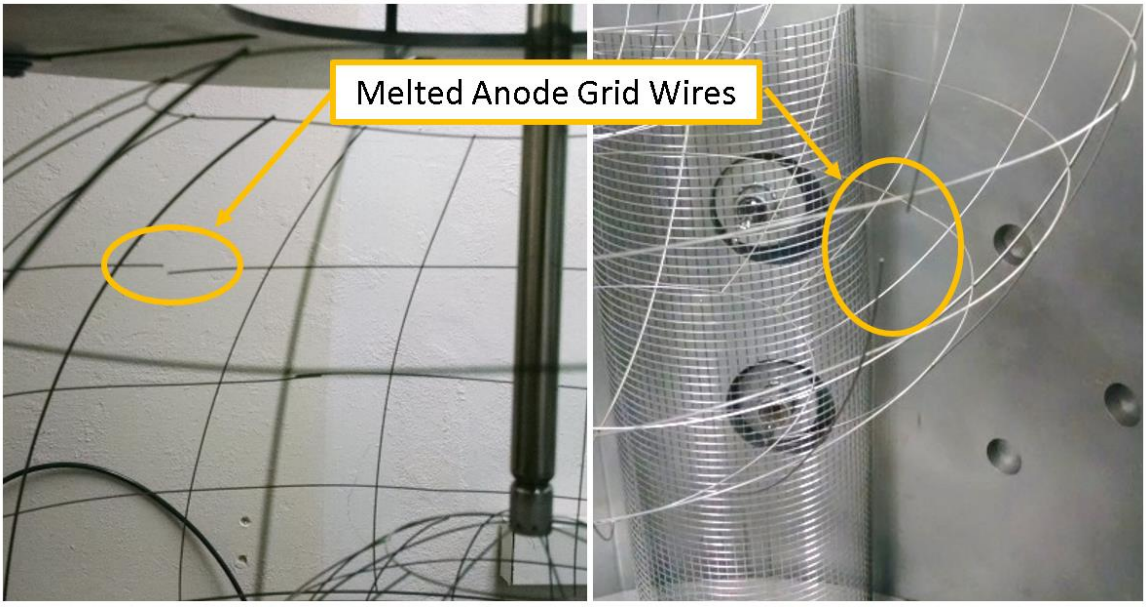

Figure 5-5: Holes melted in the stainless steel anode grid wire due to electron jets.

It is believed that strong electron jets accelerating outward from the cathode region had impinged on these spots, and the presence of electron jets was previously presented in Chapter 3. Electron jets have been found to have a sufficient power density to melt through the stainless steel anode wires, create scorch marks on the chamber wall, and form melt spots in a quartz safety glass which protects the vacuum window barrier. These jets, which occur more intensely during high cathode current operation, may lead to electro-thermal instabilities of the high voltage electrodes

resulting in current spikes, power supply shutdowns, and occasionally melting of chamber hardware. In an attempt to mitigate the impact of the jets while operating HOMER at cathode voltages above 170 kV and currents above 60 mA, careful positioning of the grid wires was made to ensure the hole positions were aligned, and an attempt to reduce the electric field at the cathode surfaces was made by the addition of more wires.

The previously used cathode grid was modified by adding additional longitudinal wires to decrease grid hole size and reduce electric field at the cathode wires. New W-25%Re grid wires of 0.76 mm diameter were spot-welded to the previous 20 cm diameter 16-9 longitude-latitude wire cathode grid, designated W-20, to increase the number of longitudinal wires to 32; this new 32-9 longitude-latitude configuration is designated grid configuration W-21 for the purposes of this work. The addition of these grid wires reduces the geometric transparency; however, the reduction in effective transparency to ion flow is expected to have a smaller effect due to the micro-channeling of charged particles through the cathode previously discussed in Chapter 3. In addition to modifying the cathode, the melted portions of the anode grid wire were replaced with new sections of stainless steel wire. The cathode and anode were installed in HOMER, and the high voltage conditioning process was restarted using the plasma conditioning technique.

To compare the performance of the revised grid design, a glow discharge voltage breakdown curve was created for the previous and new configurations, and the results are shown in Figure 5-6. This test was conducted by setting the chamber pressure then turning up the cathode voltage until a glow discharge is initiated; the breakdown voltage is determined as the cathode voltage where a plasma is initiated and current draw across the gap is observed. This test of breakdown voltage does not use the ionization filament assist typically used to control the cathode current during normal operations, and the result of this test shows an improvement of cathode

voltage standoff before initiation of a glow breakdown regime for the same deuterium chamber pressure for the new configuration. At a chamber pressure of about 1.2 mTorr, the breakdown voltage for the W-21 configuration was found to be nearly 50 kV higher than the W-20 configuration. This improvement in voltage standoff allowed for more stable operations at cathode voltages beyond 180 kV and ultimately achieved a peak operational standoff voltage of 210 kV. Despite the improved performance of this revised grid, melting of anode grid wires due to electron jets was still an issue for this system, and a solution to this problem remains to be found.

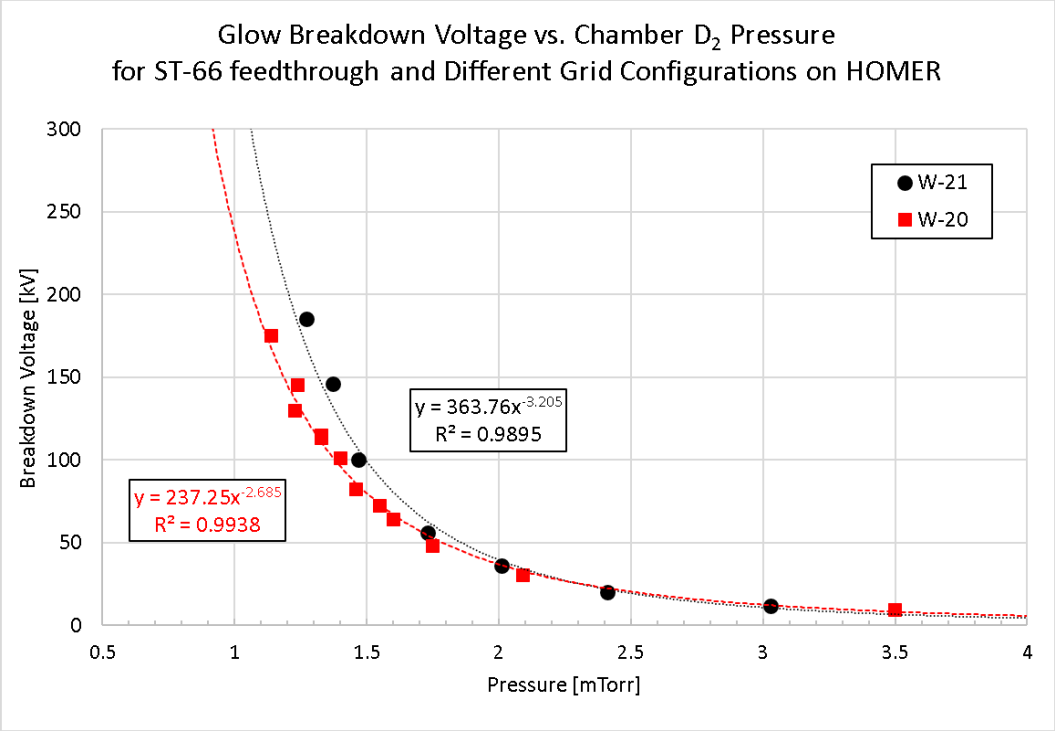

Figure 5-6: A comparison of high voltage breakdown curves shows the increased performance of the 32 longitudinal cathode wire grid over the 16 longitudinal cathode wire grid configuration using the new feedthrough design in each test.

5.4 Summary

The 2-stage resistive divider high voltage feedthrough was successful in achieving the goal of 200 kV operation in an IEC device. The 2-stage approach has been found to be robust against destructive arcs and failures of past designs by implementing the use of an intermediately biased electrostatic shield to protect the secondary stage insulating standoff from charge particle bombardment. The circuit model shows the voltage divider ratio may shift depending on the plasma conditions in the chamber, and this model may be used to predict operational limits. The plasma conditioning process has been found to be an effective means to improve the high voltage standoff of the cathodes using deuterium fuels. Concentrated electron jets accelerated outward from the cathode region are found to be detrimental to the anode structures they impact; at high enough voltages and currents, these jets have been found to melt stainless steel wires and quartz glass in the chamber. The approach to achieve higher voltage standoff by improving grid alignment and by adding additional grid wires was successful in improving the high voltage standoff before initiation of glow discharge breakdown. The result of this new 2-stage feedthrough and modified cathode grid was the achievement of a maximum high voltage cathode operation at 210 kV and 30 mA for a 1.0 mTorr deuterium pressure during plasma operation.

6. Parametric Study of Neutron Production Rates Results and Discussion

This chapter presents the results of experimental investigations of the neutron production rate scaling with input parameters for the gridded IEC device HOMER. In this device, three key parameters have been identified that influence the neutron production rate: the cathode voltage, which influences the energy distribution of deuterium ions, the cathode current, which influences the density of ion current, and the chamber pressure, which may influence the deuterium target density and ion energy distribution. The geometric configuration may also influence the neutron production rate performance; however, the geometry remains fixed for all experimental studies in this work. Parametric scans of the neutron production rate for variations on cathode current (30–100 mA), chamber deuterium pressure (0.2-1.5 mTorr), and cathode grid voltage (10-210 kV) are presented here in Section 6.1. Comparisons of this data are made to previous work performed by Michalak that studied parametric scaling of neutron production rates in HOMER up to 175 kV. Neutron production rate scaling measurements are also compared to theoretical predictions using the VICTER model. A discussion of these results and comparisons is presented in Section 6.2

6.1 Experimental results for parametric studies of neutron production rates

The experimental results presented in this section are generated using the new 2-stage resistor divider feedthrough hardware and a spherical electrode set using a 20 cm diameter 32-9 longitude-latitude spherical cathode grid and a 50 cm diameter 16-9 longitude-latitude anode grid. For the following results, the cathode voltage represents the voltage at the cathode grid and center conducting stalk. This cathode voltage is of negative polarity with respect to the grounded anode

grid and grounded chamber walls, and the voltages reported here are with a negative polarity implied. Details of the HOMER experimental setup are presented in Chapter 4, and the neutron counts are measured using the ^{3}He proportional counter with a single channel analyzer counting system described previously.

Experimental uncertainties in the neutron production rate measurements presented in the following sections are calculated by considering sources of error in the instrument set points, uncertainty in the neutron calibration factor, and the Poisson counting error in the neutron count measurements. Measurements of the neutron counts are selected from the run data of interest that meet the following criteria (unless otherwise noted): within ±1 kV of the cathode voltage set point, within ±1 mA of the cathode current set point, and within ±0.05 mTorr of the chamber pressure set point. Neutron counts and counting duration are summed over all measurements meeting the selection criteria, and the measured count rate is computed, dead time corrected, and multiplied by the calibration factor to give the true neutron production rate measurement. Counting error is calculated by the square root of the total counts and divided by the count duration to give the measured count rate uncertainty; the uncertainty in the computer sampling timing is considered negligible. The uncertainties of the count rate measurement and the calibration factor are propagated to give a measurement uncertainty in the true neutron production rate. The measurements of voltage, current, and pressure set points are respectively averaged over all the data meeting the selection criteria. The standard deviation of the free parameter measurements is calculated, and the relative error of the mean fixed parameter measurement is taken with respect to the reported set point values. The relative set point errors for the constrained parameters and the standard deviation of the free parameter are propagated with the true neutron production rate uncertainty to give the final experimental uncertainty of the measured true neutron production rate;

this uncertainty assumes only first order contributions with any covariance neglected. The true neutron production rate and experimental uncertainty are represented in the neutron production rate measurements presented in this chapter.

6.1.1 Variation of cathode current

Neutron production rate measurements were taken by fixing the cathode voltage and deuterium chamber pressure set points and varying the set point of the current measured at the cathode grid. Data presented in Figure 6-1 shows the neutron production rate measurements for cathode currents varying 30 to 100 mA with cathode voltage set points ranging from 170 to 200 kV and 1.0 mTorr deuterium pressure. For each fixed level of the cathode voltage, the order of cathode current set points chosen to measure the neutron production rate response was randomized and distributed over a series of four runs performed in one day. The data for the 170 kV cathode voltage case was taken in a single day with the data for the 180 kV case taken the following day and then incremented each day for the 190 and 200 kV cases.

The maximum neutron production rate result of current scans performed between Runs 3788 to 3811 is a neutron production rate measurement of 3.8×10^8 n/s at the experimental parameters: 98 mA, 190 kV, and 1.0 mTorr D_2 where 10 seconds worth of counting data were collected. An attempt was made to measure the neutron production rate at 200 kV cathode voltages at cathode currents above 60 mA; however, the cathode voltage standoff under these conditions was unstable, and measurements of the neutron production rate were not achieved at these conditions.

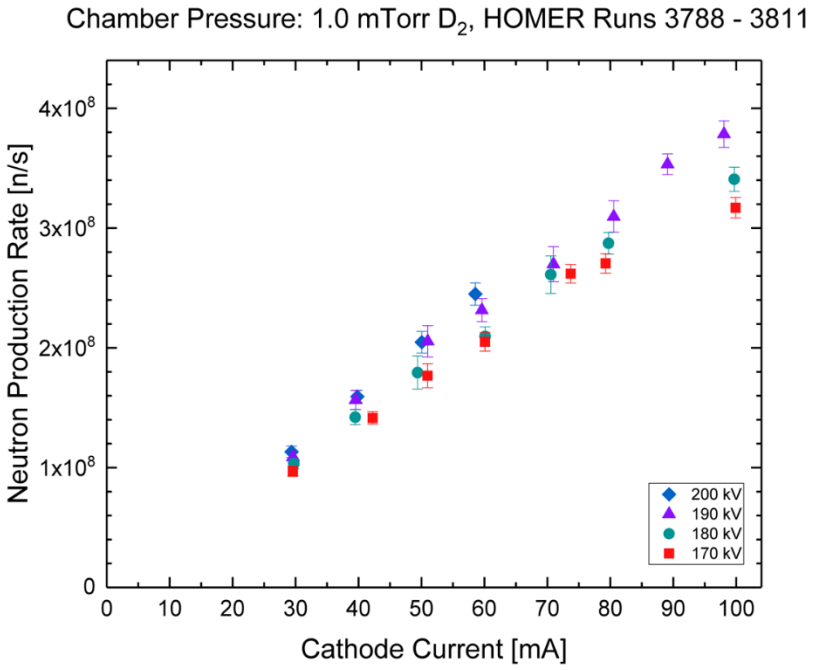

Figure 6-1: Neutron production rate measurements for cathode currents 30 to 100 mA, cathode voltages ranging 170 to 200 kV, and chamber pressure of 1.0 mTorr D_2.

A second attempt at measurements of the neutron production rate at 200 kV, 100 mA was made during a separate data run at a later date. To achieve better high voltage standoff at these levels, the experiment was vented before Run 3843 to mend an anode wire melted by an electron jet during a prior operation of HOMER. The system was pumped back down, and measurements of the neutron production rate were performed up to a 200 kV cathode voltage. These measurements, shown in Figure 6-2, were collected by operating at 170 kV and measuring the neutron counts taken at cathode currents from 30 mA increasing sequentially up to 100 mA. Measurements were then collected for a 200 kV set point starting at 30 mA and sequentially increasing in cathode current up to 100 mA.

The maximum neutron production rate result of current scans performed during Run 3843 is a neutron production rate measurement of 3.8×10^8 n/s at the experimental parameters: 100 mA, 200 kV, and 1.0 mTorr D_2 where 12 seconds worth of counting data were collected. A comparison of this data set and data from the current scan presented in Figure 6-1 is made in Section 6.2.2.

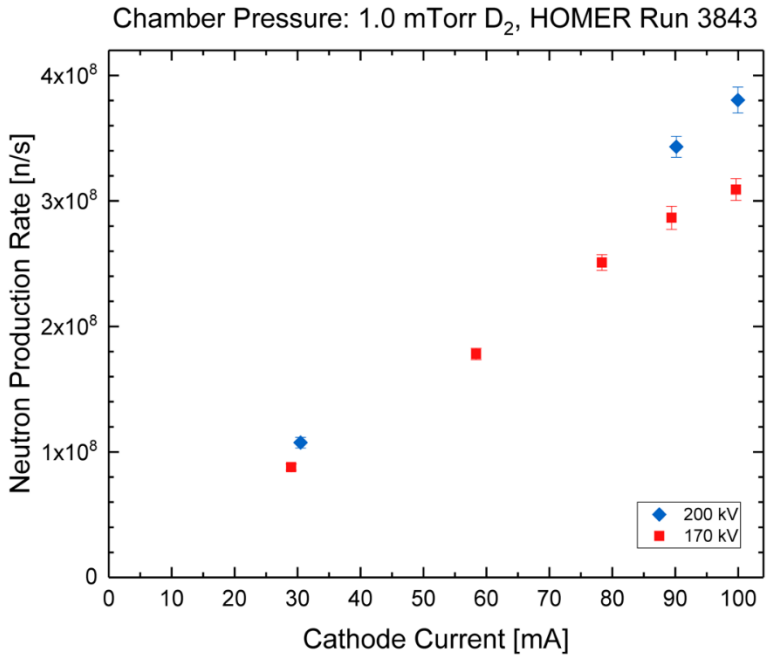

Figure 6-2: Neutron production rate measurements for cathode current 30 to 100 mA, cathode voltages at 170 and 200 kV, and chamber pressure of 1.0 mTorr D_2 operation for HOMER Run 3843.

6.1.2 Variation of deuterium fuel pressure

Neutron production rate measurements were taken by fixing the cathode voltage and cathode current set points and varying the set point of the chamber deuterium pressure. Data presented in Figure 6-3 shows the neutron production rate measurements for cathode currents varying 0.2 to 1.5 mA with cathode voltage set points ranging from 50 to 200 kV and cathode current set point of 30 mA. For each fixed level of the cathode voltage, the order of chamber pressure set points chosen to measure the neutron production rate response was randomized and recorded in a single run. The data for the 50 kV cathode voltage case was taken first with the data for the 100 kV case taken the following run and then incremented each run for the 150 and 200 kV cases.

Figure 6-3 shows a rolling over in the neutron production rate performance with increasing deuterium pressure for all fixed voltage cases. Operation of the experiment was limited at each voltage level on the higher pressure side due to the pressure at which the system transitions into a glow discharge regime; measurements of neutron production rate under glow discharge conditions are not considered in this work. For the fixed 200 kV case, high voltage operation below 0.7 mTorr was found to be unstable, and no measurements of the neutron production rate were made. Examining the 100 kV case, the neutron production rate increased by a factor of 2.4 when the pressure was increased a factor of 6.2, from 0.23 mTorr to 1.42 mTorr. A discussion of this rolling over of neutron production rate with the increase in deuterium pressure is presented in Section 6.2.3.

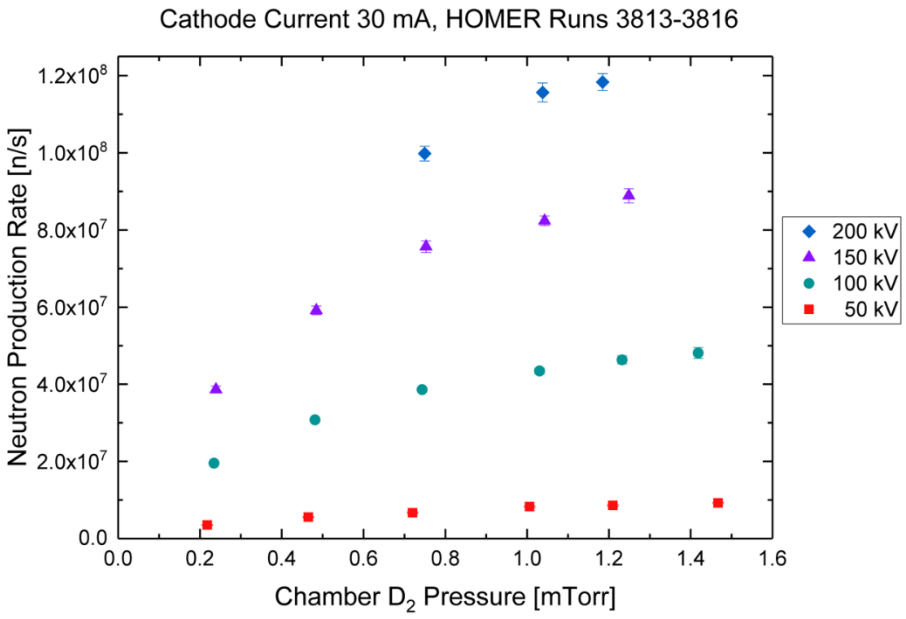

Figure 6-3: Neutron production rate measurements with varying deuterium chamber pressures of 0.2 to 1.5 mTorr D_2, cathode voltages ranging 50 to 200 kV, and a cathode current of 30 mA in HOMER.

6.1.3 Variation of cathode voltage

Neutron production rate (NPR) measurements were taken by fixing the chamber pressure and cathode current set points and varying the set point of the cathode voltage. Data presented in Figure 6-4 to Figure 6-6 show the neutron production rate measurements for cathode voltages varying 10 to 210 kV with cathode current at 30 mA and a chamber pressure set point at 1.0 or 1.2 mTorr. For each data set, the order of cathode voltage set points chosen to measure the neutron production rate response was randomized and distributed over a series of four runs performed in one day. Measurements of the neutron production rate were taken in either 5 or 10 kV increments, and the presented data was reduced by selecting only data within ± 2.5 kV about the set point. A discussion of the results is presented in Section 6.2.4.

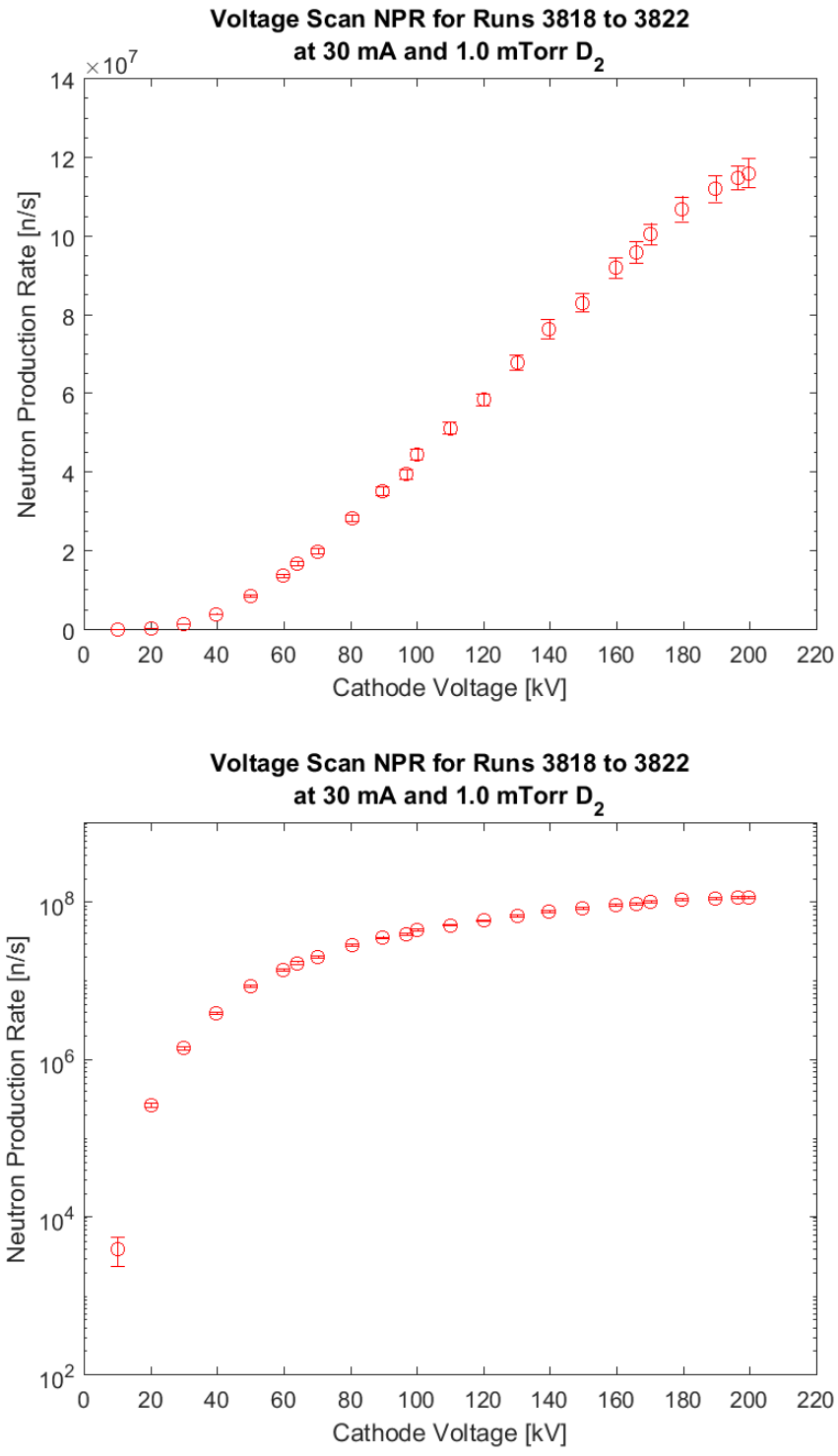

Figure 6-4: Neutron production rate measurements for cathode voltages ranging 10 to 200 kV, cathode current 30 mA, and chamber pressure of 1.0 mTorr D_2 in HOMER. Data is presented linearly with neutron production rate (top) and logarithmically with neutron production rate (bottom).

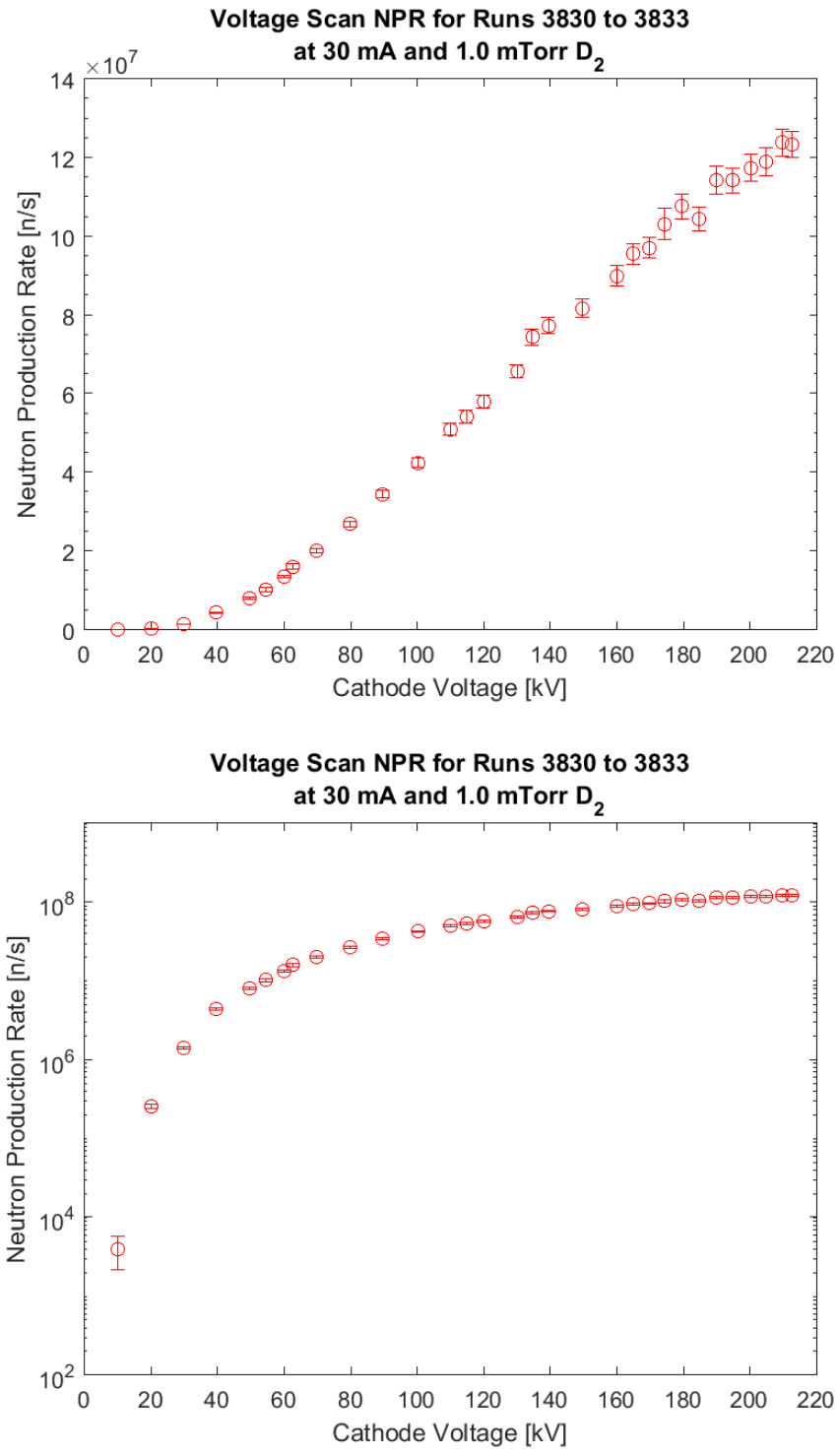

Figure 6-5: Neutron production rate measurements for cathode voltages ranging 10 to 210 kV, cathode current 30 mA, and chamber pressure of 1.0 mTorr D_2 in HOMER. Data is presented linearly with neutron production rate (top) and logarithmically with neutron production rate (bottom).

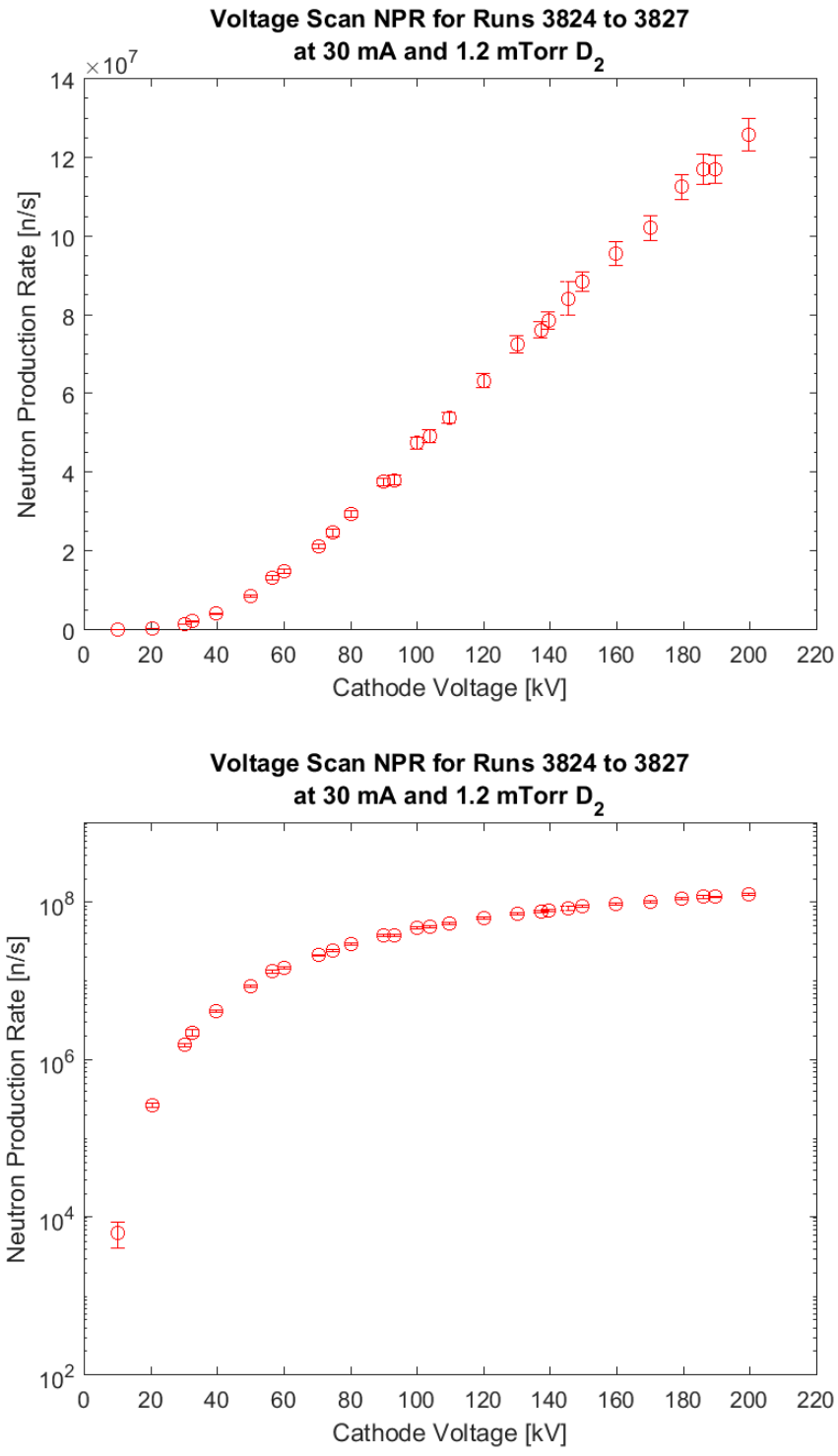

Figure 6-6: Neutron production rate measurements for cathode voltages ranging 10 to 200 kV, cathode current 30 mA, and chamber pressure of 1.2 mTorr D_2 in HOMER. Data is presented linearly with neutron production rate (top) and logarithmically with neutron production rate (bottom).

6.2 Discussion of the parametric neutron production rate experimental results

The results of the parametric scans in the previous section reveal information about the fusion reaction regimes present in this system, and measurements of the neutron production rate may be compared to theoretical expectations for these conditions. Past experimental diagnostic and theoretical work presented in Chapters 2 and 3 have informed the presence of several key physical phenomena at play in the gridded IEC device. The VICTER code [1], [2] was developed by Emmert and Santarius to model the physical effects of particle collisions in IEC devices, and this model is used to predict neutron reaction rate response to the device cathode voltage, ion current, and chamber background pressure for deuterium fuel in a spherical geometry. Comparisons to past experimental results and to theoretical predictions of the neutron production rate response using the VICTER model are presented in the following sections.

6.2.1 Comparison to previous work

A comparison of the data in this work was made to the previous work of Michalak [3] which studied neutron production rate scaling in the HOMER IEC experiment for voltages up to 175 kV and 100 mA. The hardware configuration in this past work used the actively biased 2-stage feedthrough and a 20 cm diameter16-9 longitude-latitude cathode and 16-9 longitude-latitude anode grids describe previously in Chapter 4. The uncertainty in the measurements of the previous work are represented by the uncertainty in the counting measurements and the error from parameter set points is assumed insignificant. Measurements of the neutron production rate for similar fixed parameter set point conditions are compared between this work and the past work for variations of the cathode current and the cathode voltage.

Figure 6-7 shows a comparison of the measured neutron production rate response with varying cathode current ranging 30 to 100 mA with a fixed cathode voltage at 170 kV and chamber deuterium pressure at 1.0 mTorr. Additionally, Figure 6-8 shows a comparison of the measured neutron production rate response with varying cathode voltage ranging 10 to 210 kV with a fixed cathode current at 30 mA and chamber deuterium pressure at 1.0 mTorr. The measurements of the neutron production rate taken for similar conditions of voltage, current, and pressure are found to be consistent between the two experimental setups despite using different configurations. The hardware used in this work used the 2-stage resistor divider feedthrough, which featured a different shield voltage biasing circuit, electrostatic shield profile, and cathode grid configuration than the previous work. The consistency in the measurements indicates these changes in the experimental geometry and feedthrough circuit have a negligible impact on the neutron production rates under similar operating conditions.

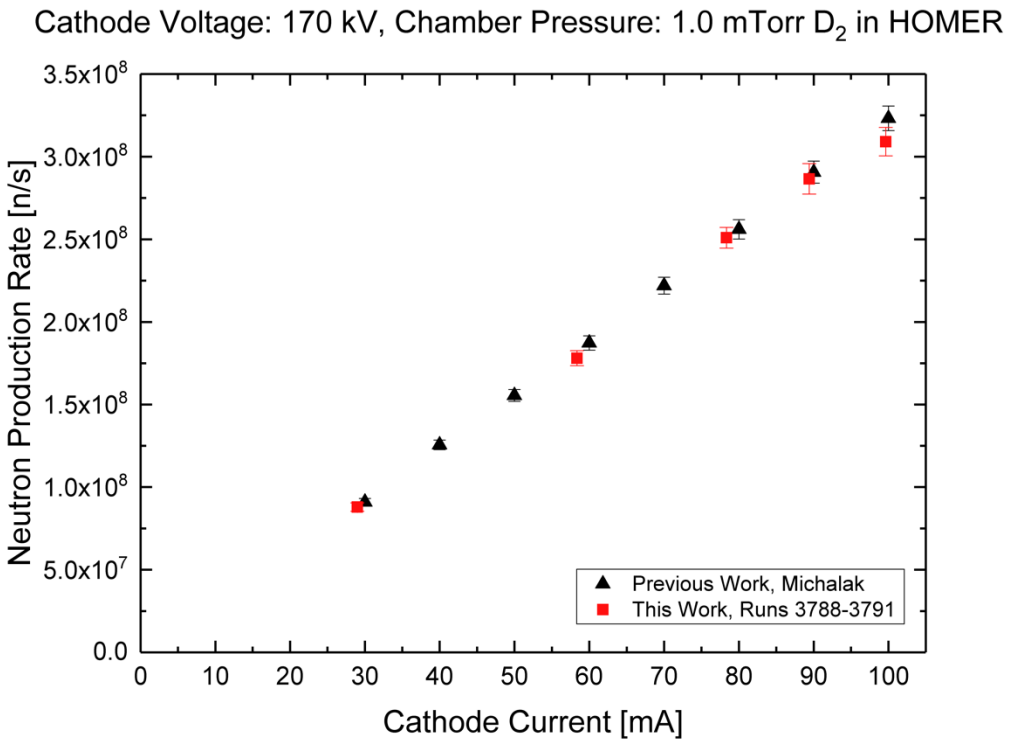

Figure 6-7: A comparison of neutron production rates the between previous work and this work shows agreement in the measurements taken at a cathode voltage of 170 kV for currents ranging 30 to 100 mA at 1.0 mTorr D_2 chamber pressure in HOMER.

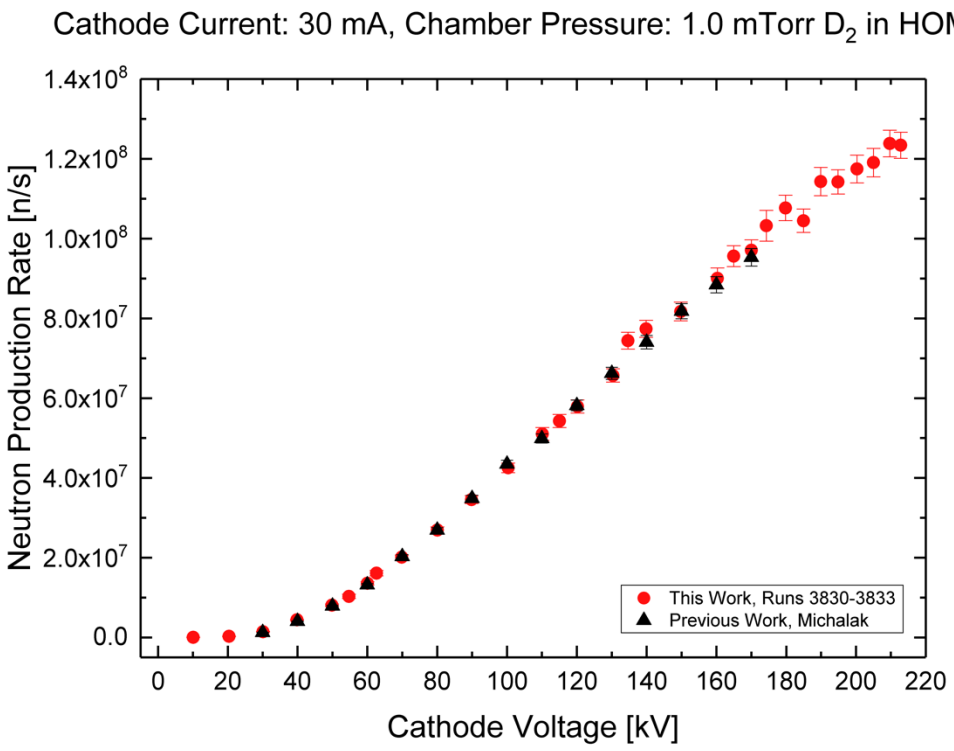

Figure 6-8: A comparison of neutron production rates between previous work and this work shows agreement in the measurements taken at a cathode current of 30 mA for cathode voltages ranging 30 to 100 mA at 1.0 mTorr D_2 chamber pressure in HOMER.

6.2.2 Variation of cathode current

Fusion reactivity due to fast deuterium ion collisions with background deuterium particles (beam-background) or with embedded deuterium in solids (beam-embedded) will scale linearly with the ion current, and fusion reactivity due to a collision of two fast deuterium ions (beam-beam) will scale with the square of the ion current. Since the fusion reactivity is related to the neutron production rate by a 50% branching ratio of the DD reaction products, the observed neutron rate scaling will follow the same scaling as the fusion reactivity. An examination of the experimental results presented in Figure 6-1 is performed by applying a zero intercept least squares linear fit of the data for each fixed voltage case to examine the linearity of the measurement scaling with cathode current and is presented in Figure 6-9. Since the ion current in the gridded IEC device is directly proportional to the cathode current, these result shows that neutron production rate measurements up to 200 kV demonstrate a linear scaling of cathode current (and thus ion current) which is consistent with a device operating in a beam-background and beam-embedded fusion reaction regime.

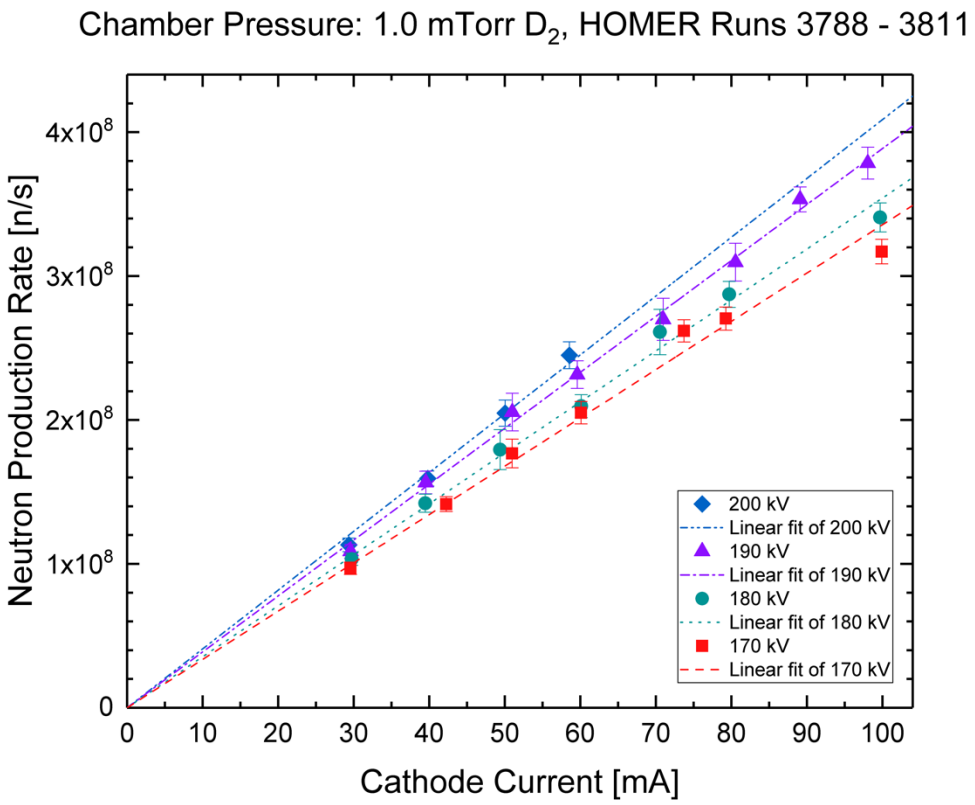

Figure 6-9: Neutron production rate measurements demonstrate a linear dependency with cathode currents ranging 30 to 100 mA, cathode voltages 170 to 200 kV, and chamber pressure of 1.0 mTorr D_2 in HOMER.

A neutron production rate measurement of 3.8×10^8 n/s for experimental set points of cathode voltage: 200 kV, cathode current: 100 mA, and chamber pressure: 1.0 mTorr D_2 was made during a later run, shown in Figure 6-2, where the hardware configuration remained the same, but the chamber condition was altered due to a venting procedure preceding the run. Since the neutron production rate is found to scale linearly with the cathode current, an extrapolation of the linear fit of the 200 kV data from Figure 6-9 would predict a neutron production rate of 4.1×10^8 n/s with a 95% confidence interval of 3.9×10^8 to 4.3×10^8 n/s. The discrepancy this measured neutron production rate with the extrapolated data prediction is believed to be caused by altered baseline chamber conditions due to impurity gas introduced during the venting procedure. The impact of impurity gas on the system will be considered in Chapter 7.

6.2.3 Variation of deuterium fuel pressure

The results presented in Figure 6-3 show a rolling over in neutron production rate with the increase in chamber background gas pressure for all fixed voltage cases which indicates non-linear effects are present. Fusion reactivity for reactions consisting of mono-energetic beam-background collisions scale linearly with the background deuterium density and thus will scale linearly with the chamber background pressure while the reaction cross section remains invariant for the mono-energetic species. This assumption of mono-energetic species is invalid since fast deuterium collisions with atomic and molecular species in the system will redistribute the energy of the fast deuterium species leading to a softening of the energy spectrum of reacting particles and a diminished reaction cross section contribution for each reaction to the total fusion reactivity. This can occur in the system by the presence of molecular dissociation, charge exchange, or ion impact ionization reactions. The effect of increasing pressure is thus: the neutron production rate increases

with the background density and the neutron production rate will decrease with a softened energy spectrum of the fast deuterium particles caused by increased collisions with increased background density and the ionization of deuterium species part way down the potential well resulting in a maximum energy less than the full anode-cathode potential difference.

The analysis of the current scaling in the previous section indicates this system is operating in a beam-background reaction regime, and neutron production rates are expected to demonstrate this scaling. Fusion reactions caused by fast deuterium interacting with embedded deuterium within solids are presumed to contribute some portion of the measured neutron production rate, and the magnitude of this contribution is considered further in Chapter 7. The neutron production rate dependence on chamber pressure normalized to the 0.2 mTorr measurements is shown in Figure 6-10 to examine the rate increase factors for different cathode voltage set points. The increase in neutron production rate is seen to be about a factor of 2.5 for increasing the chamber pressure by a factor of 6 over the 0.2 mTorr chamber pressure measurements for all voltage cases. This indicates that non-fusion producing deuterium collisions with background species will affect the neutron production rate performance of the device. The curvature of the neutron production rate response also suggests the energy spectrum softening of fast species has a stronger effect as the pressure increases over this pressure range. Previous measurements from the FIDO diagnostic [4] and the neutral particle analyzer [5] have experimentally measured these energy spectra softening effects in HOMER up to 60 kV cathode operation. The increase in neutron production rate across this pressure range is consistent for cathode voltage set points ranging 50 to 150 kV, which indicates the energy spectrum softening due to collisions is a strong effect and does not seem to be enhanced or diminished over this range of cathode voltages. The VICTER model was used to calculate the fusion reaction rate response

with increasing pressure over the same range, and the results showed the model predicts a greater than linear increase with pressure. The model predicts a divergence in the neutron rates with increasing pressure among the different voltage cases with the lower cathode voltage cases out-performing the higher voltage cases, and this discrepancy in scaling suggests that some unaccounted for physical process may be missing from the model.

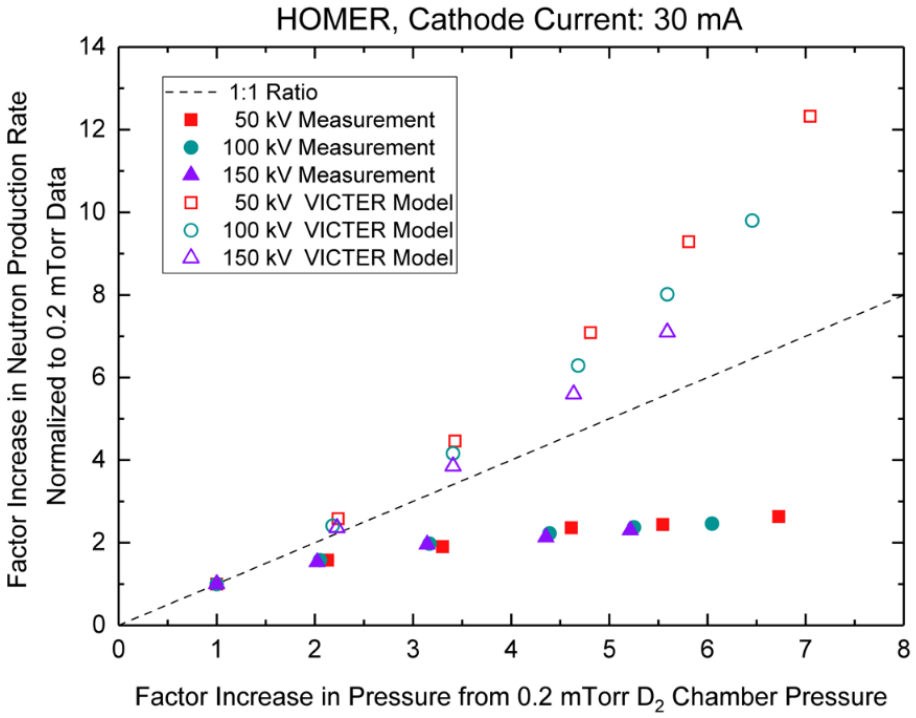

Figure 6-10: Neutron production rate scales less than linear with increasing chamber pressure from 0.2 to 1.5 mTorr D_2 while the VICTER model predicts a greater than linear increase with increasing pressure.

6.2.4 Variation of cathode voltage

6.2.4.1 Neutron production rate reproducibility with cathode voltage variation

A check on the system to examine the reproducibility of the neutron production rate dependence on voltage was performed for a fixed cathode current of 30 mA and chamber deuterium pressure of 1.0 mTorr. Two scans were performed during separate times in the run campaign, and for each of the data sets, the order of voltage set points selected to measure the neutron production rate was randomized. Figure 6-11 shows these two scans plotted together demonstrate reproducibility in the data for these parameters. A greater than linear increase in the neutron production rate is observed for cathode voltages increasing until about 60 kV where the production rate falls off to a linear response with the cathode voltage up to 180 kV; the neutron production rate is then observed to increase at a less than linear rate with voltages 180-210 kV.

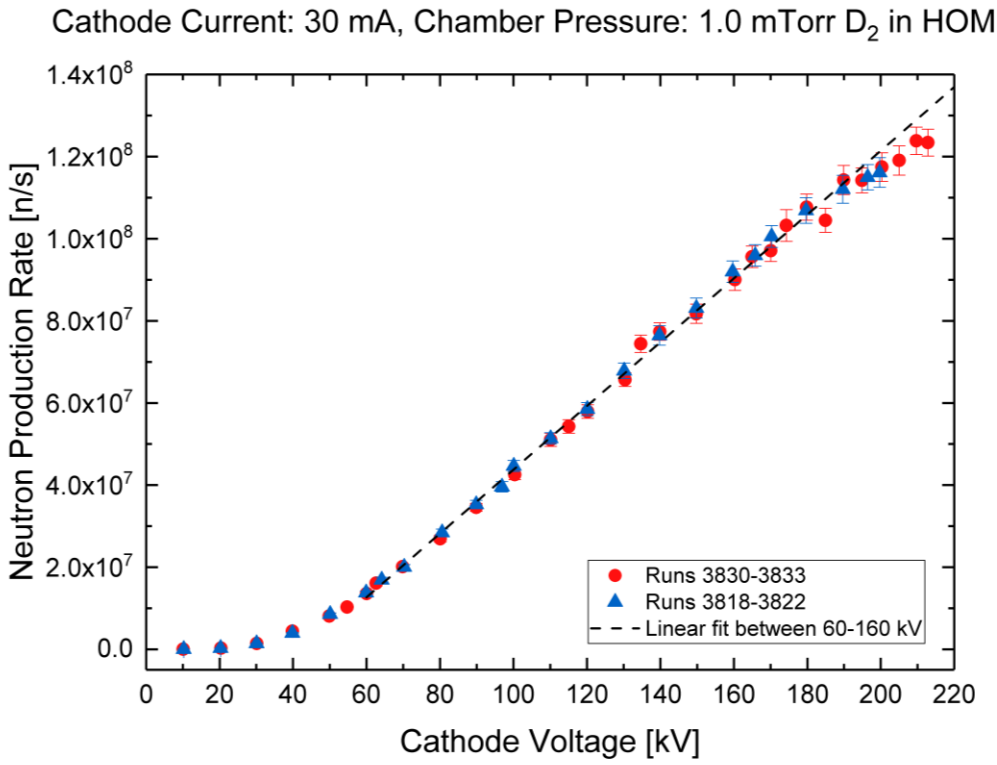

Figure 6-11: A comparison of two data sets shows reproducibility in measurements taken for cathode voltages 10 to 200 kV, while operating at 30 mA cathode current and a chamber pressure of 1.0 mTorr D_2 in HOMER.

Careful consideration must be given to the energy distribution of reacting species if the neutron production rate is to be well understood. Fusion reactivity for beam-background type collisions scales with the reaction cross section which is dependent on the energy of the reacting species. The energy spectrum of the reacting particles is complex due to the presence of non-fusing fast ion collisions with neutral particles resulting in charge exchange, ion impact ionization, negative ion formation, and molecular deuterium dissociation reactions. These reactions may result in deuterium ions born partially down the potential well, negative ions accelerated outward from the cathode, and fast neutral particles unconfined from the potential well. The overall effect of

these collisions is the redistribution of the energy for ions born outside the potential well region that are accelerated by drifting into the potential well, and a softening of the reacting deuterium energy spectrum from the full cathode potential.

6.2.4.2 Comparison of measurements to the VICTER model

The VICTER model considers these non-fusing ion collision reaction cross sections along with the energy and radial distributions of fusing deuterium reactions, and a prediction of the system neutron production rate response may be made. Figure 6-12 shows the VICTER model prediction for the neutron production rate dependency on cathode voltages ranging from 10 to 200 kV at a cathode current of 30 mA and chamber pressure of 1.0 mTorr D_2 using a 20 cm diameter cathode and 50 cm diameter anode configuration. The model is plotted along with the experimentally measured neutron production rate response for similar fixed conditions for comparison, and the VICTER model is found to under predict the neutron production rate response across the cathode voltage range by nearly an order of magnitude.

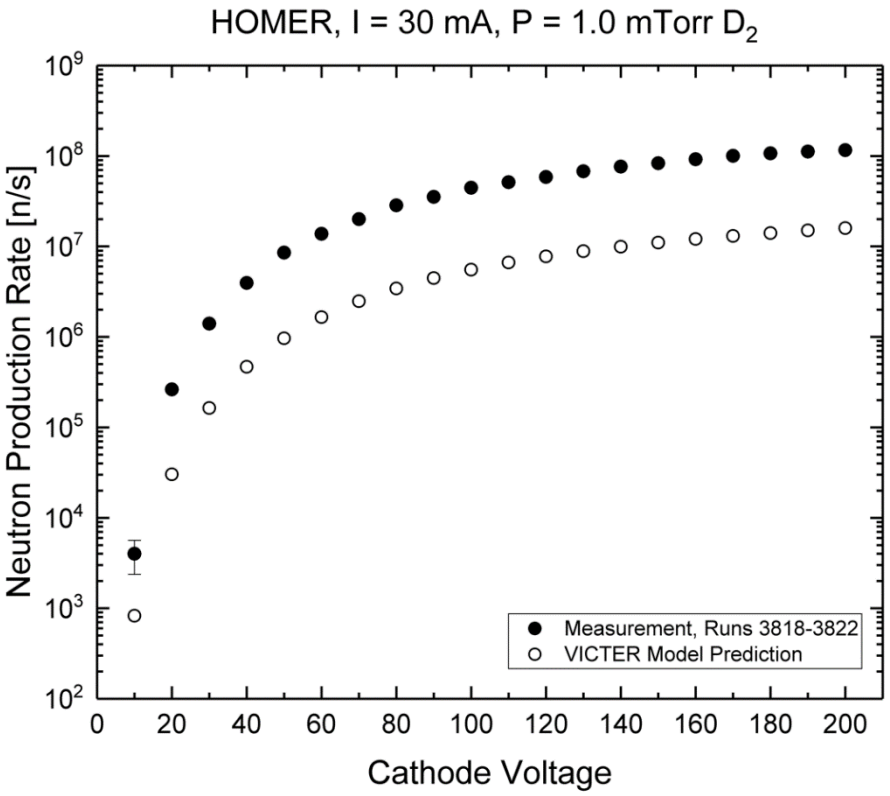

Figure 6-12: A comparison of the absolute neutron production rate response of HOMER for cathode voltages 10 to 200 kV, cathode current of 30 mA, and chamber pressure 1.0 mTorr D_2 shows the VICTER model under predicts the measured response.

The discrepancy in the measured response versus the VICTER model prediction is investigated by performing a linear least squares fit between the model results and the experimental measurements, shown in Figure 6-13, to determine the magnitude of rate disparity and to look for nonlinear deviations. The linear fit of the data indicates the measured neutron production rate is about a factor of 7.84 times greater than the VICTER model prediction. The residuals are represented here by a percent difference of the measurement with respect to the linear fit for clarity over five decades of response. The measurements when compared to the linear fit show nearly all points fall within a 10% range from this fit. This suggests that most of the discrepancy between the measurement and model are recovered by simply scaling the model by a factor of 7.84. The residuals of this fit also indicate that linear scaling will generally under predict the response for cathode voltages below 100 kV and over predict measurements above this voltage and that a weakly non-linear offset between the VICTER predicted response and the experimental measurements exists. Figure 6-14 shows the VICTER model predicted neutron production rate multiplied by a factor of 7.84 in comparison to the experimentally measured rate.

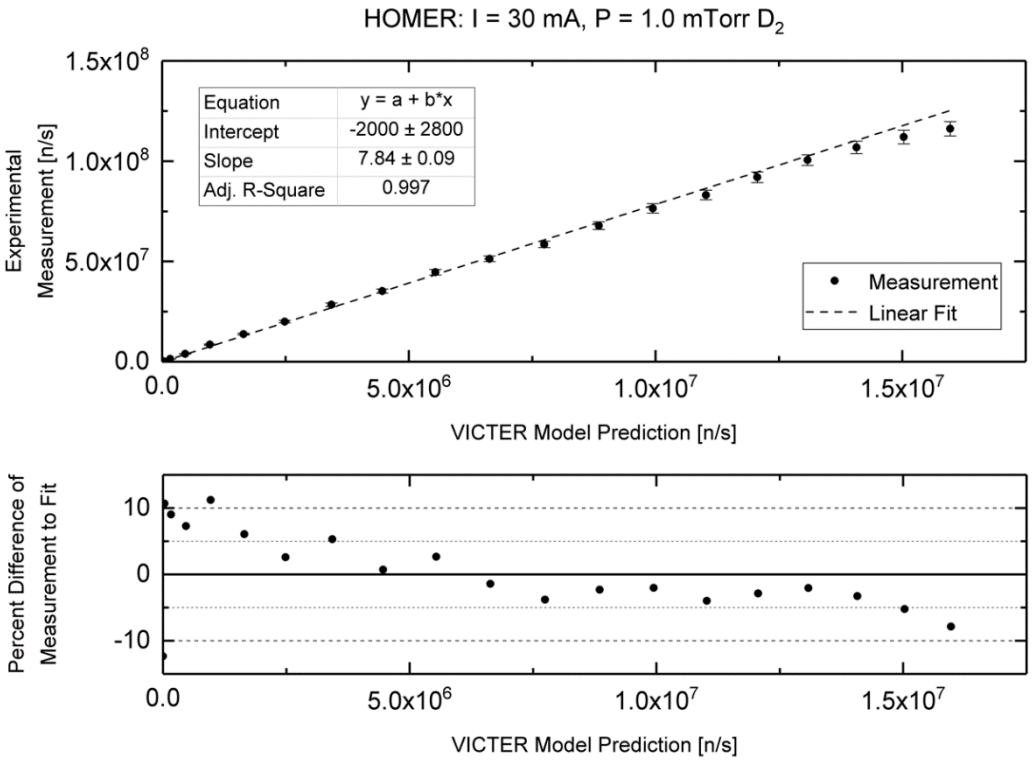

Figure 6-13: (Top) A linear least squares fit of the measured neutron production rate to the VICTER model prediction shows a factor of 7.84 discrepancy in the voltage parameter scan. (Bottom) A plot of the percent difference of measurement to the fit indicates this discrepancy in the model is not purely linear, and it is likely that unknown physical effects are unaccounted in the model.

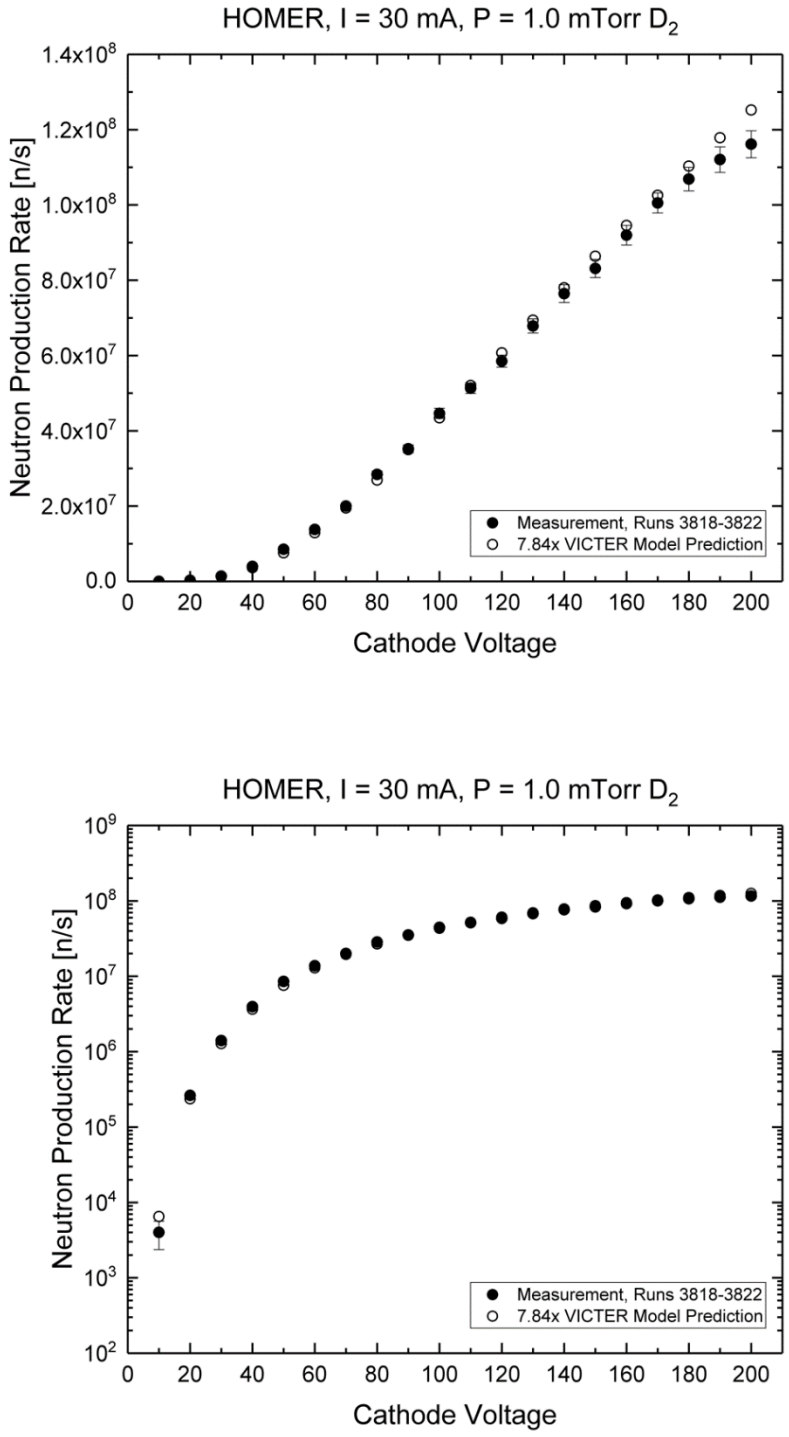

Figure 6-14: A plot of the VICTER model predicted voltage scan response scaled by a factor of 7.84 compared to the measured neutron production rate response for HOMER plotted linearly (top) and logrithmically (bottom).

There are phenomena that occur in the physical system which are not accounted for in the VICTER model, and these effects may increase or reduce the predicted neutron production rate. The presence of embedded fusion reactions originating from the chamber walls can contribute to the observable neutron production rate and may offset this discrepancy by some amount. Fast unconfined deuterium particles can stream outward from the device center and fuse with deuterium implanted into the wall increasing the neutron yield of the system. It is suspected that the contribution to the observable fusion reaction rate may be a significant effect, and a model to estimate the contribution of embedded fusion events is considered in Chapter 7. Reionization events involving fast neutral particles interacting with background gas are not represented in the VICTER model since the mean free path of these collisions is long compared to the cathode-anode distance, and the presence of such events would be considered a small effect. Additionally, elastic scattering events are not considered in the VICTER model which may have the effect of softening the ion energy spectrum, this additional softening of the deuterium ion energy spectrum would reduce the effective reaction cross section resulting in a decrease in neutron rates.

The discrepancy in the response curves at cathode voltages greater than 180 kV between the measurements and model may be due to unaccounted for electron emission processes at the cathode grid for elevated wire temperatures and ion energies as the system power is increased with voltage while maintaining a fixed cathode grid current. The diminishing gains of neutron production rate above 180 kV cathode voltages were observed in Figure 6-11 for both measurement sets taken at cathode current of 30 mA and chamber pressure of 1.0 mTorr D_2, indicating this rolling over may be systematic and not random. Enhanced electron emission from the cathode can occur as the substrate temperature is elevated by increasing the heat loading of the wires to the point where the grid begins to glow. Thermionic emission of electrons may occur at

these portions of the grid that experience high heat fluxes. Secondary electron coefficients will also increase with substrate temperature and energy of the ions impacting the grid, and both processes will displace the ion current in the system resulting in a reduced system efficiency and lower neutron production rate. During operation at higher power inputs, the grids in HOMER have been observed to glow, which may lead to the effects described above and has been experimentally observed elsewhere [6]. Additionally, the cathode grid transparency plays a role in determining the amount of recirculating ion current is removed from the system due to ion strikes with the grid wire, and this transparency may not be properly accounted for in the VICTER model. The effective ion transparency of the grid will differ from the geometric transparency due to the presence of microchannel formation in which electron jets streaming from the cathode region will preferentially ionize the background gas along the channel making the effective transparency harder to predict.

6.3 Summary

Parametric scans have been performed using the gridded IEC device HOMER to investigate the neutron production rate scaling with variations in the input cathode current, cathode voltage, and chamber pressure. Variations in the cathode current between 30 to 100 mA produced a linear response in neutron production rate indicating the fusion reaction regimes are most likely dominated by beam-background and beam-embedded collisions in this IEC device for cathode voltages ranging 170 to 200 kV at a 1.0 mTorr D_2 chamber pressure. A new steady state D-D neutron production rate record in an IEC device of 3.8×10^8 n/s has been measured for a cathode voltage of 200 kV, cathode current of 100 mA, and a chamber pressure at 1.0 mTorr D_2. An investigation into the device response with varying deuterium chamber pressure showed a less than

linear response when the pressure was increased over a range from 0.2 to 1.5 mTorr. This would indicate a strong dependence of the reacting deuterium energy and population with pressure, and the effect of energetic collisions with background gas reduces the energy distribution of fusing particles, decreasing the neutron yield. Variation of the cathode voltage showed the neutron production rate scaling is complex with an increase with voltage. The D-D neutron production rate performance in HOMER is observed to transition from a greater than linear response below 60 kV, a near linear response ranging 60 to 180 kV, and a less than linear response beyond 180 kV while operating at a cathode current of 30 mA and chamber pressure of 1.0 mTorr D_2. A comparison to the VICTER model prediction of the device performance shows the model under predicts the measured neutron production rate by nearly a factor of 8, and this discrepancy may be due to neutron producing processes not considered in the model.

6.4 References

[1] G. A. Emmert and J. F. Santarius, “Atomic and Molecular Effects on Spherically Convergent Ion Flow. I. Single Atomic Species,” *Phys. Plasmas*, vol. 17, no. 1, pp. 1–13, 2010.

[2] G. A. Emmert and J. F. Santarius, “Atomic and Molecular Effects on Spherically Convergent Ion Flow. II. Multiple Molecular Species,” *Phys. Plasmas*, vol. 17, no. 1, p. 13503, Jan. 2010.

[3] M. K. Michalak, “Increasing the High Voltage Capabilities and Exploring Parameter Space of an Inertial Electrostatic Confinement Fusion Neutron Source for the Detection of Chemical Explosives,” Ph.D. dissertation, University of Wisconsin-Madison, 2017.

[4] D. R. Boris, “Novel Diagnostic Approaches to Characterizing the Performance of the Wisconsin Intertial Electrostatic Confinement Plasma,” Ph.D. dissertation, University of Wisconsin-Madison, 2009.

[5] G. E. Becerra, “Neutral Particle Analysis in Inertial Electrostatic Confinement Fusion Devices,” Ph.D. dissertation, University of Wisconsin-Madison, 2014.

[6] G. H. Miley and S. K. Murali, *Inertial Electrostatic Confinement (IEC) Fusion*. New York, NY: Springer New York, 2014.

7. Effects of Impurity Gas and Embedded Fusion on the Neutron Production Rate Performance

This chapter examines the presence of long term trends in device performance by examining the results of replicate measurements of the neutron production rate for fixed experimental parameters taken at the start of each experimental run. Evidence of an increase in neutron production rate over the course of many runs was previously observed by Michalak [1], and this chapter will examine this drift in neutron production rate for the new data taken with the upgraded hardware for this work. Two effects were hypothesised to contribute to an upward drift in the neutron production rate over the device operation history during this data campaign: the presence of impurity background gas which may degrade neutron production rate and the contribution to the measured neutron production rate performance due to beam-embedded fusion in the chamber walls. The effect of impurity gas will be discussed in Section 7.2 and an embedded fusion model used to describe rate contributions is discussed in Section 7.3.

7.1 Results for replicate measurements of neutron production rate performance

A check of the system performance was conducted at the beginning of each run by operating the HOMER experiment at the same fixed set points to monitor for any changes or anomalies in the system. All startup data was performed by fixing the cathode current at 30 mA, the chamber pressure at 1.0 mTorr D_2, and measuring the neutron production rate for cathode voltages at 30, 80, 120, and 160 kV taken sequentially in that order. At each fixed voltage, about 30 seconds of counting data were collected. The measurements of the neutron production rate here represent only the data taken during the startup sequence of each run as described in Chapter 4,

and the experimental uncertainty of the measurements is determined using the method described previously in Chapter 6.

The results of these measurements are presented in Figure 7-1 to Figure 7-4, and show an upward trend in the neutron production rate for each set of fixed parameters taken at the start of each run. The first experimental run after the final cathode grid modification was Run 3746 performed on 01/05/2018, and the last experimental run presented here was Run 3845 performed on 2/16/2018. The data is presented with respect to the experiment date and to the run number to highlight distinguishing features. Looking at the data with respect to the run date (the top plots in Figure 7-1 to Figure 7-4), gaps in the data points represent dates during which no experimental data was taken. One consistent feature seen in all fixed voltage cases is that the measured neutron production rate is observed to drop after long durations of experimental downtime (order of days), and in subsequent runs, the measurements quickly return to the level of rates observed prior to this downtime. A second consistent feature of the data for all fixed cases is a distinct change of the rate performance increase, which is highlighted when the data is plotted by incrementing run number (bottom plots). This deflection in the rise of neutron rate seems to indicate a change in the system conditions has occurred and the overall upward rate of rate improvement is seen to change around Run 3785, which occurred on 1/30/2018. No notable changes to the experimental setup or counting system were made around this point in the campaign that would change the measurement response of the neutron production rate. It should be noted that all data collected for the experimental measurements used in the parameter study presented in Chapter 6 were performed after Run 3787, and these experimental measurements are taken in this more slowly varying portion of the curve.

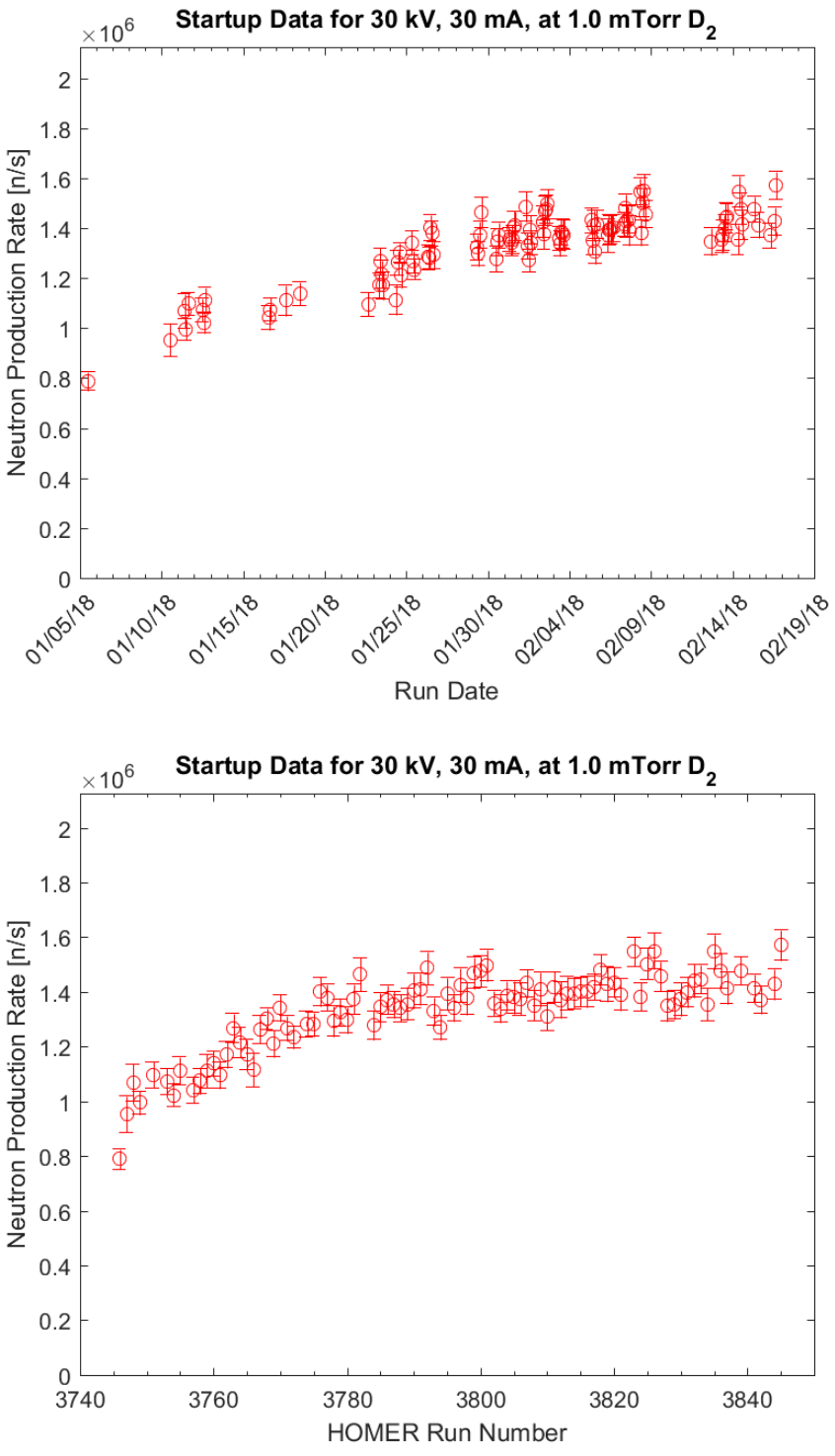

Figure 7-1: Startup neutron production rate measurements for cathode voltage 30 kV, cathode current of 30 mA, and chamber pressure of 1.0 mTorr D_2 plotted by run date (top) and by run number (bottom).

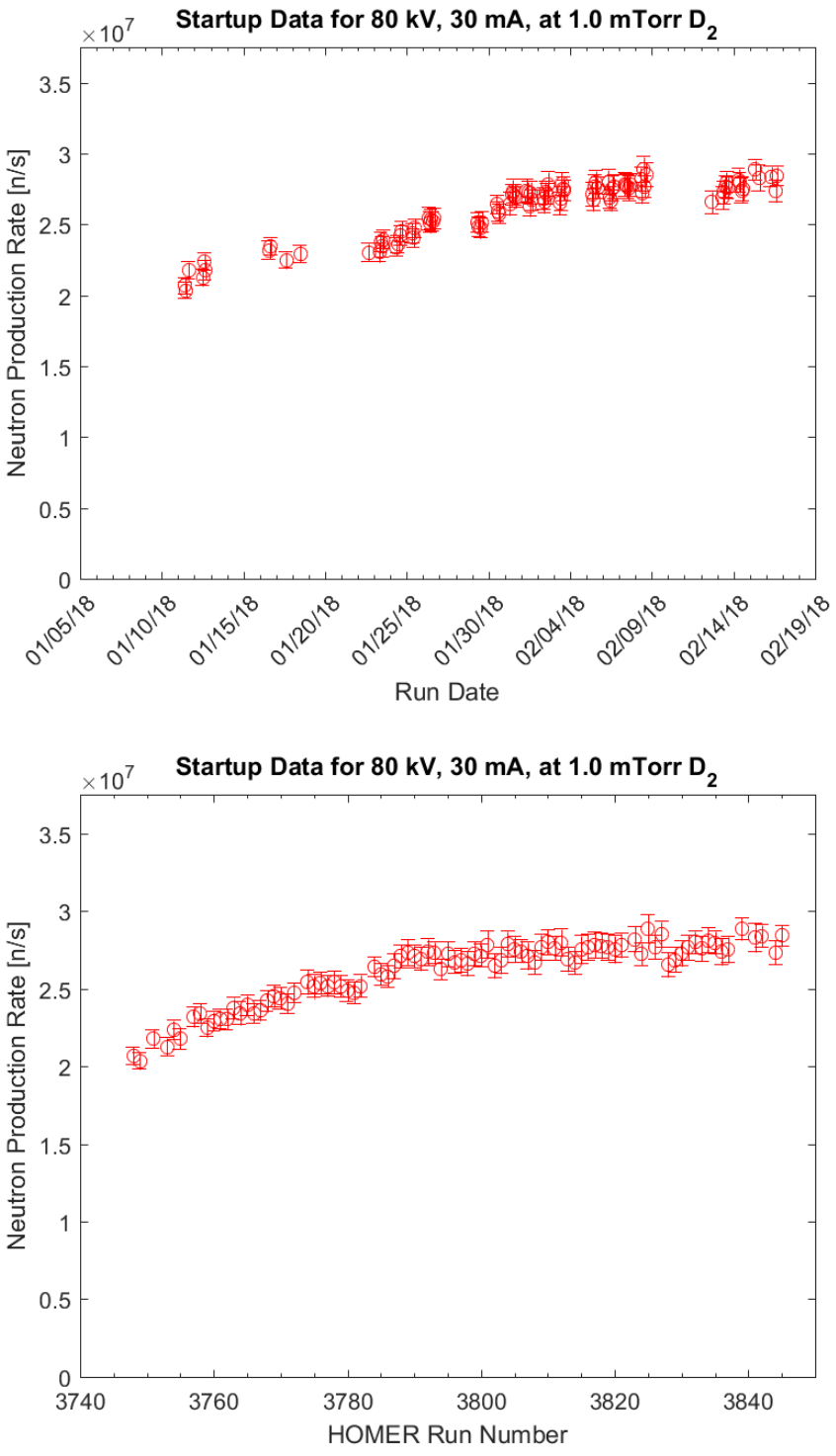

Figure 7-2: Startup neutron production rate measurements for cathode voltage 80 kV, cathode current of 30 mA, and chamber pressure of 1.0 mTorr D_2 plotted by run date (top) and by run number (bottom).

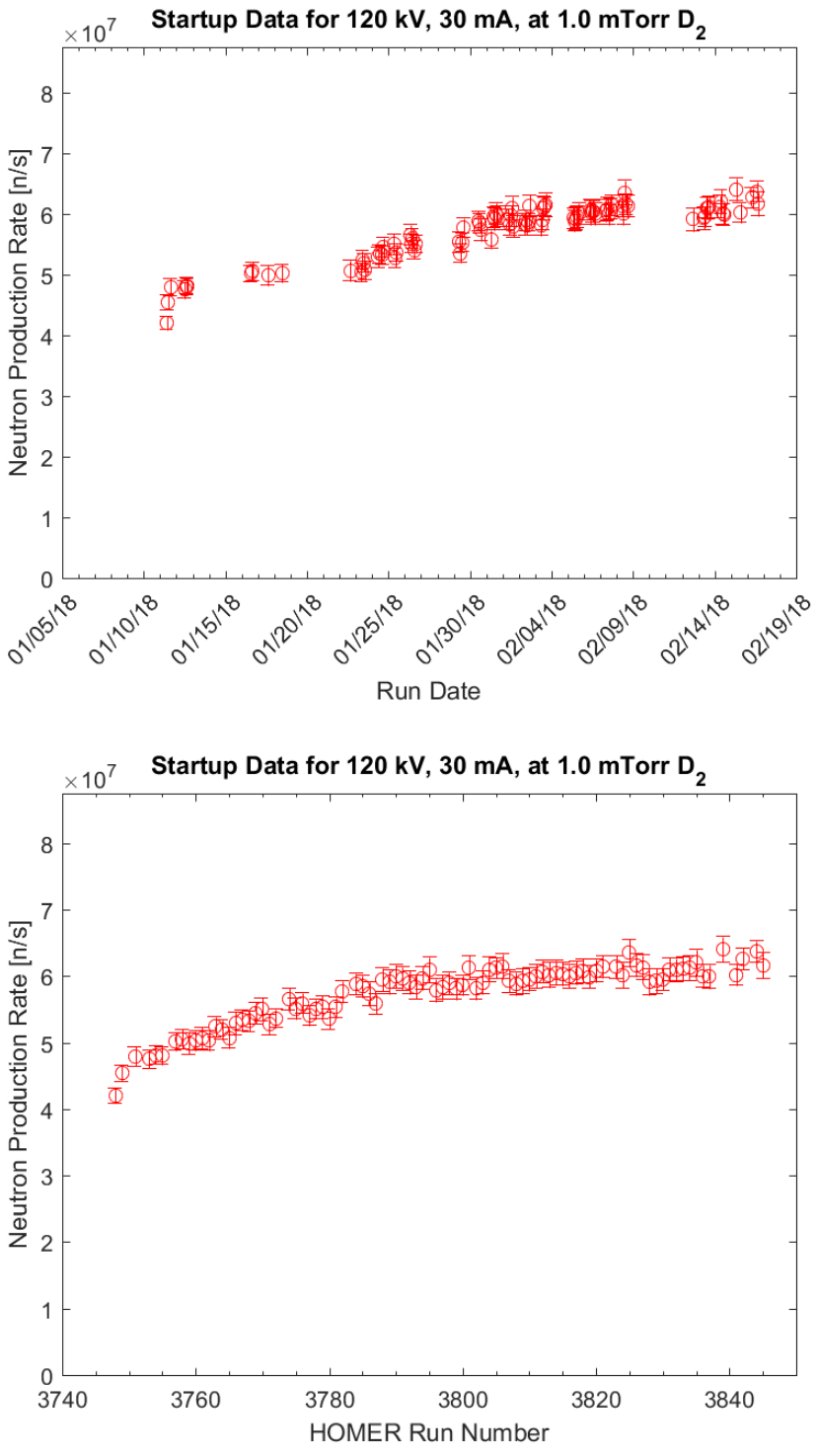

Figure 7-3: Startup neutron production rate measurements for cathode voltage 120 kV, cathode current of 30 mA, and chamber pressure of 1.0 mTorr D_2 plotted by run date (top) and by run number (bottom).

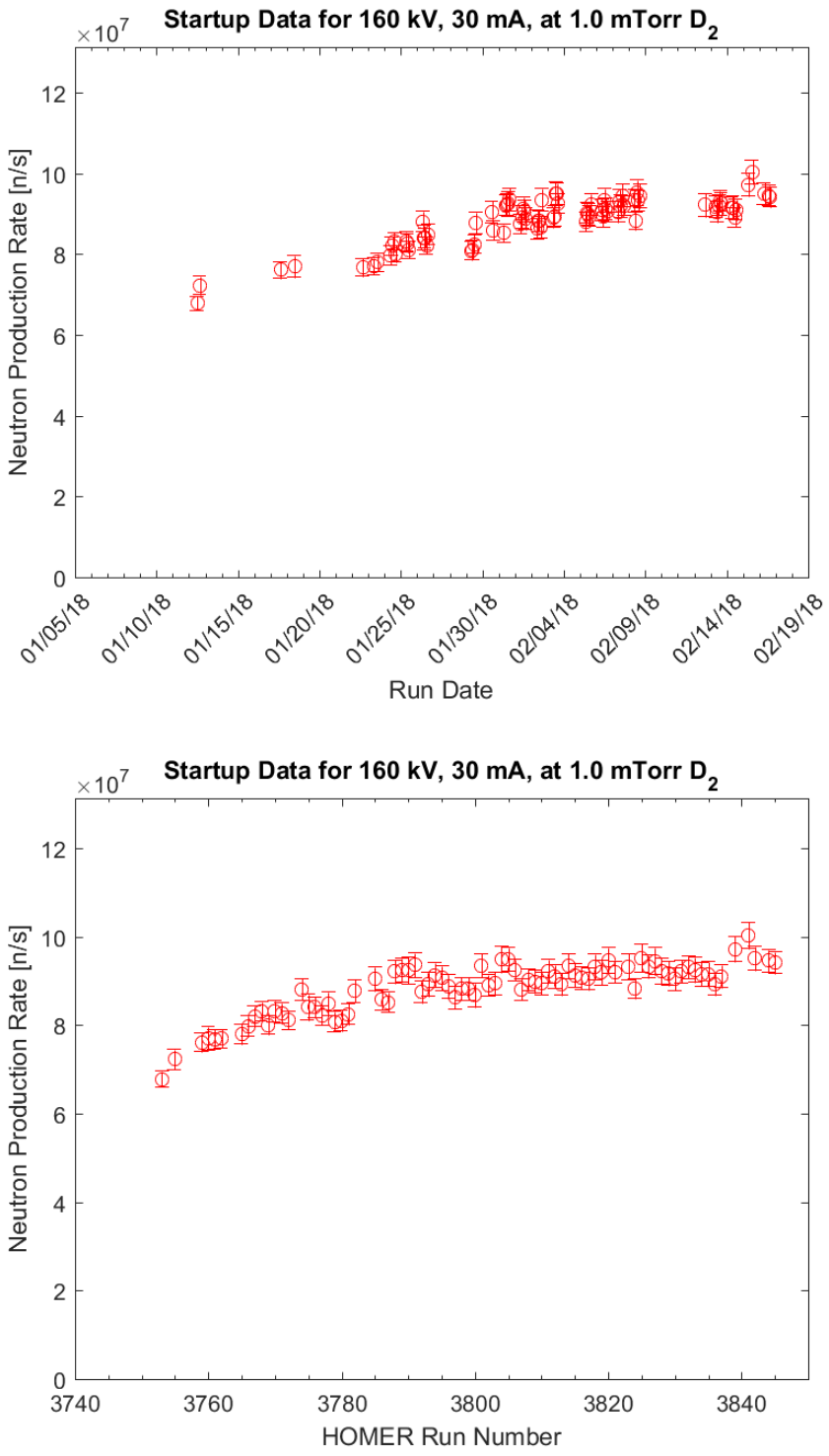

Figure 7-4: Startup neutron production rate measurements for cathode voltage 160 kV, cathode current of 30 mA, and chamber pressure of 1.0 mTorr D_2 plotted by run date (top) and by run number (bottom).

7.2 Discussion of the impurity effect on neutron production rate performance

The presence of impurity gas in the system will have a negative impact on the neutron production rate performance of an IEC device due to several effects. First, the energetic collisions of non-fusing deuterium species do not contribute to D-D neutron production and may redistribute ion energy by dissociative or charge exchange reactions. Secondly, impurity ions may be confined by the potential well, contributing to the system ion current and striking the cathode grid wire, which reduces the fraction of deuterium ions contributing to the meter current. The ion current contribution, I_{ion}, to the cathode is represented by the contribution of the sum of deuterium species, I_D, and sum of impurity species, I_I.

$$I_{ion} = \Sigma I_{D_i} + \Sigma I_{I_i} \qquad 7\text{-}1$$

The cathode meter current, $I_{cathode}$, measured by the system will be the contribution of both the ions impacting the cathode grid and stalk surfaces, and the secondary electrons leaving the cathode, I_{e^-}.

$$I_{cathode} = I_{ion} + I_{e^-} \qquad 7\text{-}2$$

Electron current contributions are due to the emission of secondary electrons from the impact of ions at the cathode surface, neglecting contributions from field emission, photoemission, and thermionic emission electrons. The electron contribution to the cathode current due to ions striking the grid is related by the secondary electron coefficient, γ, summed over all ion species:

$$I_{e^-} = \Sigma\gamma_i I_i = \Sigma\gamma_{D_i} I_{D_i} + \Sigma\gamma_{I_i} I_{I_i} \quad 7\text{-}3$$

Combining these equations, the cathode current is related to the ion species which may impact the grid:

$$I_{cathode} = \Sigma(1+\gamma_{D_i}) I_{D_i} + \Sigma(1+\gamma_{I_i}) I_{I_i} \quad 7\text{-}4$$

For a fixed cathode current, the deuterium ion current will decrease as the impurity levels increase. Since current from the deuterium and impurity species are weighted by their secondary electron coefficients, the presence of heavier mass impurities will have a stronger effect due to their higher secondary coefficients compared to lighter deuterium species. The presence of impurities will have the effect of reducing the measurable neutron production rate by displacing the fusible deuterium ion contributions in the system. Impurities due to outgassing from material surfaces and the vacuum chamber leak rate are likely the largest contributing sources for HOMER. A typical system base pressure of $4\text{x}10^{-7}$ Torr is achieved.

A test demonstrating the impact of impurity gas in the system was performed in an earlier experiment by measuring the neutron production rate for similar deuterium flow rates with impurity gasses added. In this test, the deuterium flow rate is fixed, resulting in a chamber background pressure near 0.26 mTorr. The chamber pressure is then raised by the introduction of impurities to the chamber by outgassing via heating the chamber walls or by a controlled air leak. Figure 7-5 shows the result from three different cases of system response: fixed deuterium flow rate only, a fixed deuterium flow rate plus a calibrated air leak, and a fixed deuterium flow rate with outgassing contributions from heating the chamber walls. For this test, a thermocouple probe is mounted to the outside wall of the aluminum HOMER chamber to monitor changes in

temperature. The measurements of the neutron production rate for the outgassing case were taken over several points in time as the chamber pressure increased with increasing outside chamber wall temperature from 27 to 56 ºC for fixed deuterium flow rate and vacuum pumping conditions. The controlled air leak and the deuterium only cases were taken with an outside chamber wall temperature of 27 ºC. A similar drop in neutron production rate performance by about a factor of 3 was observed as the chamber pressure increased 60-80% above the fixed deuterium pressure in both the outgassing and air leak cases, which indicates both sources of impurities have similar effects in reducing the neutron production rate.

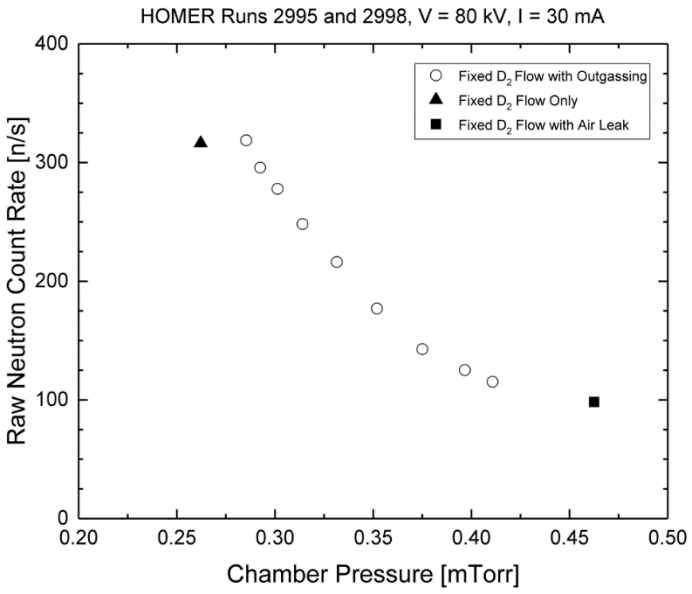

Figure 7-5: For similar deuterium flow rates, the neutron production rate is seen to decrease due to the introduction of impurities into the system by chamber outgassing or by an air leak.

The effects of outgassing will probably be reduced in HOMER after many conditioning runs have been performed, where the system has been allowed to heat and cool over several run cycles. The system neutron production rate was measured while fixing the cathode voltage to 120 kV, cathode current to 60 mA, and chamber pressure to 1.0 mTorr D_2 and allowing the chamber wall to heat up over 5 minutes of run time. Figure 7-6 shows the neutron production rate does not drastically decrease while the chamber wall temperature is increased from 42 to 73 ºC. Additionally, a small rise in pressure of 0.75% over 1.029 mTorr was measured as the chamber wall heated. This pressure increase may be due to a rise in gas temperature for a fixed volume by the ideal gas law; however, measurements of the background neutral gas temperature are not available for comparison. Additionally, outgassing of impurities into the chamber may also contribute a small amount to this pressure rise.

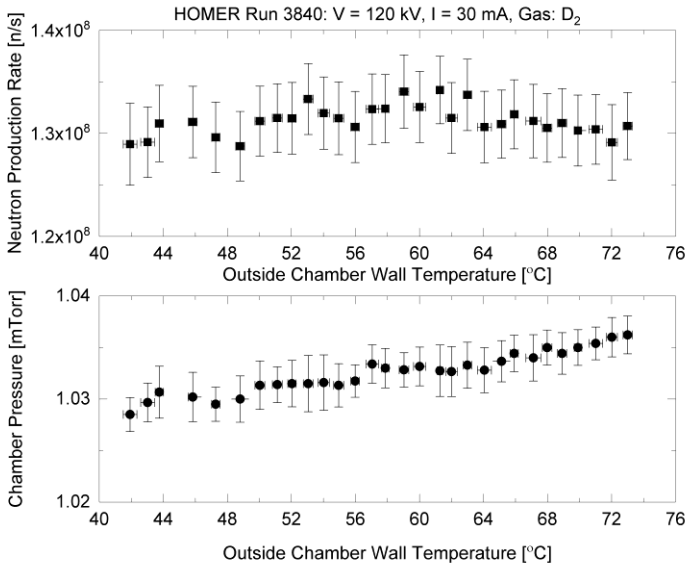

Figure 7-6: Effects of outgassing due to chamber wall heating are minimized in HOMER for a well-conditioned system. The neutron production rate is not seen to drastically change as the chamber is heated from 42 to 73 ºC, where a 0.75% rise in chamber pressure from 1.029 mTorr D_2 is observed.

Large errors in the deuterium chamber pressure set point may affect the neutron production rate output for repeated startup measurements, and sensitivity of the neutron rate is examined for the 160 kV startup data in Figure 7-7. The startup data presented in Figure 7-4 is analyzed by plotting the neutron rate with the spread in the chamber pressure set points, and the color mapping represents the run order. The conditioning data points taken from Runs 3759-3787 are seen to generally underperform for similar pressures of about 1.025 mTorr when compared to later data taken between Runs 3788-3842. A linear regression of the data for Runs 3788-3842 was analyzed by a one-way analysis of the variance (ANOVA), which tests if the neutron production rate measurements over this range of chamber pressure set points has a slope that is statistically different from zero. The result of the ANOVA test found the slope of the neutron production rate over this range is not significantly different from zero with an F Value = 1.17 and p = 0.29; this indicates the system response is insensitive to the small variations in the chamber pressure set point for these measurements. The neutron rate performance difference between the earlier and later runs in the series indicate that some other uncontrolled parameter may be responsible for a drift in neutron production rate performance. It is believed that these earlier runs in the data set (Runs 3759-3787) may have been affected by the presence of outgassing impurities during the initial conditioning process of the system after the previous up to air maintenance and installation of the modified cathode was performed.

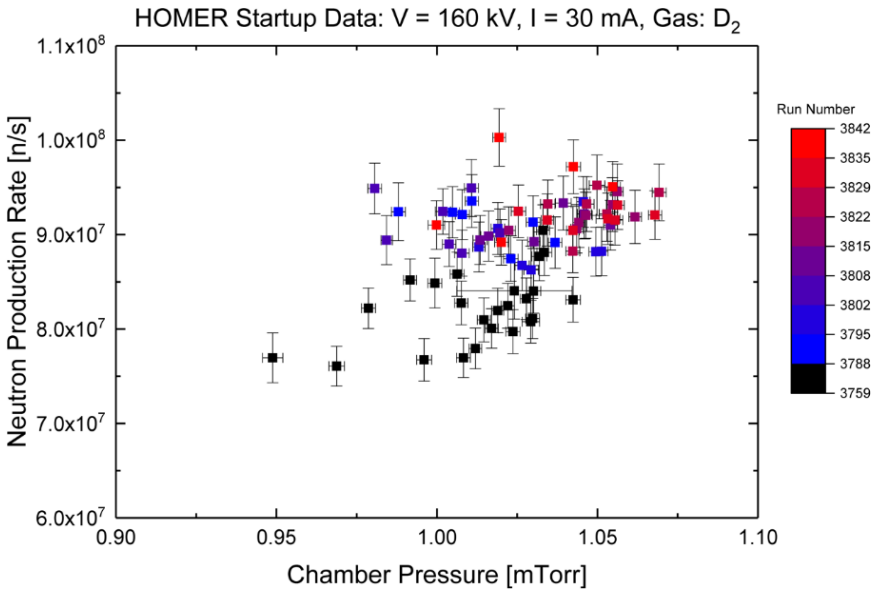

Figure 7-7: Neutron production rate plotted with the spread in chamber pressure measurements for HOMER startup data at a cathode voltage of 160 kV and cathode current of 30 mA. Runs 3788-3842 show the neutron production rate response is insensitive to variations in the pressure set point measurements ranging 0.975 to 1.075 mTorr, and Runs 3759-3787 represent data taken during initial conditioning of the system.

To examine the system for the presence of impurities, residual gas analysis (RGA) spectra are taken during operation using a quadrupole mass analyzer. The RGA data contains information related to gas present in the system, filtering by the mass to charge ratio of ionized background gas. Different sensitivities due to the ionization cross sections of the background gas species make the RGA spectral response difficult to interpret for absolute partial pressure measurements, and differential pumping on the hardware may bias the gas distribution observed at the RGA instrument. Qualitative comparisons may be made by examining the relative characteristics of the spectra under similar operating parameters. Select runs, highlighted in Figure 7-8, are chosen for analysis to compare the distribution of gas species during the collection of the 160 kV start up data.

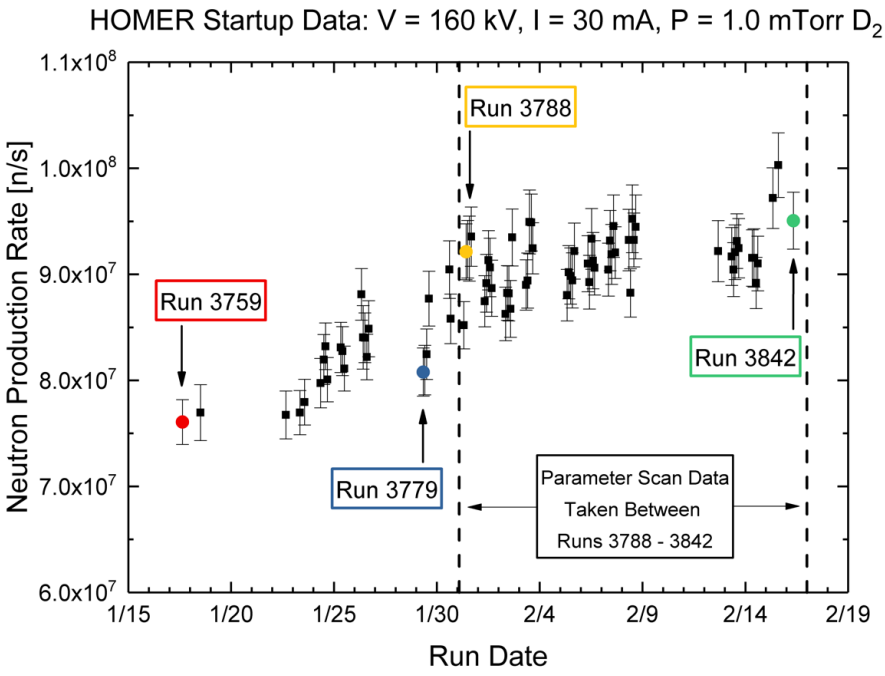

Figure 7-8: RGA data is taken for analysis from select runs to examine the chamber conditions during the measurements taken during the startup procedure at cathode voltage 160 kV, cathode current 30 mA, chamber pressure 1.0 mTorr D_2.

A comparison of the RGA spectra is shown in Figure 7-9 for the four runs highlighted above, and the RGA spectra in each instance is captured during the measurement of the neutron production rate where a 1.0 mTorr chamber pressure is maintained. To compare the relative intensities of the impurity masses, each spectrum is normalized to the dominant amu/e 4 peak after subtracting off the spectrum background noise floor. The result of the RGA scans show a dominating presence of peaks 1-6 in the system and smaller relative intensities of peaks greater than 6 amu/e. In this figure, the relative intensities for peaks > 6 amu/e are generally observed to decrease as the number of runs progresses and the relative intensity at peaks at 1, 2, 3, and 5 amu/e are observed to drop slightly as well.

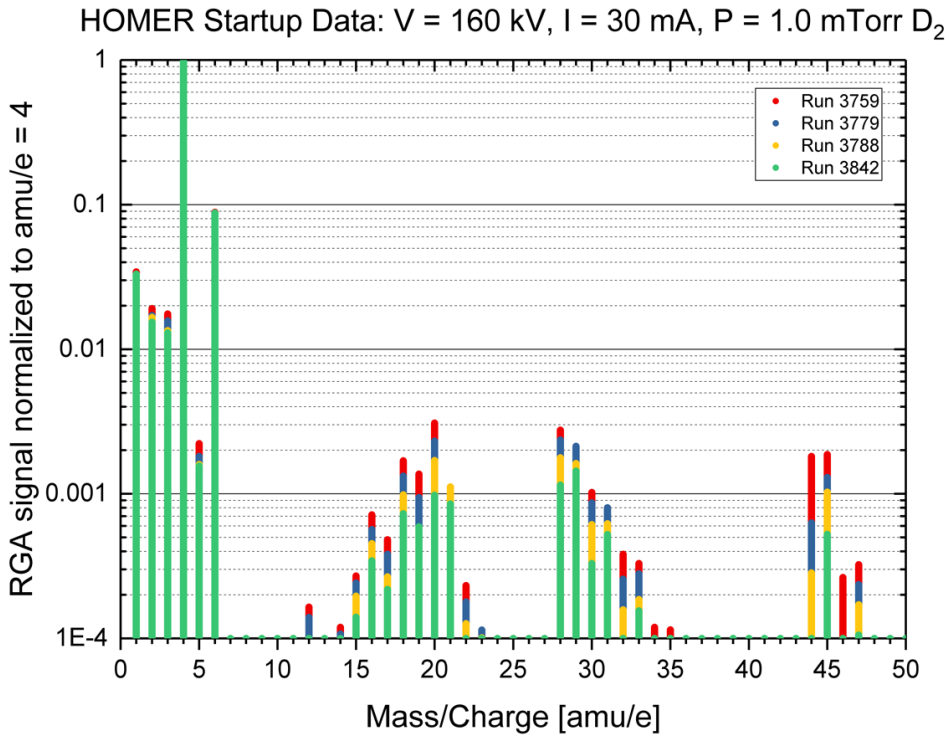

Figure 7-9: A comparison of the relative RGA spectra to the shows a reduction in impurity levels over the course of several runs. Each RGA spectrum is baseline corrected for noise then normalized by the amu/e = 4 peak which represents D_2 in the system.

The peaks at 1-6 represent the presence of deuterium and hydrogen molecular species, and to a lesser extent helium, and Table 7-1 gives the most likely contributions of these species to the spectrum response. The contribution of tritium or helium-3 to the background gas population from deuterium fusion reaction products are assumed negligible since a background gas density at 1 mTorr is ~10^{19} m^{-3} and fusion rates of ~10^{8} reactions/second are only sustained for minutes at a time while the chamber gas is constantly pumped on in the open flow system for a chamber volume ~0.5 m^3.

Table 7-1: Light mass gas species most likely to contribute to the RGA spectrum for 1-6 amu/e.

amu/e	Species
1	H^+
2	D^+, H_2^+
3	H_3^+, DH^+
4	D_2^+, DH_2^+, He^+
5	HD_2^+
6	D_3^+

IEC operations using electron impact ionization to drive the ion source plasma region (outside the anode grid) will result in the formation of D^+, D_2^+, and D_3^+, and the formation of mixed hydrogen-deuterium ion species to the extent that hydrogen exists in the system. Proton exchange reactions due to singly ionized diatomic species colliding with a diatomic background neutral may produce triatomic ions:

$$H_2^+ + H_2 \rightarrow H_3^+ + H \qquad 7\text{-}5$$

This exchange reaction may also occur for deuterium species [2], and similar reactions are likely to be observed by the RGA ionizer of the background gas since the instrument also uses electron impact to ionize the background gas. A deuterium gas purity level of 99.999% is used for all experimental measurements in this work, and the presence of helium impurities are expected to have a negligible contribution to the 4 amu/e peak while the chamber pressure is maintained at 1.0 mTorr using deuterium gas.

The contribution to the RGA spectrum for mass/charge ratios greater than 6 amu/e are due to higher mass impurities found in the background gas of the system, and Table 7-2 gives a list of suspected contaminants in the system and the most predominantly observed mass/charge fractions.

Contaminants in the system are most likely due to a small air leak or outgassing from elastomer seals and the blue nylon high voltage insulator; the use of ethanol and methanol in the cleaning process of the elastomers and nylon may have also led to an absorbed quantity of the alcohols which may contribute to the outgassing load. Without careful instrument sensitivity calibration and accounting for the gas species biasing due to the differential pumping, the absolute impurity fraction is not determined for this system using the RGA. With a deuterium chamber fill pressure of nearly four orders of magnitude greater than the chamber base pressure, the total impurity fraction is most likely under 0.1% contribution to the background gas. For a fixed chamber fill pressure of 1.0 mTorr D_2, the RGA data in Figure 7-9 shows a decrease in relative intensities of these higher mass species which would indicate a removal of impurities as the chamber is cycled through many runs while keeping the system under constant vacuum. The reduction of impurity gas would have a positive increase on the neutron production rate performance under similar operating conditions due to a larger portion of deuterium species contributing to the ion current.

Table 7-2: Table of mass/charge spectrum for most likely contaminants present in the HOMER vacuum chamber due to atmospheric constituents and common solvents used [3].

Species	Most Common Mass Peaks Observed (amu/e)				
N_2	28	14	29		
O_2	32	16			
Ar	40	20	36	38	
CO_2	44	28	16	12	
Ne	20				
He	4				
Methane	16	15	14	13	12
Water	18	17	16	19	20
Ethanol	31	45	29	27	46
Methanol	31	32	29	15	

7.3 Discussion of embedded fusion contributions to the neutron production rate

The increase in neutron production rate observed over periods of several runs for similar fixed experimental parameters may be due to an increasing amount of embedded fusion reactions occurring with an increasing rate of deuterium density in the wall over many experimental runs. Unconfined energetic neutral and negative ion deuterium particles are formed during the operation of an IEC device, and these fast deuterium particles can collide with other deuterium particles embedded in the chamber wall, which can result in a neutron producing fusion reaction. Under normal operating conditions, these unconfined energetic deuterium particles will embed in the wall, leading to an accumulation of deuterium near the chamber inner surface. The rate of deuterium accumulation in the wall will depend on the incident deuterium particle current and the rate of deuterium diffusion out of the wall, and the deuterium density profile in the wall will be primarily the result of the stopping range of the energetic deuterium in the chamber wall and the diffusion of deuterium. The deuterium particle current and energy distribution into the chamber wall is dependent on the operational parameters of the IEC device, and the VICTER model may be used to predict the incident particle current and average energy for specified operational parameters. With this information, an order of magnitude estimate of the neutron production rate due to fusion reactions occurring within the chamber wall is made, and the upward trend in neutron production rate is examined by estimating the rate of increase in deuterium density in the wall.

The following embedded fusion analysis considers the increase in rates observed during the repeated 160 kV measurements and aims to determine if the increasing rate of neutron production may be reasonably accounted for by considering deuterium density buildup in the chamber walls over a set of experimental runs. This estimate is performed by the following method:

- Calculate the range of the typical incident deuterium travelling through aluminum using the continuous slowing down approximation (CSDA).
- Estimate the deuterium particle flux incident on the walls using the VICTER model for typical experimental operating conditions.
- Calculate the neutron production rate due to embedded fusion reactions from the energetic deuterium particle current colliding with a background deuterium density in the aluminum wall as the deuterium slows down in the substrate.
- Calculate the increase in deuterium density needed to match the observed rate of neutron production increased over the set of fixed parameter measurements.
- Compare this deuterium density matching condition to the estimated amount of deuterium implanted into the chamber wall during experimental operations over the set of runs.

If the increase in deuterium density in the aluminum wall needed to match the experimentally measured increase in neutron production rate is similar or less than the estimated increase in deuterium density due to implanted deuterium during experimental operations over the

set of runs, then it is considered plausible that the observed rate of neutron production increase is due to embedded fusion reactions in the chamber wall.

To calculate the total distance travelled by the deuterium slowing down in the aluminum chamber wall, the continuous slowing down approximation is used for the energetic deuterium ions. Previous work [4] has shown the average energy spectrum of the incident deuterium at the wall is typically in the range of 20 to 30 keV due to the elevated charge exchange cross section within this energy range. The CSDA ranges calculated for energetic deuterium in aluminum are given in Table 7-3.

Table 7-3: CSDA range in aluminum for incident deuterium energies ranging 20 to 30 keV.

Energy [keV]	CSDA Range (μm)
20	0.33
22	0.35
24	0.38
26	0.40
28	0.42
30	0.44

The case of deuterium energy of 26 keV with a range of 0.4 μm is chosen as a base case for the rest of the analysis, and a plot of the incident deuterium energy with distance travelled in aluminum is plotted in Figure 7-10.

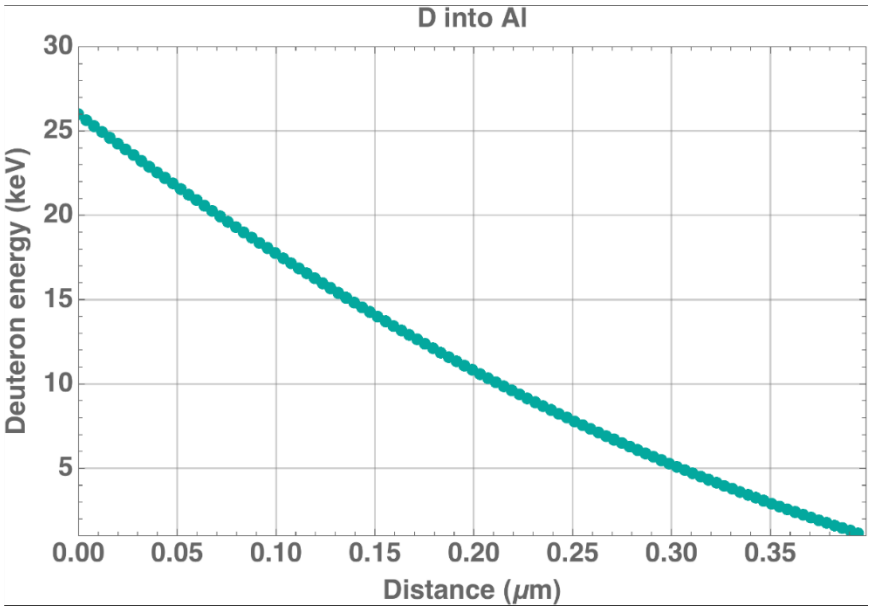

Figure 7-10: Deuterium ion energy as a function of distance travelled in aluminum.

The VICTER model is used to estimate the number of neutral deuterium particles hitting the wall for both atomic and molecular species, and the input to the model used for this comparison was: 100 kV cathode voltage, 30 mA cathode current, 1.0 mTorr D_2 chamber pressure, 20 cm diameter cathode radius, 50 cm diameter anode, and 90 cm diameter spherical chamber wall. The model neglects the contribution of fast negative ions reaching the wall; however, the negative deuterium ion contribution is believed to be a small contribution of ~5% of the ion current based on previous observations [2]. Under these operating conditions, VICTER predicts a total deuterium

particle current of $5x10^{17}$ deuterium/s incident on the chamber wall, and a deuterium particle flux at the chamber wall is ~$2x10^{17}$ D/m^2-s.

The fusion rate contribution due to this incident fast deuterium on the chamber surface will depend on the incident deuterium energy and particle flux, along with the embedded deuterium density and depth profile in the aluminum. Half of the fusion reactions resulting from a fast deuterium ion colliding with a stationary embedded deuterium particle (beam-embedded) will result in neutron production and contribute to the measurement. The energy attenuation of the fast deuterium ions is proportional to the stopping power in aluminum and folds into the energy dependent fusion cross section for this calculation. An average incident deuterium energy of 26 keV is used for the purposes of this calculation with an incident deuterium particle flux of $2x10^{17}$ D/m^2-s. An initial estimated deuterium density of ~10^{25} m^{-3} in aluminum is arbitrarily assumed, which is about 0.017% aluminum atomic density. The actual density profile of deuterium in the wall is unknown, and several cases are examined here for Gaussian profiles with a specified mean, μ, and width, σ, in addition to a flat density profile. Since the incident deuterium energy will typically range from 20-30 keV, resulting in a CSDA range ~0.4 μm, peaked Gaussian profiles centered about a 0.4 μm depth with varying widths and a flat density profile are chosen for analysis, and the density profiles used are shown in Figure 7-11. A broadened density profile away from the mean implantation depth is likely since the real energy spectrum of incident deuterium particles is expected to be broader, and diffusion of the deuterium is expected to occur as the chamber wall is heated beyond 340 K [5]. For these calculations, each profile has been normalized such that an equal number of embedded deuterium atoms is represented over a depth of 4 μm.

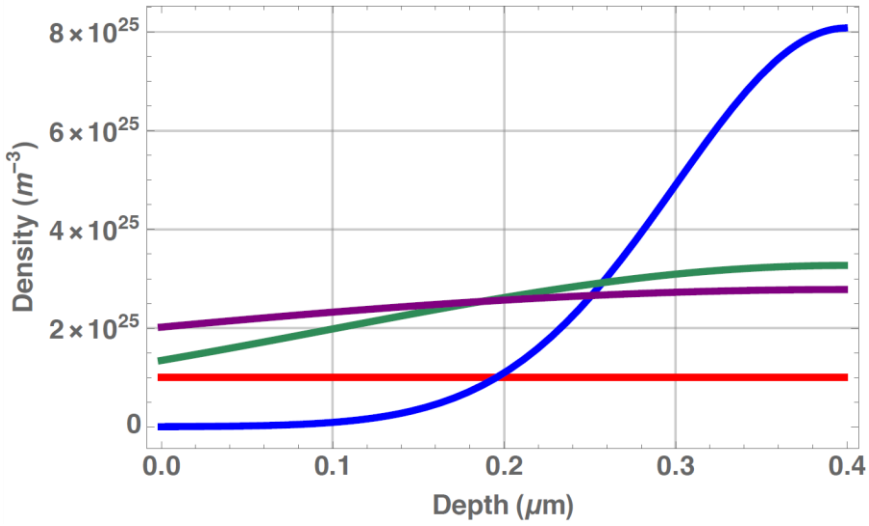

Figure 7-11: Simulated deuterium density profiles in the aluminum chamber wall for several Gaussian parameters: [blue: μ = 0.4 μm, σ = 0.1 μm], [green: μ = 0.4 μm, σ = 0.3 μm], [purple: μ = 0.4 μm, σ = 0.5 μm], [red: flat density profile].

The neutron production rate due to the embedded reactions contribution is then calculated by integrating the product of deuterium flux, fusion cross section, and density profile over the CSDA range. The total simulated neutron production rate contributions for each case are reported in Table 7-4, and the cumulative and differential neutron rate contributions with depth are shown respectively in Figure 7-12 and Figure 7-13.

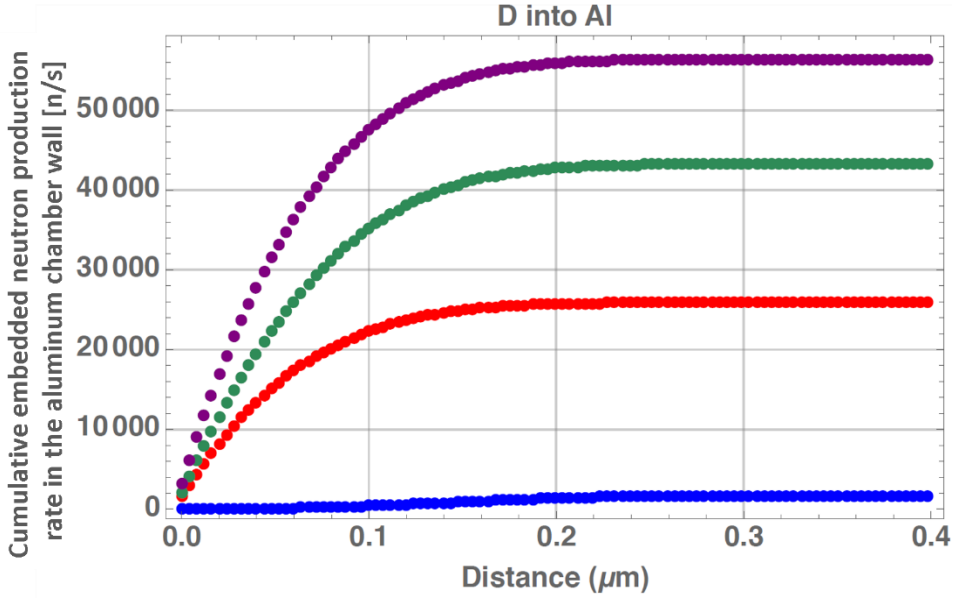

Figure 7-12: Cumulative embedded neutron production rate with depth for several Gaussian density profiles: [blue: μ = 0.4 μm, σ = 0.1 μm], [green: μ = 0.4 μm, σ = 0.3 μm], [purple: μ = 0.4 μm, σ = 0.5 μm], [red: flat density profile].

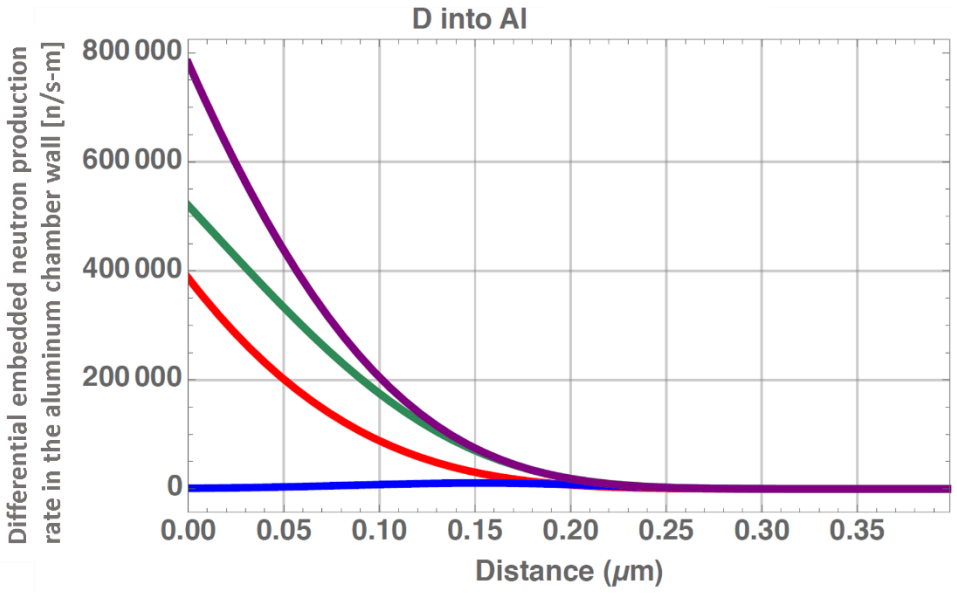

Figure 7-13: Differential embedded neutron production rate contribution with depth in aluminum for several cases shows most all fusion events occur within the first 0.2 μm depth for all simulated Gaussian profiles: [blue: μ = 0.4 μm, σ = 0.1 μm], [green: μ = 0.4 μm, σ = 0.3 μm], [purple: μ = 0.4 μm, σ = 0.5 μm], [red: flat density profile].

Table 7-4: Simulated total neutron production rate contribution of embedded fusion reactions in the wall for different deuterium density profiles assuming ~ 0.017% deuterium atomic fraction in aluminum.

Deuterium density profile	Neutron Production Rate [n/s]
Gaussian: μ = 0.4 μm, σ = 0.1 μm	0.2×10^4
Gaussian: μ = 0.4 μm, σ = 0.3 μm	4.2×10^4
Gaussian: μ = 0.4 μm, σ = 0.5 μm	5.5×10^4
Flat Profile	2.5×10^4

The embedded fusion reaction rate contribution becomes negligible beyond a depth of 0.2 μm for all cases where the deuterium ion energy is attenuated below ~10 keV as it moves through the substrate and the fusion cross section drops rapidly. Averaging the neutron rates from these different cases gives an estimated neutron production rate of $\sim 3 \times 10^4$ n/s due to embedded fusion.

To estimate the increase in the neutron production rate, a linear fit is applied to the measured rates for Runs 3788 to 3842 for the 160 kV cathode voltage case, shown in Figure 7-14. The increase in measured neutron production rate over this range is then calculated by the difference in fit of the rate from Run 3788 to Run 3842. For cathode voltage of 160 kV, cathode current of 30 mA, and chamber pressure of 1.0 mTorr D_2, the increase in the neutron production rate by linear fit is $(3.8 \pm 1.2) \times 10^6$ n/s from Runs 3788 to 3842, which represents about 4% of the average neutron production rate of 9.2×10^7 n/s over this range. This analysis was repeated for the 30, 80, and 120 kV cathode voltage cases, and the increase in neutron production rate calculated from the linear fit of the data is presented in Table 7-5.

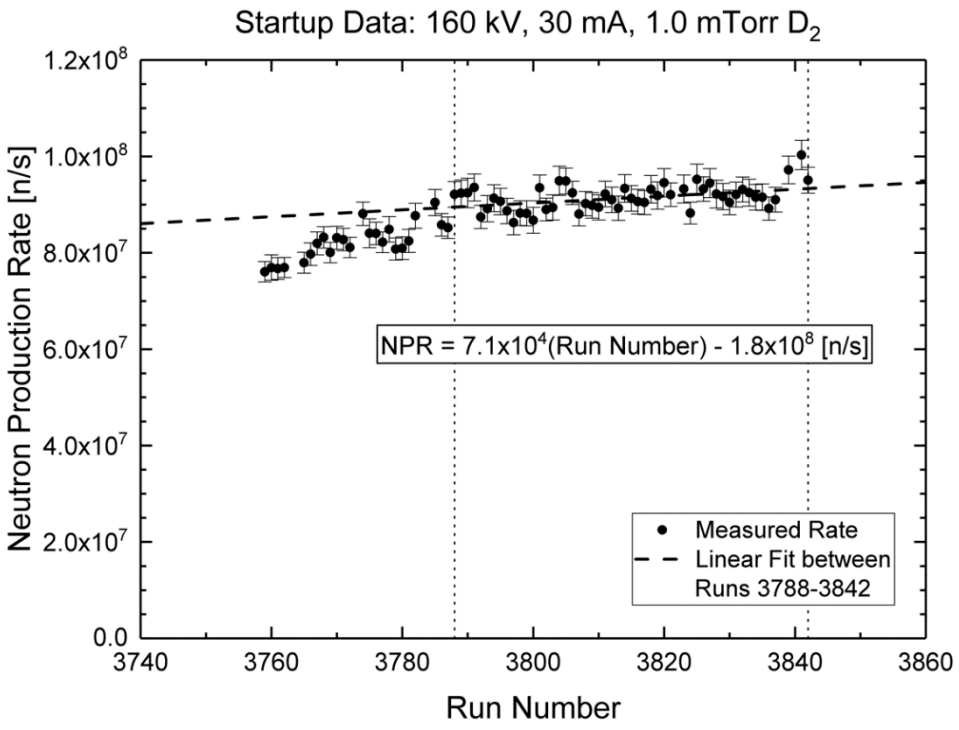

Figure 7-14: A linear fit of the neutron production rate measurements is taken from Run 3788 to 3842 for fixed operating set points of cathode voltage of 160 kV, cathode current of 30 mA, and chamber pressure of 1.0 mTorr D_2. The slope of the fit indicates a rise in neutron production rate after several runs are performed.

Table 7-5: Increase in neutron production rates from Runs 3788 to 3842 determined by a linear fit of the measurements for different cathode voltage setpoints and a fixed cathode current of 30 mA and chamber pressure 1.0 mTorr D_2.

Cathode Voltage [kV]	Increase in Neutron Production Rate [n/s]
30	$(7.2 \pm 2.8)\text{x}10^4$
80	$(1.2 \pm 0.2)\text{x}10^6$
120	$(2.6 \pm 0.5)\text{x}10^6$
160	$(3.8 \pm 1.2)\text{x}10^6$

Since the embedded fusion rate scales linearly with the deuterium density in the wall, a comparison may be made to the change in neutron rate to estimate the density increase needed to match this upward trend in measured rate. The change in neutron production rate, $\Delta NPR_{obesrved}$, with respect to the initial neutron rate predicted from embedded fusion calculation, $NPR_{embedded}$, should scale as the change in the deuterium density, Δn_D, with respect to the deuterium density in the wall, n_{D_o} :

$$\frac{\Delta n_D}{n_{D_o}} \sim \frac{\Delta NPR_{obesrved}}{NPR_{embedded}} \rightarrow \Delta n_D \sim \frac{\Delta NPR_{obesrved}}{NPR_{embedded}} n_{D_o} \qquad 7\text{-}6$$

Using an assumed deuterium density ~10^{25} m^{-3} in the aluminum wall, the predicted neutron rate averaged over the embedded fusion cases of 3x10^4 n/s, and the observed upward trend in neutron production rate for the 160 kV cases is ~4 x10^6 n/s, so the increase in deuterium density needed to match the production increase would be ~1.3x10^{27} m^{-3}. This change in deuterium density to match this neutron production rate represents ~2% the atomic density of the deuterium in aluminum.

To estimate the total incident deuterium particles on the wall that had occurred over these runs, the time integrated particle current incident on the wall is calculated over the device operational history within this run span. The device operation time under plasma conditions during these runs is summed up for all voltage and current conditions, and the total time is calculated to be ~5x10^4 seconds. The external chamber wall temperature was recorded at maximum 78 ºC (351 K), and the time weighted average temperature over these runs was 39 ºC (312 K). The product of the cathode current and operation time integrated over the set of runs was calculated to be 1.5x10^6 mA-s, and the product of the cathode voltage, cathode current, and run duration integrated over these runs was calculated to be 2x10^8 kV-mA-s. To bracket the total amount

deuterium particles embedded into the wall over this run duration, the minimum is approximated as this time integrated cathode current converted to particle current by the coulomb charge: ~$9x10^{21}$ deuterium atoms, and the maximum is approximated by weighting the integrated product of cathode voltage, cathode current, and run duration by the average neutral deuterium energy of 26 keV to give: ~$5x10^{22}$ deuterium atoms. This weighting represents an estimate of the number of neutral particles escaping the system per each full cathode voltage energy ions entering from the source region. If an assumption is made that these implanted deuterium ions are uniformly distributed up to their range depth in the aluminum wall, then the [minimum, maximum] estimated increase in deuterium density over this set of runs would be ~[$9x10^{27}$, $4.5x10^{28}$] m^{-3}.

By comparing the estimated increase in deuterium density of $1.3x10^{27}$ m^{-3} needed to match the observed rising trend in measured neutron production rate to the estimated increase in deuterium wall density due to implanting deuterium over this period of runs, it is found that the matching condition is exceeded by a factor of 7 to 35. If it is assumed that a substantial fraction of the implanted deuterium does diffuse out of the aluminum chamber with time due to heating, the upward trend in neutron production rate operating under fixed cathode voltage, cathode current, and chamber pressure due to an increasing contribution of embedded fusion events can be considered plausible.

7.4 Summary

Repeated measurements of the neutron production rate for fixed experimental parameters cathode voltage, cathode current, and chamber pressure revealed an upward trend in neutron rates over a span of 100 run operations. The effects of impurity gas, chamber condition, and embedded fusion were investigated as possible causes of this trend in neutron production rate. A test of the impact of impurities in the system showed that a near 1:1 ratio of deuterium to impurity gas (total chamber pressure ~0.5 mTorr) decreased the measurable neutron production rate by about a factor of 3 for impurity gas loads originating from a calibrated atmospheric leak or heated chamber outgassing in an unconditioned system. By extensive run conditioning of the chamber, the impact of outgassing impurities on the system due to heating of the chamber walls was reduced to a negligible effect. Residual gas analysis of the background chamber gas during run operations showed a reduction in relative intensities of all non-deuterium gas constituents over this series of experiments while keeping the chamber under constant vacuum, and the effect of reducing gas impurities in the system can lead to an increase in neutron production rate. The extent to which the reduction of impurity gas over time contributed to the upward trend in neutron rates remains uncertain, since careful calibrations of the quadrupole mass analyzer response are needed to determine absolute partial pressure measurements of the impurity gas; however, the impurity fraction with respect to deuterium is estimated to be <0.1% contribution of the total background gas pressure for this work.

The presence of embedded fusion reactions was also considered as a contributor to the upward trend in neutron rates due to the build-up of implanted deuterium density in the chamber wall. An estimated increase in deuterium density of ~$1x10^{27}$ m^{-3} near the surface of the aluminum wall was calculated to be necessary to account for this trend, and almost all embedded fusion

reactions are predicted to occur within a 0.2 μm depth for typical incident deuterium particle energies of 26 keV. An estimated ~10^{22} fast deuterium particles originating from charge exchange reactions were incident on the chamber wall from runs 3788 to 3842, and build-up in deuterium density over these runs is estimated to be ~$3x10^{28}$ m^{-3} if distributed uniformly over a 0.4 μm depth. Since the estimated increase in deuterium during this run period is found to be on the order of ten times larger than the build-up needed to match the upward trend, embedded fusion reactions may be a plausible mechanism for the observed increase in neutron rate under these assumptions. More detailed experiments may be designed in the future to measure the increase in deuterium density and depth profile at the wall during IEC operations.

7.5 References

[1] M. K. Michalak, "Increasing the High Voltage Capabilities and Exploring Parameter Space of an Inertial Electrostatic Confinement Fusion Neutron Source for the Detection of Chemical Explosives," PhD dissertation, University of Wisconsin-Madison, 2017.

[2] E. C. Alderson, "Experimental and Theoretical Characterization of Negative Deuterium Ion Distributions in a Gridded Inertial-Electrostatic Confinement Device," University of Wisconsin-Madison, 2012.

[3] National Institute of Standards and Technology, "NIST Chemistry WebBook," 2018. [Online]. Available: https://webbook.nist.gov/. [Accessed: Apr. 30, 2018].

[4] G. E. Becerra, "Neutral Particle Analysis in Inertial Electrostatic Confinement Fusion Devices," PhD dissertation, University of Wisconsin-Madison, 2014.

[5] S. M. Myers, F. Besenbacher, and J. K. Norskov, "Immobilization mechanisms for ion-implanted deuterium in aluminum," *J. Appl. Phys.*, vol. 58, no. 5, pp. 1841–1850, Sep. 1985.

8. Conclusions

The work presented in this work has achieved a new milestone in gridded IEC devices by increasing operational capability to 210 kV at the cathode grid using a 2-stage feedthrough technique. The new feedthrough, designed and implemented for this work by the author, has allowed access to new experimental parameter space previously unachieved in any gridded IEC device, and an experimental campaign has been conducted to study the neutron production rate response. Comparisons of the experimental data were made to the VICTER code, a theoretical model of the neutron-producing reactions in a spherical IEC device, for variations of cathode voltage, cathode current, and chamber pressure. Additionally, long term trends showed a measurable increase in the neutron production rate for repeated measurements under similar experimental parameters taken over 100 experimental runs conducted over the course of 43 days. To analyze this trend in neutron production rate, an investigation into the effect on neutron rate due to the presence of impurity background gas has been performed, and an estimation of the effect of embedded fusion contributions from the chamber wall has been made. The following is a summary of conclusions from this work:

- The 2-stage resistor divider feedthrough approach has been found to be robust against destructive arcs and failures, which occurred in past designs, due to the implementation of an intermediately biased electrostatic shield to protect the insulating standoff from charged particle bombardment. High voltage standoff under plasma operations has been achieved to 210 kV, 30 mA at the cathode grid.

- A high voltage plasma conditioning procedure using deuterium fuel has been found to be an effective method of improving the standoff performance of the high voltage electrodes during operation. Additionally, careful alignment of the cathode and anode grid openings and doubling the number of longitude wires at the cathode improved the high voltage stability of the system for operations beyond 180 kV; however, the issue of electron jets melting portions of the anode grid wire, which had been seen with fewer longitude wires, persisted.
- A new steady-state D-D neutron production rate record in an IEC device of 3.8×10^8 n/s has been achieved at a cathode voltage of 200 kV, cathode current of 100 mA, and a chamber pressure at 1.0 mTorr D_2.
- The linear neutron production rate response to variation in the cathode current from 30 to 100 mA indicates the fusion reaction regimes are dominated by beam-background and beam-embedded collisions in this IEC device for cathode voltages ranging 170 to 200 kV at a 1.0 mTorr D_2 chamber pressure.
- A factor of 2.5 increase in neutron production rate response for a factor of 6 increase in the deuterium pressure from 0.2 mTorr D_2 suggests the effects of non-fusing deuterium collisions are sufficient to soften the energy spectrum of the accelerated deuterium ions and reduce the fusion reaction rates.
- A comparison of neutron production rate scaling with cathode voltage to the VICTER model prediction showed the model under predicts the neutron production rate by nearly a factor of 8. This discrepancy may be due to unaccounted for physical processes in the model.

- Residual gas analysis of the background chamber gas during run operations showed a reduction in relative intensities of all non-deuterium gas constituents while keeping the chamber under constant vacuum, and the effect of reducing gas impurities in the system can lead to an increase in neutron production rate.
- A calculated increase in deuterium density of ~$1x10^{27}$ m^{-3}, about 2% the atomic density of aluminum, near the surface of the chamber wall is needed to account for the upward trend in measured neutron production rates for repeated experimental conditions, and almost all embedded fusion reactions are predicted to occur within a 0.2 μm depth for typical incident deuterium particles energies of 26 keV.
- An estimated ~10^{22} fast deuterium particles originating from charge exchange reactions were incident on the chamber wall from runs 3788 to 3842, and build-up in deuterium density over these runs is estimated to be ~$3x10^{28}$ m^{-3} if distributed uniformly over a 0.4 μm depth and if there is no diffusion of deuterium out of the aluminum. Since the estimated increase in deuterium during this run period is found to be on the order of ten times larger than the build-up needed to match the upward trend, embedded fusion reactions may be a plausible mechanism for the observed increase in neutron rate under these assumptions.

9. Recommendations for Future Work

This work has contributed to significant advancements in the high voltage operational capability of gridded IEC devices and to new insight into the neutron production rate up to 200 kV. In the process of completing this work, several avenues for future advancement have been identified.

The investigation into embedded fusion contributions to the neutron production rate has offered insight into the order of magnitude density of deuterium near the surface of the aluminum chamber wall needed to account for measured increase in rates over time. Several assumptions were made concerning the density profile of embedded deuterium and incident deuterium flux to estimate these rates, and the actual deuterium density profile and fusion rate at the wall remains unverified. Experimental study of the wall implantation by fast deuterium particles can be performed by inserting samples into the chamber and measuring the deuterium density profile build up by nuclear reaction analysis or other material characterization techniques. A collimated proton detector looking at the wall can give a measure of the fusion rate by measuring the fast proton producing channel of the D-D reaction, and the neutral particle analyzer can give more detailed information about the incident neutral particle energy distribution at the wall. The results of these experimental studies may be used to better inform the embedded fusion model and add to the fusion rate prediction capabilities for IEC devices.

The VICTER model showed discrepancies in the prediction of absolute neutron production rate when compared to the measurements taken in the cathode voltage variation study; however, the code predicted a scaling of rates in good agreement with the measurements. A portion of this discrepancy may be due to the presence of embedded fusion reactions contributing to the

experimental measurements that are unaccounted for in the model, and further investigation of the embedded rates may reduce this discrepancy. Another discrepancy with the VICTER model showed a greater than linear rise in neutron production rate with increase in chamber pressure starting from 0.2 mTorr D_2 in comparison to a less than linear scaling with pressure observed in the experimental setup. The cause of this scaling discrepancy remains unknown, and an investigation into how the model depends on background chamber pressure should be conducted to resolve this physics issue.

The campaign to increase high voltage operation has led to the development of a resistively divided 2- stage high voltage feedthrough, and this prototype design may be extended to a multiple stage approach, allowing for a higher maximum operating voltage. The results of this work showed a less than linear increase of fusion rate with cathode grid operations greater than 180 kV for deuterium fuels; however, studies of advanced fuel reactions such as D-^{3}He and ^{3}He-^{3}He demand higher ion energy and thus higher voltage to achieve significant fusion rates for experimental study. Technical improvements to the design can be made by replacing the nylon insulator with a bonded ceramic to metal insulator. By moving to all ceramic and metal materials, higher temperature operation and better vacuum performance may be achieved, leading to more reliable high voltage standoff. Additionally, the field shaping geometry used to shield the insulating surfaces from charged particle bombardment may be optimized to reduce the current collected at the shield electrode. This will relax the requirements of the drain current due to the cathode-resistor path to ground, and tax the high voltage power supply less by selecting higher resistive values. The full high voltage capability of the new 2-stage high voltage feedthrough remains unknown since the cathode grid seems to be an influencing factor of the breakdown limits. To separate the grid influence from the feedthrough high voltage design limits, the cathode grid may be replaced

by a hollow sphere electrode, representing a minimization of the electric field at the cathode surface, and a high potential test of the system to determine the upper boundary of the feedthrough standoff may be conducted.

High voltage performance of the system may also be limited by high electric fields at the cathode grid wire surfaces due to the manufacturing process, which produces sharp points and irregularities in the grid structure and provides sites where field-enhanced breakdown may occur. Uniformity in the grid design can be achieved through the use of additive manufacturing of tungsten; however, surface roughness and material porosity are key issues with the use of additive manufacturing in high voltage applications. Post-processing of the material surface will likely be needed to ensure smooth electrode surfaces for high voltage standoff performance, and outgassing of a porous material is detrimental to high voltage standoff and vacuum.

The cathode grid geometry may be optimized for hole symmetry, hole alignment with anode holes, transparency, and power dissipation through the use of additive manufacturing. Melting of the anode grid wires by localized electron jets was a pervasive issue while operating at high voltage and high currents. The presence of fast electrons leaving the cathode region is an inherent issue with this type of gridded IEC device, and the anode design may be revised to withstand a higher heat flux by increasing material thickness or by using refractory metals in place of stainless steel.

Appendix: High Voltage Feedthrough Circuit Model

This appendix details the derivation of the circuit model equations that describe the high voltage circuit used to operate the IEC device and 2-stage feedthrough and is an extension of the circuit model discussion presented in section 4.2.1. Section A.1 derives the circuit equations used to analyze the old 2-stage biased feedthrough that used an independent power supply to bias the shield electrode, and section A.2 derives the circuit equations used to analyze the new 2-stage resistor divider design developed for this work.

A.1 Analysis of 2-stage biased feedthrough circuit model

To estimate the current contribution to the system at the shield electrode, a circuit model of the previous 2-stage biased feedthrough, shown in Figure A-1, is evaluated using Kirchhoff's laws for nodal and mesh analysis. In this model, the plasma resistivity is represented by a total resistance across the plasma gaps at the cathode, R_{p-c}, and at the shield R_{p-s}; the plasma resistance is treated as unknown in this analysis and only the resistive portion of the total plasma impedance is considered for DC analysis. The high voltage power supply voltage, V_{HVPS}, sets the cathode voltage, $V_{cathode}$, and the feedthrough power supply, V_{FTPS}, sets the voltage at the shield electrode, V_{shield}. The quantities V_{HVPS} and I_{HVPS} along with V_{FTPS} and I_{FTPS} are determined from the power supply meter outputs. I_{shield} is drawn to represent the current contribution to the shield from the plasma resistance path.

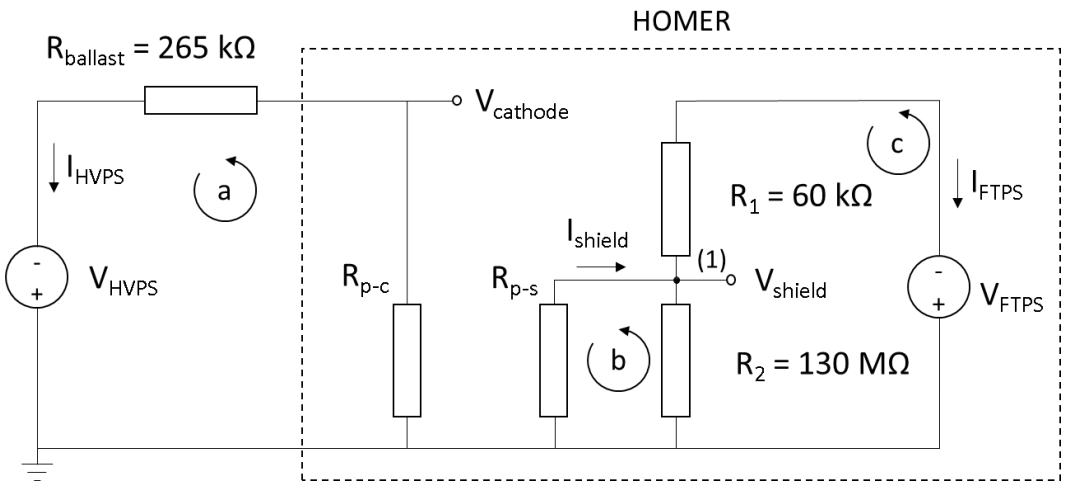

Figure A-1: Circuit model of the previous 2-staged biased feedthrough design for analysis.

Summing the voltage drops around loop a due to a loop current, i_a , starting clockwise from ground gives:

(a) $$-i_a R_{p-c} - i_a R_{ballast} + V_{HVPS} = 0 \quad \text{A-1}$$

Taking $i_a = I_{HVPS}$ and rearranging to solve for the plasma resistance at the cathode gives:

$$R_{p-c} = \frac{V_{HVPS} - I_{HVPS} R_{ballast}}{I_{HVPS}} \quad \text{A-2}$$

The cathode voltage may be determined moving counter clockwise starting from the power supply:

$$V_{cathode} = -V_{HVPS} + I_{HVPS} R_{ballast} \quad \text{A-3}$$

To operate the cathode at -100 kV with a cathode current of 30 mA, then solving equation A-3 for the high voltage power supply meter voltage would give 108 kV.

Next, to solve for the current collected at the shield electrode, the voltage drop is summed around loop c, moving counter clockwise from ground:

(c) $$-V_{FTPS} - i_c R_1 + (i_b - i_c) R_2 = 0$$ A-4

Taking $i_b = -I_{shield}$ and $i_c = -I_{FTPS}$, equation A-4 is solved in terms of I_{shield}:

$$I_{shield} = I_{FTPS}\left(\frac{R_1 + R_2}{R_2}\right) - \frac{V_{FTPS}}{R_2}$$ A-5

The voltage at the shield is determined by working clockwise around loop c from the feedthrough power supply:

$$V_{shield} = -V_{FTPS} + I_{FTPS} R_1$$ A-6

The plasma resistance at the shield can be determined by combining equations A-5 and A-6 by:

$$R_{p-s} = \frac{V_{shield}}{I_{shield}}$$ A-7

A.2 Analysis of 2-stage resistor divider feedthrough circuit model

Since the new 2-stage resistive voltage divider design does not rely on a regulated voltage supply to maintain a shield set point voltage, the cathode voltage and current will be affected by the addition of current collected at the shield. A simple DC circuit was modeled for the resistive voltage divider design, shown in Figure A-2. Here, a voltage platform and electrostatic shield are placed between two resistors which bias the shield at an intermediate potential with respect to the center conducting stalk and the grounded chamber. The plasma impedance at the cathode and the shield are represented by the resistive component of the plasma for the purposes of this DC circuit analysis as done previously in section A.1.

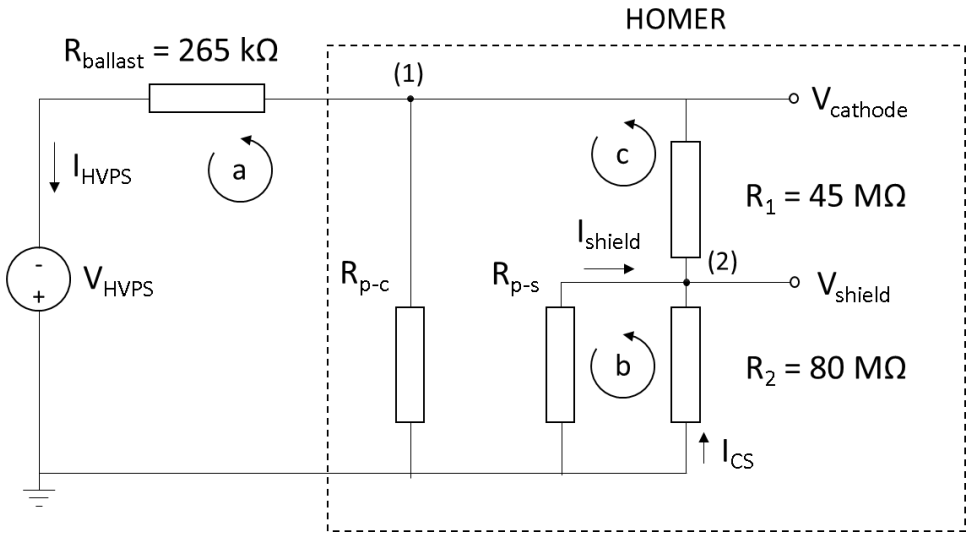

Figure A-2: Circuit model of the 2-stage resistive feedthrough design for analysis.

To determine the current at the cathode grid and shield electrodes, this system may be solved in terms of the measured voltage and current at the high voltage power supply along with a measurement of the current draw, I_{CS}, through the second stage resistor, R_2, via a 1 kΩ current

sense resistor placed between R_2 and ground and is a negligible perturbation of the voltage across the second stage resistor. The voltage drops around loops a, b, and c are determined moving counterclockwise from ground:

(a) $$(-i_a + i_c)R_{p-c} - i_a R_{ballast} + V_{HVPS} = 0 \quad \text{A-8}$$

(b) $$-i_b R_2 + (-i_b + i_c)R_{p-s} = 0 \quad \text{A-9}$$

(c) $$(-i_c + i_b)R_{p-s} - i_c R_1 + (-i_c + i_a)R_{p-c} = 0 \quad \text{A-10}$$

Adding together equations A-8, A-9, and A-10 reduces to:

$$V_{HVPS} - i_a R_{ballast} - i_b R_2 - i_c R_1 = 0 \quad \text{A-11}$$

The loop currents are related to the system measurements by:

$$i_a = I_{HVPS} \quad \text{A-12}$$

$$i_b = I_{CS} \quad \text{A-13}$$

And by nodal analysis at (2):

$$i_c = I_{shield} + I_{CS} \quad \text{A-14}$$

Substituting the loop current relationships into equation A-11 and solving for the shield current gives:

$$I_{shield} = \frac{[V_{HVPS} - R_{Ballast} I_{HVPS} - (R_1 + R_2) I_{CS}]}{R_1} \quad \text{A-15}$$

And the voltage of the shield is determined by the voltage drop across the second stage resistor to ground:

$$V_{shield} = -I_{CS} R_2 \quad \text{A-16}$$

The current collected at the cathode is found by nodal analysis at (1):

$$I_{cathode} = I_{HVPS} - I_{shield} - I_{CS} \quad \text{A-17}$$

And the cathode voltage is determined once again by the voltage drop across the resistor ballast:

$$V_{cathode} = -V_{HVPS} + I_{HVPS} R_{ballast} \quad \text{A-18}$$

The plasma resistance at the cathode and at the shield are determined by:

$$R_{p-c} = \frac{V_{cathode}}{I_{cathode}} \quad \text{A-19}$$

$$R_{p-s} = \frac{V_{shield}}{I_{shield}} \quad \text{A-20}$$

Under no plasma load, the system reduces simply to the current drawn, I_{drain}, from the high voltage power supply across the series resistance from the ballast and the two resistor stages:

$$I_{drain} = I_{HVPS_{no\ plasma}} = \frac{V_{HVPS}}{R_{Ballast} + R_1 + R_2} \quad \text{A-21}$$

The drain current is related to the current draw across the second stage current sense resistor by combining equations A-15 and A-21 which reduces to:

$$I_{CS} = I_{Drain} - I_{Cathode}\left(\frac{R_{Ballast}}{R_{Ballast} + R_1 + R_2}\right) - I_{Shield}\left(\frac{R_{Ballast} + R_1}{R_{Ballast} + R_1 + R_2}\right) \quad \text{A-22}$$

The power dissipation, P, across each resistor stage is:

$$P_1 = (I_{Shield} + I_{CS})^2 R_1 \quad \text{A-23}$$

$$P_2 = I_{CS}^2 R_2 \quad \text{A-24}$$